Reduction of deterministic coupled atmosphere-ocean models to stochastic ocean models: a numerical case study of the Lorenz-Maas system

Ludwig Arnold
Institut für Dynamische Systeme
Fachbereich 3, Universität, Postfach 33 04 40
28334 Bremen, Germany
arnold@math.uni-bremen.de

Peter Imkeller and Yonghui Wu*
Institut für Mathematik
Humboldt-Universität zu Berlin
10099 Berlin, Germany
imkeller@mathematik.hu-berlin.de
yonghui@mathematik.hu-berlin.de

December 2, 2002

Abstract

Our starting point is the Lorenz-Maas coupled atmosphere-ocean model which was proposed by van der Schrier and van Veen and couples the ocean model by Maas with the Lorenz-84 model of the atmosphere. This 6-dimensional model (3-dimensional slow ocean and 3-dimensional fast atmosphere) is, to the knowledge of the authors, the simplest atmosphere-ocean model presently available which is derived from first principles in a controlled manner.

This paper is an extensive numerical case study of the model, thereby implementing *Hasselmann's program*, i.e. applying the various mathematical techniques of reducing the fully coupled deterministic model to a deterministic or stochastic model for the ocean alone, namely to

- the (deterministic) statistical model, using the method of averaging,
- the linear stochastic model, based on the central limit theorem for the error in averaging,
- the nonlinear stochastic model, also known as Hasselmann's equation.

The long-term and bifurcation behavior of these models are studied and compared. The general result is that in most situations the nonlinear stochastic model outperforms the other one's.

Key words and phrases: Lorenz-84 model, Maas model, statistical climate model, stochastic climate model, invariant measure, method of averaging, linear diffusion approximation, nonlinear diffusion approximation, Hasselmann's equation, bifurcation analysis

MSC2000: primary 86A10; secondary 34F05, 37G35, 60H10.

Contents

1	Introduction. Reduction of multiscale climate models	2
2	Mathematical reduction methods: averaging, linear and nonlinear diffusion approximation	3
	2.1 The classical case	. 4
	2.2 The general case of fully coupled equations	. 7

^{*}On leave from the Institute of Atmospheric Physics, Chinese Academy of Sciences, Beijing 100029, China. Financial support from DFG which allowed the author to spend a year in Berlin is gratefully acknowledged.

o	THE	e Lorenz-Maas coupled atmosphere-ocean model	9
4	Dyr	namics and bifurcation of the Lorenz-Maas model	13
	4.1	Existence of a global attractor	13
	4.2	Dynamics and bifurcation of the Maas ocean model	15
	4.3	Dynamics and bifurcation of the Lorenz-84 atmosphere model	24
5	Stat	tistical characteristics of the reduced models	28
	5.1	Invariant measures of the Lorenz-84 atmosphere model	29
	5.2	The drift coefficient of the reduced models	31
	5.3	The diffusion coefficient of the reduced models	32
6	Bifu	urcation analysis of the statistical ocean model	35
7	Con	nparison of the unreduced model with the three reduced models	38
	7.1	The basics of our simulations	38
	7.2	The unreduced ocean model forced by the atmosphere	42
		7.2.1 Simulation of the unreduced ocean model	42
		7.2.2 Comparison of the reduced ocean models with the unreduced model forced by the atmosphere	44
	7.3	The unreduced ocean model coupled to the atmosphere	46
		7.3.1 Simulation of the unreduced ocean model	
		7.3.2 Comparison of the reduced ocean models with the unreduced model coupled to the atmosphere	
8	Con	nclusions and discussion	47

1 Introduction. Reduction of multiscale climate models

A characteristic feature of climatic records is their pronounced *variability*, meaning that climatic time series have a positive continuous power spectrum (spectral density) over the whole range of frequencies. This ubiquitous variability is also shown by computer data produced by the most advanced deterministic General Circulation Models. In short, most output data look like random noise. An understanding of the origin of climatic variability from extreme ice age changes to seasonal anomalies is still a primary goal of climate research.

Hasselmann in his visionary 1976 paper [12] attributes climate variability to the existence of various time scales, more precisely to the internal forcing by the short time scale "weather" (all variables with period up to 15 days, say, mainly related to atmospheric processes). Slowly responding components of the system (such as the ocean, the cryosphere and the biosphere) act as integrators of this input in much the same way as a pollen grain in a liquid integrates the short time impact of the molecules to yield Brownian motion. In short, the "weather" drives the "climate" through internal random forcing. Arnold [1] has recast *Hasselmann's program* of reducing complex deterministic multiscale climate models to simpler stochastic models for the slow variables in modern mathematical language to which we come back in Section 2.

After a first burst of stochastic modelling papers in the years following Hasselmann's article [12] in which the viability of the concept was demonstrated using very simple "toy models" there was a lull of work in this field which we attribute to disillusionment of the meteorology community as the program did not seem to live up to its original expectations.

We have witnessed a resurgence of interest in stochastic climate models in recent years. This is due, on the one hand, to the possibility of carrying out numerical studies of more realistic climate models, and, on the other hand, to the availability of new mathematical reduction methods. See the Proceedings volume on *Stochastic Climate Models* [17] edited by P. Imkeller and J.-S. von Storch, and the Special Issue of the journal *Stochastics and Dynamics*, also entitled *Stochastic Climate Models*, edited by P. Imkeller and A. Monahan [16].

We also refer to the work of Majda, Timofeyev and Vanden-Eijnden [35, 36] about general strategies of replacing the unresolved degrees of freedom in atmosphere-ocean models by noise and for the treatment of several rather complex illustrative examples.

The present paper is, to our knowledge, the first systematic implementation of Hasselmann's program for a two-scale atmosphere-ocean model of moderate complexity which is derived from first principles in a controlled manner (hence is not a toy model). It is necessarily a numerical study as it seems to be hopeless today to aim at rigorous results. Moreover, we will freely use mathematical methods, concepts and statements whose applicability cannot be rigorously justified for our model.

We nevertheless believe that this numerical case study is interesting and was worthwhile to be carried out as it is the first one to systematically compare the performance of the various stochastic reduction methods (including the nonlinear diffusion approximation which was only recently understood) for a non-trivial fully coupled two-scale model.

The paper is organized as follows: In Section 2 we describe the three mathematical reduction methods we will consider. Section 3 is devoted to the presentation of the 6-dimensional Lorenz-Maas model. In Section 4 we study the dynamical and bifurcation behavior of the full Lorenz-Maas model as well as of the 3-dimensional Lorenz atmosphere subsystem with frozen ocean, resp. of the 3-dimensional Maas ocean subsystem with frozen atmosphere. Section 5 is devoted to the calculation of the ingredients of the stochastic models. Section 6 is a systematic bifurcation analysis of the reduced statistical ocean model (obtained via averaging). The heart of the paper is Section 7 in which we numerically compare the performance of the original unreduced model with the three reduced models, section 8 contains our conclusions and a discusion of the main findings of our study.

$\mathbf{2}$ Mathematical reduction methods: averaging, linear and nonlinear diffusion approximation

Let

$$\dot{z} = h(z)$$

be an ODE in some Euclidean space. In many applications we can naturally separate the variables as

$$z = (x, y)$$

with strongly differing "response times" $\tau_y \approx \varepsilon \ll \tau_x \approx 1$, so that y is the vector of fast variables, while x is the vector of slow variables. Introducing the small scaling parameter ε into the equation $\dot{z} = h(z)$ yields the equivalent coupled system of the two ODE

$$\dot{x}_t^{\varepsilon} = f(x_t^{\varepsilon}, y_t^{\varepsilon}), \quad x_0^{\varepsilon} = x \in \mathbb{R}^d, \tag{2.1}$$

$$\dot{x}_{t}^{\varepsilon} = f(x_{t}^{\varepsilon}, y_{t}^{\varepsilon}), \quad x_{0}^{\varepsilon} = x \in \mathbb{R}^{d},
\dot{y}_{t}^{\varepsilon} = \frac{1}{\varepsilon} g(x_{t}^{\varepsilon}, y_{t}^{\varepsilon}), \quad y_{0}^{\varepsilon} = y \in \mathbb{R}^{m}.$$
(2.1)

The general problem of model reduction consists of approximating the slow part $x_t^{\varepsilon}(x,y)$ of the solution of (2.1,2.2)as accurately as possible (and on a time interval as long as possible) not by solving (2.1,2.2) explicitly, but by using only some long-term "statistical" properties of $y_t^{\varepsilon}(x,y)$ in order to obtain an equation for the slow variables alone.

This is of course part of a now classical program: It started with the method of averaging centuries ago, although the rigorous mathematical foundation was provided only some 40 years ago by Bogolyubov and Mitropolskii [3].

However, this program has been only partly implemented, in particular for the fully coupled case (2.1,2.2).

To provide the reader with "clean" and proven statements we first deal in detail with the case where y is not coupled to x, in fact is a fast stationary stochastic process (Subsection 2.1). The rather complete results for this case (which we call classical) can serve as a guideline and to direct our "wishful thinking" for the fully coupled case which is much more involved and which we treat in Subsection 2.2.

2.1 The classical case

Consider

$$\dot{x}_t^{\varepsilon} = f(x_t^{\varepsilon}, \xi_{t/\varepsilon}), \quad x_0^{\varepsilon} = x \in \mathbb{R}^d, \quad t \in [0, T]. \tag{2.3}$$

Here ξ_t is an ergodic stationary stochastic process on some probability space $(\Omega, \mathcal{F}, \mathbb{P})$ with values in \mathbb{R}^m , cadlag (i.e. right-continuous with left-hand limits) trajectories and invariant probability distribution $\mathbb{P}\{\xi_t \in \cdot\} = \rho(\cdot)$. The vector field $f: \mathbb{R}^d \times \mathbb{R}^m \to \mathbb{R}^d$ is continuous in (x, ξ) , $f(\cdot, \xi)$ is globally Lipschitz-continuous uniformly with respect to ξ , and $f(0, \cdot)$ is bounded.

We can average out the fast process $\xi_{t/\varepsilon}$ from (2.3) keeping the slow variable x "frozen" and arrive at the averaged vector field

$$\bar{f}(x) := \mathbb{E} f(x, \xi_0) = \int_{\mathbb{R}^m} f(x, \xi) \rho(d\xi) = \lim_{T \to \infty} \frac{1}{T} \int_0^T f(x, \xi_t) dt \quad \mathbb{P}\text{-a.s.} ,$$
 (2.4)

which is again globally Lipschitz continuous and of at most linear growth in x.

Hence the ODE (2.3) as well as the **averaged model (A)** (in climatology also named *statistical climate model*) described by the ODE

$$\dot{\bar{x}}_t = \bar{f}(\bar{x}_t), \quad \bar{x}_0 = x \in \mathbb{R}^d, \tag{2.5}$$

both have global solutions $x_t^{\varepsilon}(x)$ resp. $\bar{x}_t(x)$ for any initial value $x \in \mathbb{R}^d$ and $t \in [0,T]$ which we want to compare.

A novel feature of our presentation is that we will determine the order of magnitude of the L^2 -error between the various reductions and the original in terms of powers of the smallness parameter ε . This will enable us to decide whether a certain approximation is "better" than another one.

Theorem 2.1 (Averaging Principle (A))

Let the above assumptions on f and ξ_t be satisfied, and let $x_t^{\varepsilon}(x)$ be the solution of (2.3) and $\bar{x}_t(x)$ the solution of (2.5). Assume that the $d \times d$ covariance (or correlation) matrix

$$R_x(t) := \operatorname{cov}(f(x, \xi_t), f(x, \xi_0)) = \mathbb{E}(f(x, \xi_t) - \bar{f}(x))(f(x, \xi_0) - \bar{f}(x))'$$
(2.6)

satisfies

$$\lim_{t \to \infty} R_x(t) = 0 \quad \text{for all } x \in \mathbb{R}^d.$$
 (2.7)

Then for each T>0 there exists a constant C_T independent of x and ε such that for all $x\in\mathbb{R}^d$ and $\varepsilon>0$

$$\mathbb{E}\max_{0 \le t \le T} \|x_t^{\varepsilon}(x) - \bar{x}_t(x)\|^2 \le C_T \varepsilon. \tag{2.8}$$

The fact that $\mathbb{E}\max_{0\leq t\leq T}\|x_t^{\varepsilon}(x)-\bar{x}_t(x)\|\to 0$ as $\varepsilon\to 0$ was proved by Khasminskii [23]. The above L^2 version, the estimate (2.8) and the fact that the decay of correlation to zero expressed by (2.7) is sufficient for the statement (2.8) can be easily deduced from Khasminskii's original paper [23]. Our program in the remainder of this subsection is to replace $\bar{x}_t(x)$ in (2.8) by a "better" approximation of $x_t^{\varepsilon}(x)$ in the sense that

- the mean square error is smaller than in (2.8),
- the approximation is capable of catching long-term features of $x_t^{\epsilon}(x)$ which go beyond a fixed time interval.

To pursue this, we now look at the error $x_t^{\varepsilon} - \bar{x}_t$ made in the Averaging Principle. If the stationary stochastic process ξ_t is a periodic function, this error can be asymptotically expanded in powers of ε (see Sanders and Verhulst [40] for a precise statement).

If, however, ξ_t is a sufficiently mixing stochastic process, the error is of a completely different character: It has order $\sqrt{\varepsilon}$, and no further term of the asymptotic expansion can be written down.

Let ξ_t be a stationary stochastic process in \mathbb{R}^m with cadlag trajectories. We define the sub- σ -algebras of \mathfrak{F} generated by ξ_t as

$$\mathfrak{F}_s^t := \sigma(\xi_u : s \le u \le t), \quad -\infty \le s \le t \le \infty,$$

and the mixing coefficient of ξ_t by

$$\alpha(\tau) := \sup_{A \in \mathcal{F}_{-\infty}^0, B \in \mathcal{F}_{-\infty}^{\infty}} |\mathbb{P}(A)\mathbb{P}(B) - \mathbb{P}(A \cap B)|, \quad \tau \in \mathbb{R}^+.$$

The stochastic process ξ_t is called *strongly mixing*, if the (non-increasing) mixing coefficient satisfies

$$\lim_{\tau \to \infty} \alpha(\tau) = 0. \tag{2.9}$$

It follows that a strongly mixing stationary stochastic process is ergodic and, plugged into a function f satisfying our assumptions above, satisfies property (2.7). Good sources for all this are Rozanov [39, Chap. IV] and Ibragimov and Linnik [14, Chapter 17]).

We are now in a position to formulate Khasminskii's *Central Limit Theorem* [23] describing the evolution of the error in averaging asymptotically as the solution of a linear SDE.

Theorem 2.2 (Error in the Method of Averaging)

Let $f: \mathbb{R}^d \times \mathbb{R}^m$, $(x,\xi) \mapsto f(x,\xi)$, be continuous, and let $f(\cdot,\xi)$ together with its first and second derivatives with respect to x be bounded uniformly with respect to ξ . Let ξ_t be a stationary stochastic process with values in \mathbb{R}^m and cadlag trajectories which is strongly mixing and satisfies, moreover, the condition

$$\int_0^\infty \tau \,\alpha(\tau) \,d\tau < \infty. \tag{2.10}$$

Denote by $x_t^{\varepsilon}(x)$ and $\bar{x}_t(x)$ the solution of (2.3) and (2.5), resp. Then the Averaging Principle (Theorem 2.1) holds, and, moreover, for all $x \in \mathbb{R}^d$

$$\zeta_t^{\varepsilon,x} := \frac{1}{\sqrt{\varepsilon}} (x_t^{\varepsilon}(x) - \bar{x}_t(x)) \Rightarrow \zeta_t^x \quad \text{as } \varepsilon \to 0 \quad \text{on } [0,T].$$
 (2.11)

Here \Rightarrow means weak convergence (i.e. the probability distribution of the left-hand side converges to the probability distribution of the right-hand side as $\varepsilon \to 0$), and ζ_t^x is a Gauss-Markov (or Ornstein-Uhlenbeck) process on [0,T] given by the solution of the linear SDE

$$d\zeta_t^x = D\bar{f}(\bar{x}_t(x))\zeta_t^x dt + \sigma(\bar{x}_t(x)) dW_t, \quad \zeta_0^x = 0, \tag{2.12}$$

driven by the solution $\bar{x}_t(x)$ of the averaged ODE (2.5). In (2.12) the $d \times d$ matrix

$$D\bar{f}(x) := \left(\frac{\partial^i \bar{f}}{\partial x_j}\right)(x)$$

is the Jacobian of the averaged vector field \bar{f} , W_t is a standard Brownian motion in \mathbb{R}^d , and $\sigma(x)$ is the square root of the nonnegative-definite $d \times d$ matrix $\sigma(x)^2$ defined as the "nonlinear average"

$$\sigma(x)^{2} := \lim_{T \to \infty} \frac{1}{T} \int_{0}^{T} \int_{0}^{T} R_{x}(t-s)dtds = \int_{-\infty}^{\infty} R_{x}(t)dt = 2\pi S_{x}(0), \tag{2.13}$$

where $R_x(t)$ is the correlation matrix (2.6) of $\varphi_t := f(x, \xi_t)$ for frozen x, and $S_x(0)$ is its spectral density matrix at frequency $\lambda = 0$.

For a proof see the original paper by Khasminskii [23] or Freidlin and Wentzell [9, Chapter 7]. By our assumptions, the limits in (2.13) exist and define a C^2 function, and $\sigma(\cdot)^2$ and its first and second derivatives are bounded. The result of Theorem 2.2 is that we can replace the averaged equation (2.5) by the more informative pair of equations

$$\dot{\bar{x}}_t = \bar{f}(\bar{x}_t), \quad \bar{x}_0 = x, \tag{2.14}$$

$$d\zeta_t^x = D\bar{f}(\bar{x}_t(x))\zeta_t^x dt + \sigma(\bar{x}_t(x)) dW_t, \quad \zeta_0^x = 0, \tag{2.15}$$

which has skew product structure. We can approximate the original process $x_t^{\varepsilon}(x) = \bar{x}_t(x) + \sqrt{\varepsilon} \zeta_t^{\varepsilon,x}$ with $\zeta_t^{\varepsilon,x} \Rightarrow \zeta_t^x$ by the Gaussian process

$$\eta_t^{\varepsilon,x} := \bar{x}_t(x) + \sqrt{\varepsilon} \, \zeta_t^x \tag{2.16}$$

centered at $\bar{x}_t(x)$. We call (2.16) the linear diffusion approximation (L) of the original slow variable $x_t^{\varepsilon}(x)$.

As a by-product of his work [28] on the nonlinear diffusion approximation Kifer proved the following strong approximation of $x_t^{\varepsilon}(x)$ by (L).

Theorem 2.3 (Strong Linear Diffusion Approximation (L))

Let the assumptions of Theorem 2.2 hold true. Then for each $\varepsilon > 0$ there is a possibly richer probability space which carries a d-dimensional Brownian motion W_t and on which we can redefine ξ_t without changing its distribution such that for these ξ_t and W_t the solutions of (2.3), (2.5) and (2.12) satisfy for each $x \in \mathbb{R}^d$ and $\varepsilon > 0$

$$\mathbb{E}\max_{0 < t < T} \| x(x) - (\bar{x}_t(x) + \sqrt{\varepsilon} \zeta_t^x) \|^2 \le C_{\delta, T} \varepsilon^{1+\delta}$$
(2.17)

for any $\delta < 2/(90d + 177)$, where $C_{\delta,T}$ is independent of x and ε .

"Changing the probability space" in applications should not create any problem as such a space is a measuretheoretic underpinning and typically neither fixed nor unique anyway.

A comparison of Theorems 2.1 and 2.3 reveals that the linear diffusion approximation (L) given by (2.16), i.e. the solution of the averaged equation (2.5) corrected by the solution of the linear SDE (2.12) is a better approximation in the L^2 sense on a finite time interval than is the averaged motion (A).

However, the crucial drawback of (L) is that it will typically not be able to model correctly the long-term behavior of the original slow motion $x_t^{\varepsilon}(x)$. This drawback is partly remedied by another approximation which was proposed by Hasselmann [12, Sect. 4] and which has defied rigorous analysis until the recent work of Kifer [28].

Unlike the linear diffusion approximation which is a Gaussian correction of the solution of the averaged equation (2.5), the **nonlinear diffusion approximation (N)** is a state-dependent correction of the averaged equation itself, namely

$$dy_t^{\varepsilon} = \bar{f}(y_t^{\varepsilon}) dt + \sqrt{\varepsilon} \, \sigma(y_t^{\varepsilon}) dW_t, \quad y_0^{\varepsilon} = x, \tag{2.18}$$

where \bar{f} and σ are defined above. Using Doob's and the Gronwall-Bellman inequality and the fact that \bar{f} and σ are Lipschitz and bounded it follows that for each $x \in \mathbb{R}^d$ and $\varepsilon > 0$

$$\mathbb{E} \max_{0 \le t \le T} \|y_t^{\varepsilon}(x) - \bar{x}_t(x)\|^2 \le C_T \varepsilon, \tag{2.19}$$

where C_T is independent of x and ε . Hence $\bar{x}_t(x)$ is as close to $y_t^{\varepsilon}(x)$ as it is to $x_t^{\varepsilon}(x)$, namely $O(\sqrt{\varepsilon})$ in L^2 . The question now arises whether $x_t^{\varepsilon}(x)$ and $y_t^{\varepsilon}(x)$ are closer to each other than $O(\sqrt{\varepsilon})$. This turns out to be indeed the case. Here is Kifer's result [28].

Theorem 2.4 (Nonlinear Diffusion Approximation (N))

Let the assumptions of Theorem 2.1 hold true. Then for each $\varepsilon > 0$ there is a possibly richer probability space which carries a d-dimensional Brownian motion W_t and on which we can redefine ξ_t without changing its distribution such that for these ξ_t and W_t the solution $x_t^{\varepsilon}(x)$ of (2.3) and the solution $y_t^{\varepsilon}(x)$ of (2.18) satisfy for each $x \in \mathbb{R}^d$ and $\varepsilon > 0$

$$\mathbb{E}\max_{0 \le t \le T} \|x_t^{\varepsilon}(x) - y_t^{\varepsilon}(x)\|^2 \le C_{\delta, T} \varepsilon^{1+\delta}$$
(2.20)

for any $\delta < 2/(90d + 177)$, where $C_{\delta,T}$ is independent of x and ε .

As a result, the linear diffusion approximation (L) given by $\bar{x}_t(x) + \sqrt{\varepsilon} \zeta_t^x$ and the nonlinear diffusion approximation (N) given by $y_t^{\varepsilon}(x)$ approximate the original slow motion $x_t^{\varepsilon}(x)$ on a finite time interval [0, T] equally well, namely with an L^2 error of order $O(\varepsilon^{1/2+\delta/2})$. However, the nonlinear SDE (2.18) is more likely to catch the correct long-term and qualitative behavior of the slow motion. This is also convincingly supported by

examples, see Arnold [2].

Large deviations in averaging: Freidlin in his monumental 1978 paper [8] developed the theory of large deviations in averaging by studying the phenomena observable only on an exponential time scale $e^{c/\varepsilon}$ (like exit of the slow variable from the neighborhood of a stable steady state of the averaged equation, invariant measures, wandering between local attractors etc.). An account of Khasminskii's and Freidlin's theories is given in Chapter 7 of Freidlin and Wentzell's book [9].

In order not to extend even further an already long paper we have decided to exclude large deviations theory from our study, even so we feel that it is highly relevant to climatology as it provides the means of describing the "hopping" of the climate between local attractor basins/metastable states (extreme climate events), see Arnold [1], Hasselmann [13] and Imkeller [15].

2.2 The general case of fully coupled equations

We now return to the fully coupled system

$$\dot{x}_t^{\varepsilon} = f(x_t^{\varepsilon}, y_t^{\varepsilon}), \quad x_0^{\varepsilon} = x \in \mathbb{R}^d \text{ (climate, slow variables)},$$
 (2.21)

$$\dot{y}_t^{\varepsilon} = \frac{1}{\varepsilon} g(x_t^{\varepsilon}, y_t^{\varepsilon}), \quad y_0^{\varepsilon} = y \in \mathbb{R}^m \text{ (weather, fast variables)}.$$
 (2.22)

In climatology, the distinct time scales are mainly due to the huge heat capacity differences e.g. between sea water and atmosphere.

Denote by $(x_t^{\varepsilon}, y_t^{\varepsilon}) = (x_t^{\varepsilon}(x, y), y_t^{\varepsilon}(x, y))$ the solution of (2.21, 2.22) with the initial value (x, y). Now the slow and fast variables are cross-coupled to each other.

The situation now becomes much more complicated than in the classical case, and there are only few rigorous results. We will of course in principle have the three reduced models (A), (L) and (N) also in the general case. The conditions of their validity are, however, often not known or very restrictive, and so are the statements. A thorough discussion of the difficulties is given by Kifer [26, 27]. The results of Kifer obtained in [24, Remark 2.5] and [26, Sect. 3] are, to our knowledge, the only presently available mathematically rigorous results for averaging in the fully coupled case (2.21, 2.22). There is a promising *Ansatz* by Gelfert [10] using Young measure limits to derive an averaged equation.

A good general reference is also Lochak and Meunier [31] in which also the classical work of Anosov and Neistadt on exceptional sets of initial values in averaging is presented.

The task of the Method of Averaging is, as above, to average out y from f such that $x_t^{\varepsilon}(x,y)$ converges on [0,T] to $\bar{x}_t(x)$, the solution of some averaged equation, at least for many initial values (x,y).

Selection of invariant measures

To prepare the averaging procedure for (2.21, 2.22) we consider the auxiliary weather ODE

$$\dot{y}_t = g(x, y_t), \quad y_0 = y,$$
 (2.23)

with frozen climate variables x, and denote by $(t,y) \mapsto \varphi_t^x(y)$ the dynamical system (flow) generated by (2.23) indexed by the fixed parameter x.

The first basic difficulty is that the dynamical system φ^x typically has many invariant measures $\mu_x(dy)$ (except in the rare case of unique ergodicity) which generally also depend on x: Various fixed points, periodic and quasiperiodic solutions might coexist with measures on chaotic attractors, and this situation might change if we vary x which can be considered as a bifurcation parameter for (2.23). There is no canonical rule telling us which of the many invariant measures $\mu_x(dy)$ to choose.

The average of $f(x,\cdot)$ over y now becomes

$$\lim_{T \to \infty} \frac{1}{T} \int_0^T f(x, \varphi_t^x(y)) dt = \int_{\mathbb{R}^m} f(x, y) \mu_x(dy) =: \bar{f}_{\mu_x}(x), \tag{2.24}$$

where equality in (2.24) only holds for μ_x -almost all y, and the (non-uniform) limit depends on our choice of μ_x and its respective domain of attraction, hence is different for different y's.

Moreover, the selection of a branch $\{\mu_x(dy): x \in \mathbb{R}^d\}$ of invariant measures can be made such that the vector field $\bar{f}_{\mu_x}(x)$ is so irregular that existence and uniqueness of solutions of the averaged equation cannot be assured.

Example: Let $\dot{y}_t = g(x, y_t) = xy_t - y_t^3$ in \mathbb{R}^1 for x > 0, and f be arbitrary. Then φ^x has the three Dirac measures $\mu_x^0 = \delta_0$ (unstable) and $\mu_x^{1,2} = \delta_{\pm\sqrt{x}}$ (stable) as invariant measures, so that the limits in (2.24) are

$$\bar{f}_{\mu_x^i}(x) = \begin{cases} \bar{f}_{\mu_x^0}(x) = f(x,0), & y = 0, \\ \bar{f}_{\mu_x^1}(x) = f(x,\sqrt{x}), & y > 0, \\ \bar{f}_{\mu_x^2}(x) = f(x,-\sqrt{x}), & y < 0. \end{cases}$$

Method of Averaging (A) for the general case

Here is a form of the Method of Averaging for the above situation which holds "modulo conditions": Select the family (μ_x) of invariant measures for the auxiliary weather dynamical system generated by (2.23). Then

$$\lim_{\varepsilon \to 0} x_t^{\varepsilon}(x, y) = \bar{x}_t(x) \tag{2.25}$$

on [0,T] for all $x \in \mathbb{R}^d$ and μ_x -almost all $y \in \mathbb{R}^m$ (other modes of convergence are also feasible), where $\bar{x}_t(x)$ is the solution of the averaged equation

$$\dot{\bar{x}}_t = \bar{f}_{\mu_{\bar{x}_t}}(\bar{x}_t), \quad \bar{x}_0 = x,$$
 (2.26)

 $\bar{f}_{\mu_x}(x)$ is defined by (2.24) and depends on the branch (μ_x) of invariant measures chosen.

As a result, there are typically many different averaged equations.

Suppose φ^x is a nice hyperbolic (or Axiom A, in particular Anosov) dynamical system on a compact Riemannian manifold M_x with normalized Lebesgue measure $m_x(dy)$. Then it has a particular invariant measure μ_x^{SRB} called the "physical" or SRB (Sinai-Ruelle-Bowen) measure (see Katok and Hasselblatt [21] or Viana [47]) which builds-up as the occupation measure of orbits $\varphi_t^x(y)$ for Lebesgue-almost all initial values y. In this case and with the choice $\mu_x = \mu_x^{\text{SRB}}$ we expect (2.25) to hold for all climate initial conditions x and Lebesgue-almost all weather initial conditions y.

Linear diffusion approximation (L) for the general case

There are also suitable versions of the Central Limit Theorem for the error in the Method of Averaging for the coupled system (2.21, 2.22). We refer to the work of Kifer [24, 25] for the case where g on the right-hand side of (2.22) is independent of x and where the fast motion is a hyperbolic dynamical system. Some hints are given in [26, Sect. 3] about how to derive a Central Limit Theorem for the fully coupled case.

Here again, the weather dynamical system φ^x at frozen climate x solving (2.23) has to be sufficiently "mixing" to ensure that for each fixed x

$$\zeta_t^{arepsilon,x}(y) := rac{1}{\sqrt{arepsilon}} \left(x(x,y) - ar{x}_t(x)
ight), \quad 0 \le t \le T,$$

converges weakly (in the sense that the sequence of distributions of $\zeta^{\varepsilon,x}$ on $C([0,T];\mathbb{R}^d)$ generated by (2.21,2.22) with $x_0=x$ and y_0 distributed according to $\mu_x(dy)$ converges weakly as $\varepsilon\to 0$) to the Ornstein-Uhlenbeck process ζ^x_t solving the linear SDE (2.12), where $\bar{x}_t(x)$ is the solution of the averaged equation $\dot{x}=\bar{f}_{\mu_{\bar{x}}}(\bar{x})$ based on the chosen reference measure μ_x . The definition of $\sigma(x)$ in (2.13) remains unchanged, the only difference being that the covariance is calculated with respect to the joint distribution of $\varphi^x_t(y_0)$ and y_0 where y_0 has distribution $\mu_x(dy)$. If φ^x is hyperbolic to ensure the existence of a unique SRB measure $\mu_x^{\rm SRB}$, then we expect situations in which $\mu_x^{\rm SRB}$ can be replaced in the convergence statement by the normalized Lebesgue measure $m_x(dy)$ in y space.

As a result, the linear diffusion approximation (L) given by $\bar{x}_t(x) + \sqrt{\varepsilon}\zeta_t^x$ for the slow component $x_t^{\varepsilon}(x,y)$ will make sense under certain conditions also for the fully coupled case. The linear SDE of which ζ_t^x is a solution remains the same as in the classical case.

Note, however, that there are in general many different (L) models as not just $\bar{x}_t(x)$, but also the coefficients $D\bar{f}$ and σ of the linear SDE (2.12) depend on the chosen branch μ_x of invariant measures.

Particular Case: The case

$$\dot{x}_t = f(y_t), \quad \dot{y}_t = rac{1}{arepsilon} g(y_t), \quad x_0 = x, \quad y_0 = y,$$

where $\dot{y}_t = g(y_t)$ generates a nice hyperbolic dynamical system $(t, y) \mapsto \varphi_t(y)$, has been investigated by many authors. For recent reviews see Denker [6] or Viana [47] and the references therein. Let μ^{SRB} be the SRB measure of φ . We average out y, i.e. consider

$$\lim_{T \to \infty} \frac{1}{T} \int_0^T f(\varphi_t(y)) dt = \int f(y) \mu^{\mathtt{SRB}}(dy) =: \mu^{\mathtt{SRB}}(f)$$

for Lebesgue-almost all y, hence $\dot{\bar{x}}_t = \mu^{\text{SRB}}(f)$ and $\bar{x}_t(x) = \mu^{\text{SRB}}(f)t + x$.

Since

$$x_t^arepsilon(x,y) = x + \int_0^t f(arphi_{rac{arepsilon}{arepsilon}}(y)) ds,$$

we have

$$\begin{split} \frac{1}{\sqrt{\varepsilon}} \left(x_t^{\varepsilon}(x,y) - \bar{x}_t(x) \right) &= \frac{1}{\sqrt{\varepsilon}} \int_0^t (f(\varphi_{\frac{s}{\varepsilon}}(y)) - \mu^{\text{SRB}}(f)) \, ds \\ &= \sqrt{\varepsilon} \int_0^{t/\varepsilon} (f(\varphi_s(y)) - \mu^{\text{SRB}}(f)) \, ds \\ &\Rightarrow \zeta_t, \end{split}$$

where $\zeta_t = \sigma W_t$, since $D\bar{f} \equiv 0$ here, and σ^2 is a constant matrix defined as in (2.13).

Nonlinear diffusion approximation (N) for the general case

The papers by Just, Kantz, Rödenbeck and Helm [19], Kantz, Just and Baba [20], Just, Gelfert, Baba, Riegert and Kantz [18] and Gelfert [11] formally derive the nonlinear diffusion approximation (N) given by Hasselmann's SDE (2.18) for the fully coupled system (2.21,2.22) through perturbation and averaging techniques on the level of the Fokker-Planck equation. Several toy as well as numerical examples are treated.

In the above papers, the following refinement of (N) is derived in the sense that also the drift is corrected by an ε -term (which was already used by Khasminskii [22]):

$$dz_t^{\varepsilon} = (\bar{f}(z_t^{\varepsilon}) + \varepsilon D(z_t^{\varepsilon}))dt + \sqrt{\varepsilon}\sigma(z_t^{\varepsilon}) dW_t, \quad z_0^{\varepsilon} = x,$$
(2.27)

where

$$D(x) := \int_0^\infty \mathbb{E}\left(Df(x, \varphi_t^x) - D\bar{f}(x)\right) (f(x, \varphi_0^x) - \bar{f}(x)) dt.$$

The refined model (2.27) proved to be superior to (N) in its long-term behavior for certain toy models, see Arnold [2]. There is hope to prove that z_t^{ε} approximates x_t^{ε} on the time interval $[0, T/\varepsilon]$ as $\varepsilon \to 0$ (see Kifer [28, Sect. 1]).

3 The Lorenz-Maas coupled atmosphere-ocean model

We now discuss the components of the coupled atmosphere-ocean model we shall study in this paper. This model was proposed by van der Schrier and van Veen [45] and couples the ocean model by Maas [33] with the Lorenz-84 model of the atmosphere [32]. This 6-dimensional model (3-dimensional slow ocean and 3-dimensional fast atmosphere) is considered the simplest known atmosphere-ocean model which is derived from first principles in a controlled manner.

Let us first mention that both components are β -plane approximations¹ at mid-latitudes of the northern hemisphere, centered near $45^{\circ}N$. More precisely, we suppose that the origin of our coordinate system (x, y, z) lies at the barycenter of an ocean box D of length and width W and height H, i.e.

$$D = \{(x, y, z) : -\frac{W}{2} \le x, y \le \frac{W}{2}, -\frac{H}{2} \le z \le \frac{H}{2}\}.$$

We choose $W = 5 \times 10^6 \, m$ and $H = 5 \times 10^3 \, m$ in our simulations. The quantities x and y are the horizontal coordinates, where x is the zonal (eastward), y the meridional (northward) one, while z is the vertical coordinate.

Let A denote the interface of the ocean box with a very shallow surface layer of the atmosphere of height about $10 \, m$. The frame of our atmosphere model is composed of multi- (two-) layer planes E_1 and E_2 parallel to A located next to each other at a height of more than $100 \, m$ above ocean level and centered as well at 0. These planes are supposed to be wider than the ocean box, to allow to take into account some orographic forcing of the free atmosphere which is observed in this multi-layer system. This forcing will be caused by a temperature contrast between continents supposed to lie somewhere off the plane A on the one side and the ocean on the other side. The ocean inside D will be forced by a surface wind from inside the shallow surface layer. Atmosphere and ocean are coupled by mechanisms to be specified below, but there will be no interaction between the shallow surface layer and the free atmosphere above. To get a rough idea of the model components, consult Fig. 1.

The atmosphere component is given by the Lorenz-84 model [32]. It is derived by starting with the stream functions $\psi_i(x,y)$ in plane E_i , i=1,2, which comes from the quasigeostrophic (i.e. the isobars are almost parallel to the flow lines) vorticity equation of the atmosphere. Stream functions ψ in β -planes such as the ones given reproduce the flow velocity components in direction x proportional to $\frac{\partial \psi}{\partial x}$ and in direction y proportional to $\frac{\partial \psi}{\partial x}$.

Now we Fourier analyze the stream function of the atmosphere, i.e. expand it into a series in terms of the complex exponentials $\exp(i(mx+ny))$, $m,n\in\mathbb{Z}^+$. Call the purely time dependent coefficients of this expansion $\psi(m,n)$, $m,n\in\mathbb{Z}^+$, and transfer the vorticity equation into simple differential equations for the coefficient functions. Then the Lorenz-84 model just retains the differential equations for $X=\psi(0,1)$, $Y=\operatorname{Re}(\psi(1,1))$, and $Z=\operatorname{Im}(\psi(1,1))$. X being a purely y-dependent wave on the stream function level, which results in its corresponding northward component of the velocity to be zero and therefore represents the jet stream called westerly. Y and Z correspondingly represent baroclinic waves with wave number 1 in the meridional direction. The resulting coupled system of three differential equations is of the form

$$\dot{X} = -Y^2 - Z^2 - aX + aF,$$

$$\dot{Y} = XY - bXZ - Y + G,$$

$$\dot{Z} = bXY + XZ - Z.$$
(3.1)

Let us briefly explain the forcing terms F and G and the parameters a and b. G describes the influence of orography (structure of continents) on the atmospheric flow in the form of an averaged temperature contrast between sea and continents. It is obtained by taking a rough phenomenological functional description of this contrast along sea shores described in the horizontal variables (x, y) in an extension of A below E_1 , Fourier analyzing this function in an analogous way as indicated above for the stream function, and retaining the term corresponding to m = n = 1. The forcing term F depicts the influence of the north-south temperature contrast due to the variation of the intensity of solar heating with the meridional position y. The time scale in our system of differential equations is set such as to have damping rate 1 for dissipation of Y and Z. Hence a is the scaling of damping of the westerly jet X with respect to the dissipation rate of Y and Z. The quantity b gives the scale of the strength of the exchange of energy between the westerly jet and the baroclinic waves Y and Z.

Let us next discuss the *ocean component* originating from a model by Maas ([33], [34]). This model considers the ocean in the box D as being forced by wind from the shallow surface layer above A, and by buoyancy due to heating from above the ocean surface A. The starting point for deriving this box model in D is the momentum equation for the ocean flow (u, v, w) derived from the usual Navier-Stokes equation in rotating coordinate frames

 $^{^{1}}$ A β -plane is a plane on which the variation of the Coriolis force with latitude is taken into account in first order. It is often used when describing mid-latitude atmospheric dynamics, see van Veen, Opsteegh and Verhulst [46].

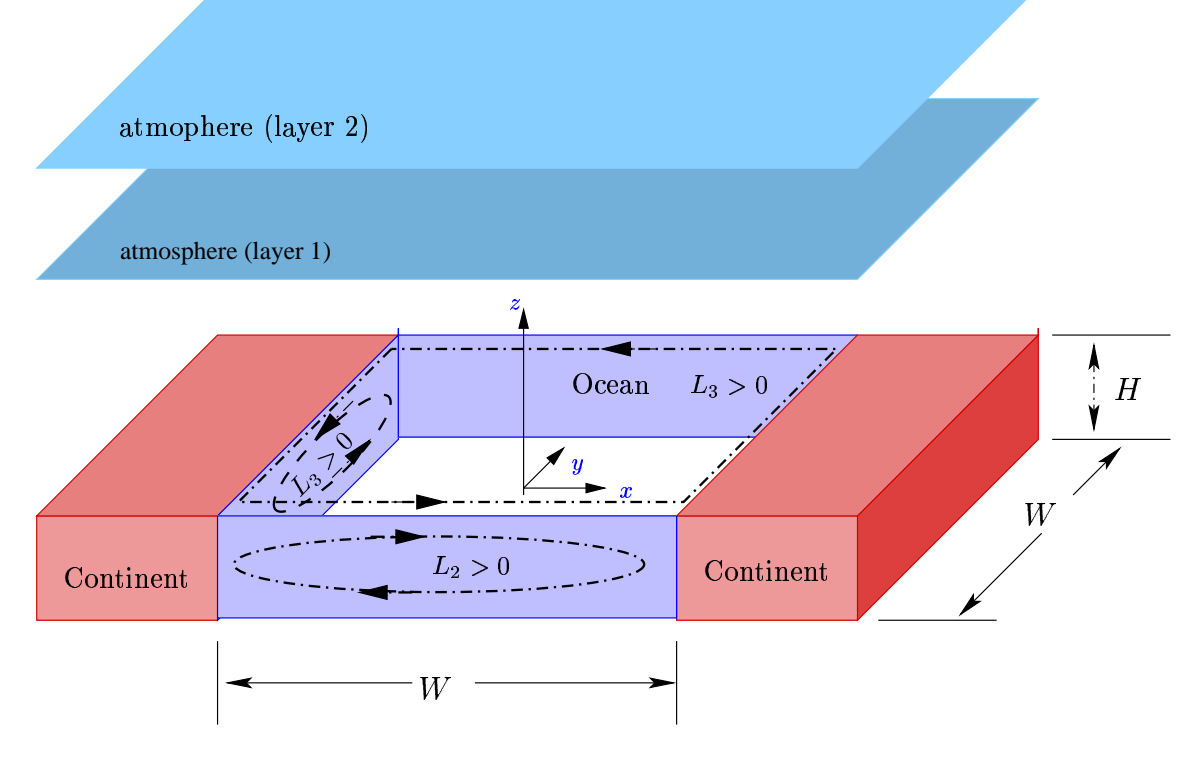


Figure 1: Illustration of the components of the Lorenz-Maas model

on the one hand, and the continuity equation of the diffusion type for the mass density ρ in the ocean on the other hand. Now these basic equations are transformed in the following way. By taking the vector (L_1, L_2, L_3) as being the average over D of the angular momentum $(x, y, z) \times (u, v, w)$ induced by the ocean flow (u, v, w) with respect to the origin in the center of D, the momentum equation becomes a differential equation for the average angular momentum which is forced by a torque due to the surface wind. L_1 describes meridional circulation. $L_1 < 0$ corresponds to a direct thermally-driven overturning, i.e. rising water in the south and sinking water in the north. L_2 , acting in the zonal plane, plays the role of "steering wheel" to L_1 indicating in which zonal parts large scale sea water sinking occurs. L_3 stands for horizontally wind-driven ocean circulation (see also Öllers [38]). Referring to hydrostatic balance, the (time) average density ρ_0 is assumed to only depend on z. Now the fluctuating residual density $\rho - \rho_0$ is expanded in terms of $x^k y^l z^m$ around the origin with purely time dependent coefficients $\rho_{(k,l,m)}$, $k,l,m \geq 0$, and, denoting $\rho_1 := \rho_{(1,0,0)}$, $\rho_2 := \rho_{(0,1,0)}$, $\rho_3 := \rho_{(0,0,1)}$, is approximated by

$$\rho(x, y, z, \cdot) - \rho_0(z) = x\rho_1 + y\rho_2 + z\rho_3, \quad (x, y, z) \in D.$$

Then the continuity equation turns into a differential equation for the density "gradient" (ρ_1, ρ_2, ρ_3) , forced by a buoyancy term. Since the influence of salinity is neglected, density is determined by temperature alone, and the equation for the density gradient may be considered an equation for heat diffusion in the ocean box D.

After choosing appropriate scales (for details see Maas [33] and van Veen [45]), the transformations of momentum and continuity equations yield the system

$$\frac{1}{P}\frac{d}{dt}L_{1} - fL_{2} = -\rho_{2} - L_{1},$$

$$\frac{1}{P}\frac{d}{dt}L_{2} + fL_{1} = \rho_{1} - L_{2},$$

$$\frac{1}{P}\frac{d}{dt}L_{3} = -rL_{3} - T,$$
(3.2)

$$\frac{d}{dt}\rho_1 + (\rho_2 L_3 - \rho_3 L_2) = -\rho_1,
\frac{d}{dt}\rho_2 + (\rho_3 L_1 - \rho_1 L_3) = -\rho_2 + RB_2,$$
(3.3)

$$\frac{d}{dt}\rho_3 + (\rho_1 L_2 - \rho_2 L_1) = -\mu \rho_1 + RB_3.$$

Let us comment on the forcing terms. The simple constant torque of strength T acts in negative z-direction and consequently generates a clockwise circulation around the origin in D interpreted as the usual westerlies (eastbound wind) in high latitudes and easterlies (westbound wind) in low latitudes. It can be considered as being created by the north-south temperature gradient which induces a northward flow. This flow is deflected eastward by the Coriolis force thus accounting for the westerlies at high latitudes, and at the same time establishing a north-south pressure gradient. The resulting southward flow is deflected west by the Coriolis force finally inducing the easterlies at low latitudes.

It is reasonable to assume that the averaged buoyancy flux, also related to the north-south temperature gradient, has principally a meridional, northward directed component B_2 which is usually given by the average of $Ky\rho_2$ over the box, with a diffusion rate K. Though surface cooling or evaporation is small compared to B_2 , it may influence the vertical stratification of the sea. For example, it may play an important role in deep-water formation like in the Labrador Sea (see Weaver and Sarachik [49] and Weaver, Aura and Myers [48]). So we keep the vertical component of the buoyancy flux B_3 and assume it be a constant at least one order smaller than B_2 .

The parameters appearing in the differential equations (3.2) and (3.3) have the following significance. P denotes the $Prandtl\ number$ describing the ratio of horizontal diffusion and damping, f is the $Coriolis\ parameter$, scaled by the friction rate of horizontal angular momentum. The $Rayleigh\ number\ R$ measures the strength of the buoyancy forcing in the northward (y) direction. Further, r gives the ratio of friction strength in the vertical and horizontal directions, and correspondingly μ is the ratio of diffusion coefficients in these directions.

We now come to a major point in simplifying the 6-dimensional ocean system derived above. Since $P \approx 10^4$ is quite large in realistic situations, it is reasonable to ignore the inertia of the angular momentum through the approximation $P = \infty$. Therefore the average angular momentum can be expressed as a function of the components of the density gradient as follows:

$$L_1 = \frac{-\rho_2 + f\rho_1}{1 + f^2}, \quad L_2 = \frac{\rho_1 + f\rho_2}{1 + f^2}, \quad L_3 = -T/r.$$
 (3.4)

Rescaling density and Rayleigh number by the factor $1 + f^2$ and keeping their names then provides the simplified 3-dimensional system

$$\dot{\rho}_{1} = \frac{T}{r}\rho_{2} + \rho_{1}\rho_{3} + f\rho_{2}\rho_{3} - \rho_{1},$$

$$\dot{\rho}_{2} = -\frac{T}{r}\rho_{1} + \rho_{2}\rho_{3} - f\rho_{1}\rho_{3} - \rho_{2} + RB_{2},$$

$$\dot{\rho}_{3} = -\rho_{1}^{2} - \rho_{2}^{2} - \mu\rho_{3} + RB_{3}.$$
(3.5)

It will be more convenient to absorb the terms containing T and to adjust the dissipation parameters in the first two equations to be 1 through the transformation

$$\rho_3 \to -\frac{T}{rf} + \Lambda \rho_3$$
, where $\Lambda = 1 + \frac{T}{rf}$.

Then, again keeping the names for the variables and parameters, we obtain the final form of the ocean component of our coupled system

$$\dot{\rho}_{1} = \rho_{1}\rho_{3} + f\rho_{2}\rho_{3} - \rho_{1},
\dot{\rho}_{2} = \rho_{2}\rho_{3} - f\rho_{1}\rho_{3} - \rho_{2} + RB_{2},
\dot{\rho}_{3} = -k_{4}(\rho_{1}^{2} + \rho_{2}^{2}) - \mu\rho_{3} + c,$$
(3.6)

where $R \to \Lambda^{-1}$, $k_4 = \Lambda^{-2}$, $\mu \to \mu \Lambda^{-1}$, and $c = (RB_3 + \mu T/rf)\Lambda^{-2}$, where c describes a combination effect of the vertical angular momentum and the vertical buoyancy flux.

We finally come to the assumptions about the *coupling* of the atmosphere and ocean components. To model the influence of the atmosphere on the ocean and of the ocean on the atmosphere we take (see van Veen [45])

1.
$$B_2 = 1 + \frac{1}{R}(k_1X - k_3\rho_2)$$
, and

2.
$$F = F_0 + k_2 \rho_2$$
.

The modification of the northward wind forcing contained in the assumption (1) on B_2 just describes a heat flux transferred by the free atmosphere to the ocean. The assumption (2) on F contains a constant meridional gradient F_0 of solar heating, augmented by a term of heat transferred from the ocean. We introduce the scale factor ε to denote the ratio of the well separated time scales of atmospheric and oceanic motion, and replace the coupling constant $1 + k_3$ by k_3 to obtain the equations of the coupled atmosphere-ocean Lorenz-Maas model as follows:

$$\dot{\rho}_{1} = \rho_{1}\rho_{3} + f\rho_{2}\rho_{3} - \rho_{1},
\dot{\rho}_{2} = \rho_{2}\rho_{3} - f\rho_{1}\rho_{3} - k_{3}\rho_{2} + R + k_{1}X,
\dot{\rho}_{3} = -k_{4}(\rho_{1}^{2} + \rho_{2}^{2}) - \mu\rho_{3} + c,$$
(3.7)

$$\varepsilon \dot{X} = -Y^2 - Z^2 - aX + aF_0 + k_2 \rho_2,
\varepsilon \dot{Y} = XY - bXZ - Y + G,
\varepsilon \dot{Z} = bXY + XZ - Z.$$
(3.8)

Representative practical choices of the parameters in the model are given in Table 1.

a = 0.25	b=4	G = 1
$F_0 = O(1)$	$k_1 = O(10)$	$k_2 = O(1)$
$k_3 = O(1)$	$k_4 = O(1)$	$\mu = 1$
f = 20	R = O(10)	c = O(1)
$\varepsilon = 3.0 \times 10^{-5}$	T = O(10)	r = 1

Table 1: Characteristic parameters of the Lorenz-Maas model

4 Dynamics and bifurcation of the Lorenz-Maas model

In this section we shall deal with the deterministic coupled model (3.7,3.8), with an emphasis on long time behavior of its dynamics and on qualitative changes (bifurcations). We first prove the existence of a global attractor. We then turn to the study of the bifurcation scenarios.

However, the smallness of realistic ε relating the time scales of the atmospheric variables of the coupled model to the one of the climate variables makes its bifurcation analysis numerically a rather difficult task. We will therefore study its dynamics and bifurcation separately in the slow and fast submodels.

4.1 Existence of a global attractor

The following key result will turn out to be very valuable for the subsequent treatment of invariant measures and bifurcation analysis: the existence of a global absorbing set of the coupled system which is independent of the scaling parameter ε . We will construct it along a well known string of arguments: By means of an energy type inequality it will follow that there is an absorbing set, uniformly in ε . Then there is a standard argument obtaining the attractor as an inferior limit of the absorbing set transported by the flow of the system. The uniformity in ε of the absorbing set will be inherited by the attractor.

This result is not only of theoretical importance. Practically, it will facilitate considerably our task taken on in subsequent sections of numerically determining invariant measures of the weather subsystem: for instance, running the box division algorithm GAIO to obtain invariant measures, we may initially choose boxes containing just the absorbing set.

Note that the time scale ratio ε relating atmosphere and ocean variables is rather small. In the sequel, we shall therefore assume that $\varepsilon \leq 1$.

Theorem (Existence of global attractor of the Lorenz-Maas model)

The dynamical system (3.7,3.8) possesses a bounded absorbing set $S \subset \mathbb{R}^6$ which is independent of $0 < \varepsilon \le 1$. Moreover, for any $0 < \varepsilon \le 1$ there exists a global attractor A_{ε} contained in S. In particular, all solutions of (3.7,3.8) are global forward in time, i.e. they exist for all times $t \ge 0$.

Proof: Let λ be a real parameter to be specified later. In order to obtain an energy type inequality, we multiply the equations (3.7) by ρ_1 , ρ_2 and $\rho_3 + \lambda$, respectively, and add up the resulting equations to obtain

$$\frac{1}{2} \frac{d}{dt} \left(\rho_1^2 + \rho_2^2 + \frac{1}{k_4} (\rho_3 + \lambda)^2 \right)
= -((1+\lambda)\rho_1^2 + (k_3 + \lambda)\rho_2^2 + \frac{\mu}{k_4} (\rho_3 + \lambda)^2)
+ \frac{\mu\lambda + c}{k_4} (\rho_3 + \lambda) + R\rho_2 + k_1 X \rho_2 + \frac{c}{k_4} \rho_3.$$
(4.1)

We estimate the non-quadratic terms on the right hand side of this equation via the simple inequality

$$ab \le \frac{a^2}{2c} + \frac{cb^2}{2}$$

valid for a, b real and c > 0. Hence there is a constant C_1 independent of ε such that

$$\frac{1}{2} \frac{d}{dt} \left(\rho_1^2 + \rho_2^2 + \frac{1}{k_4} (\rho_3 + \lambda)^2 \right)
\leq -\left(\left(\frac{1}{2} + \lambda \right) \rho_1^2 + (k_3 + \frac{\lambda}{2}) \rho_2^2 + \frac{\mu}{2k_4} (\rho_3 + \lambda)^2 \right) + \frac{k_1^2}{2\lambda} X^2 + C_1.$$

In a similar way we multiply the equations (3.8) by X, Y, and Z, respectively, add up and estimate to obtain with a constant C_2 independent of ε and λ

$$\frac{\varepsilon}{2} \frac{d}{dt} \left(X^2 + Y^2 + Z^2 \right) = -(aX^2 + Y^2 + Z^2) + k_2 X \rho_2 + aF_0 X + GY
\leq -\left(\frac{a}{2} X^2 + \frac{1}{2} Y^2 + Z^2 \right) + \frac{k_2^2}{a} \rho_2^2 + C_2.$$
(4.2)

Now we add the two inequalities (4.1) and (4.2) to deduce

$$\begin{split} &\frac{1}{2}\frac{d}{dt}\left(\rho_1^2+\rho_2^2+\frac{1}{k_4}(\rho_3+\lambda)^2+\varepsilon(X^2+Y^2+Z^2)\right)\\ &\leq &-\left((\frac{1}{2}+\lambda)\rho_1^2+(k_3+\frac{\lambda}{2}-\frac{k_2^2}{a})\rho_2^2+\frac{\mu}{2k_4}(\rho_3+\lambda)^2\right.\\ &+\left.(\frac{a}{2}-\frac{k_1^2}{2\lambda})X^2+\frac{1}{2}Y^2+Z^2\right)+C_1+C_2\\ &\leq &-L\left(\rho_1^2+\rho_2^2+\frac{1}{k_4}(\rho_3+\lambda)^2+\varepsilon(X^2+Y^2+Z^2)\right)+C, \end{split}$$

with

$$L = \min\left(\frac{1}{2}, k_3 + \frac{\lambda}{2} - \frac{k_2^2}{a}, \frac{a}{2} - \frac{k_1^2}{2\lambda}, \frac{\mu}{2k_4}\right), \quad C = C_1 + C_2.$$

To be sure that L > 0 we have to choose our free parameter λ big enough. Now Gronwall's inequality entails the estimate

$$\left(\rho_1^2 + \rho_2^2 + \frac{1}{k_4}(\rho_3 + \lambda)^2 + \varepsilon(X^2 + Y^2 + Z^2)\right)(t)
\leq \left(\rho_1^2 + \rho_2^2 + \frac{1}{k_4}(\rho_3 + \lambda)^2 + \varepsilon(X^2 + Y^2 + Z^2)\right)(0)\exp(-2Lt) + \frac{C}{L}.$$
(4.3)

So there exists $t_0 > 0$ such that for all $t \geq t_0$ we have

$$\left(\rho_1^2 + \rho_2^2 + \frac{1}{k_4}(\rho_3 + \lambda)^2 + \varepsilon(X^2 + Y^2 + Z^2)\right)(t) \le 1 + \frac{C}{L}.$$
(4.4)

In particular, ρ_2 is bounded by a constant not depending on ε . Using this fact in (4.2) and recalling $\varepsilon \leq 1$ we obtain

$$\frac{\varepsilon}{2} \frac{d}{dt} (X^2 + Y^2 + Z^2) \le -M(X^2 + Y^2 + Z^2) + D,$$

with $M = \min(\frac{a}{2}, \frac{1}{2})$ and a constant D independent of ε . Therefore another application of Gronwall's inequality yields the estimate

$$(X^2 + Y^2 + Z^2)(t) \le (X^2 + Y^2 + Z^2)(0) \exp(-\frac{2M}{\varepsilon}t) + \frac{D}{M},$$
 (4.5)

and thus there will be $t_1>0$ not depending on ε such that for $t\geq t_1$

$$(X^2 + Y^2 + Z^2)(t) \le 1 + \frac{D}{M}. (4.6)$$

We see from (4.4) and (4.6) that the solutions of the dynamical system (3.7,3.8) are absorbed by the compact set

$$S = \left\{ (X, Y, Z, \rho_1, \rho_2, \rho_3) \in \mathbb{R}^6 : \right.$$

$$X^2 + Y^2 + Z^2 \le 1 + \frac{D}{M}, \ \rho_1^2 + \rho_2^2 + \frac{1}{k_4} (\rho_3 + \lambda)^2 \le 1 + \frac{C}{L} \right\}$$

uniformly in ε . Moreover, according to a standard argument (see for example Temam [44, Theorem 1.1.1]) for any $\varepsilon \leq 1$ the Lorenz-Maas model possesses a global attractor A_{ε} contained in S. This completes the proof.

4.2 Dynamics and bifurcation of the Maas ocean model

In this subsection we freeze the coupling atmosphere term in the ocean model, and consider it as a bifurcation parameter in the dynamics of the latter. We do a detailed bifurcation analysis of the Maas model using the package AUTO while varying this parameter which will be denoted by $\alpha := R + k_1 X$. It represents the frozen meridional component of the buoyancy flux. We therefore consider the following family of differential equations representing the density variables (ρ_1, ρ_2, ρ_3)

$$\dot{\rho}_{1} = \rho_{1}\rho_{3} + f\rho_{2}\rho_{3} - \rho_{1}
\dot{\rho}_{2} = \rho_{2}\rho_{3} - f\rho_{1}\rho_{3} - k_{3}\rho_{2} + \alpha
\dot{\rho}_{3} = -k_{4}(\rho_{1}^{2} + \rho_{2}^{2}) - \mu\rho_{3} + c$$
(4.7)

parametrized by α .

Note first that the system possesses symmetry properties. If α is replaced by $-\alpha$, we see that $(-\rho_1, -\rho_2, \rho_3)$ instead of (ρ_1, ρ_2, ρ_3) satisfies equation (4.7). Accordingly, our bifurcation diagram should be antisymmetric for passing from ρ_1 resp. ρ_2 to their negatives, but symmetric when replacing ρ_3 with $-\rho_3$. It is therefore sufficient if we restrict our bifurcation studies to α on the positive half line. Corresponding diagrams for negative α may be obtained by the symmetries just explained. In the two sets of simulations presented we choose the parameters in the following way: f = 20, $k_3 = 1$, $\mu = 1$, $k_4 = 1/3$, and either c = 1 or c = 5. The bifurcation parameter α varies continuously in the interval [0,75]. In the following diagrams, solid curves represent stable steady state branches, dashed curves represent unstable steady state branches. Full discs stand for stable limit cycle branches, empty discs for unstable ones.

Let us first explain the diagrams in the case c=1. Two solution branches coexist. One is related to limit cycles (Fig. 2), the other one to steady states (Fig. 3). The limit cycle branch is globally stable. Its period changes very slowly along with the maximum of ρ_3 , while the maxima of ρ_1 and ρ_2 fluctuate rapidly. The steady state branch starts from zero with α , and is stable as α increases. At $\alpha=13.34$ it undergoes a saddle-node bifurcation (lab. SN5) where it loses its stability. It regains stability as it crosses another saddle-node bifurcation point at $\alpha=1.73$ (lab. SN6). Stability of this branch is further interrupted for $\alpha \in (1.85, 47.38)$ which is bounded by two Hopf bifurcation points denoted HB7 and HB8 in the diagrams.

The limit cycle branch originating in HB7 (Fig. 4) is stable until it crosses two period doubling points (lab. PD9 and PD10). They are connected to another stable limit cycle branch with approximately double period. The limit cycle branch originating in HB8 (Fig. 5) is stable as α decreases until it hits a period doubling point (lab.

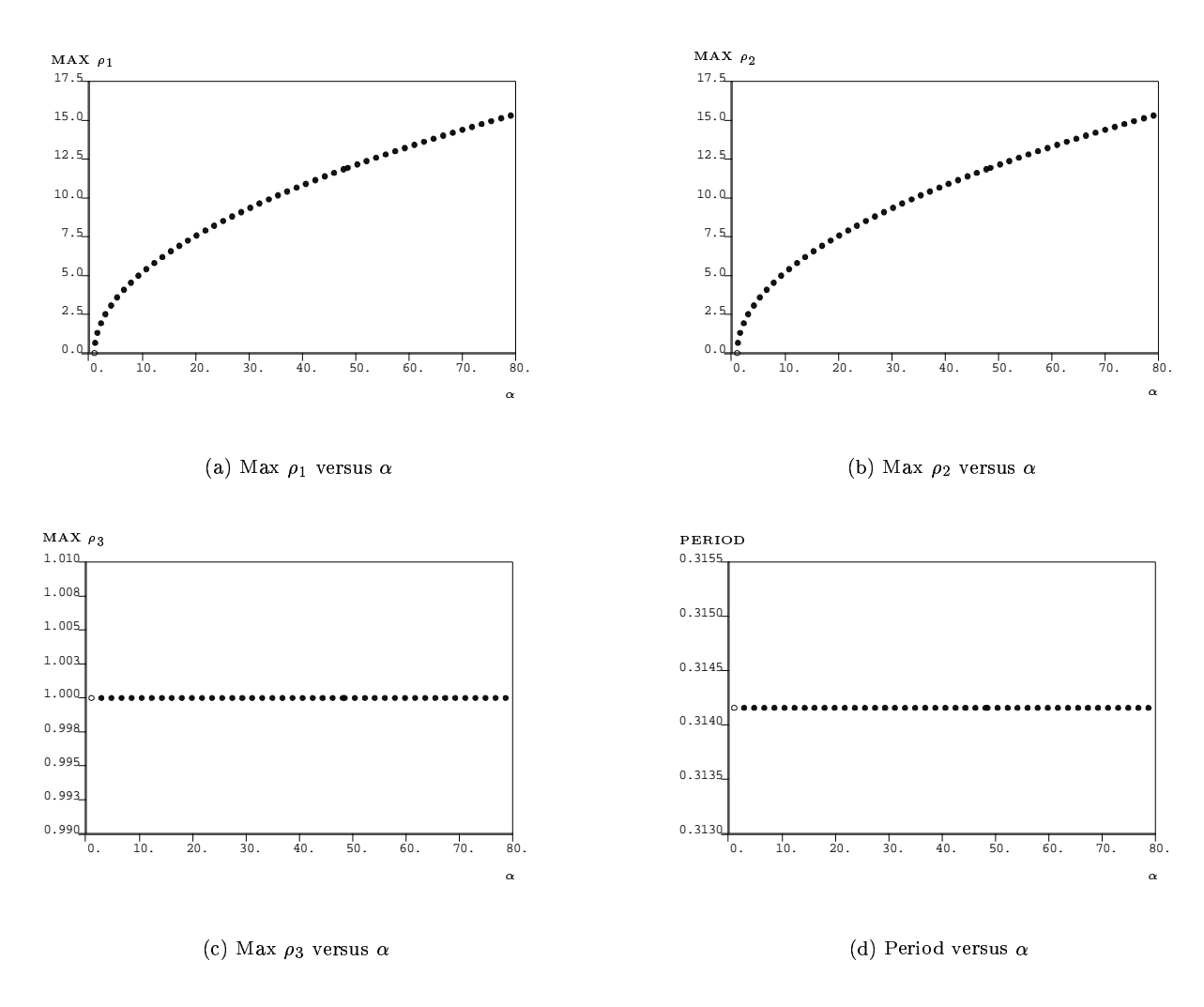


Figure 2: Continuation of limit cycle branch of Maas model with c=1

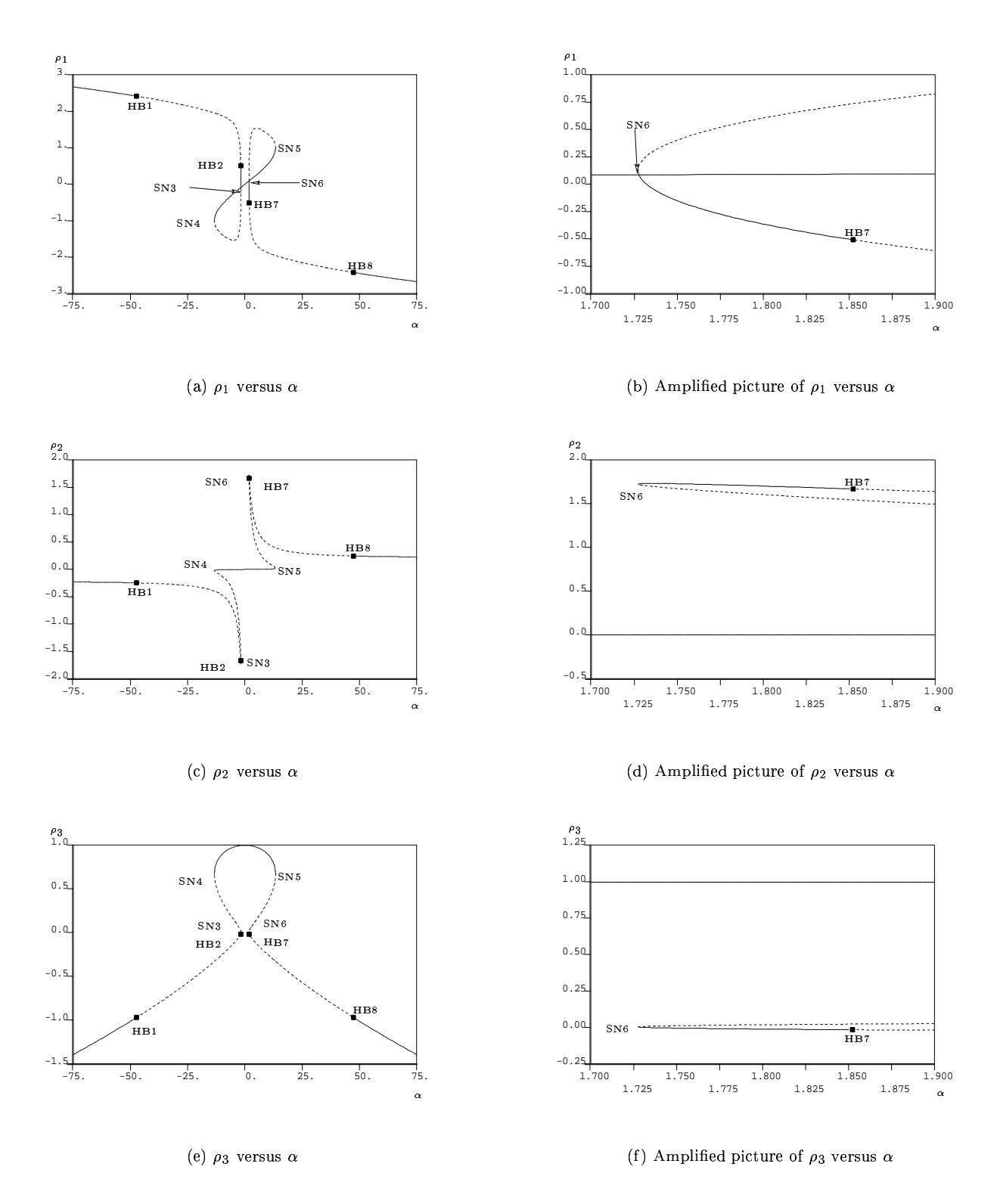


Figure 3: Steady state bifurcation diagram of Maas model with c=1

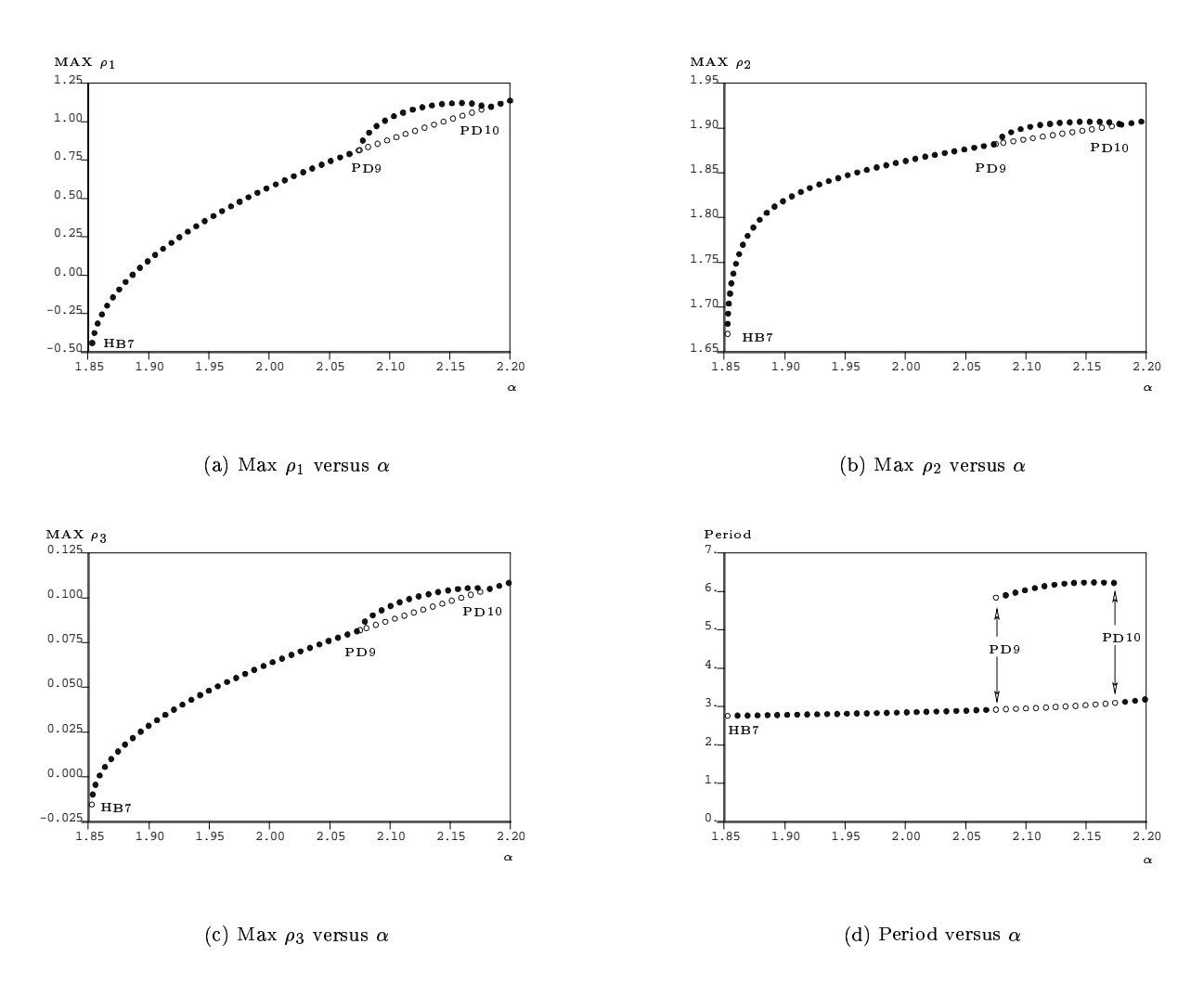


Figure 4: Continuation of limit cycle branches of Maas model from HB7 and PD9 with c=1

PD11). Another stable limit cycle branch with approximately double period appears on the left hand side of the period doubling point. It is stable until it hits another period doubling point (lab. PD12) triggering still another stable limit cycle branch with approximately double period to its left. This period doubling process continues until the system becomes chaotic. Let us now pass to the diagrams for c = 5. There are again two coexisting

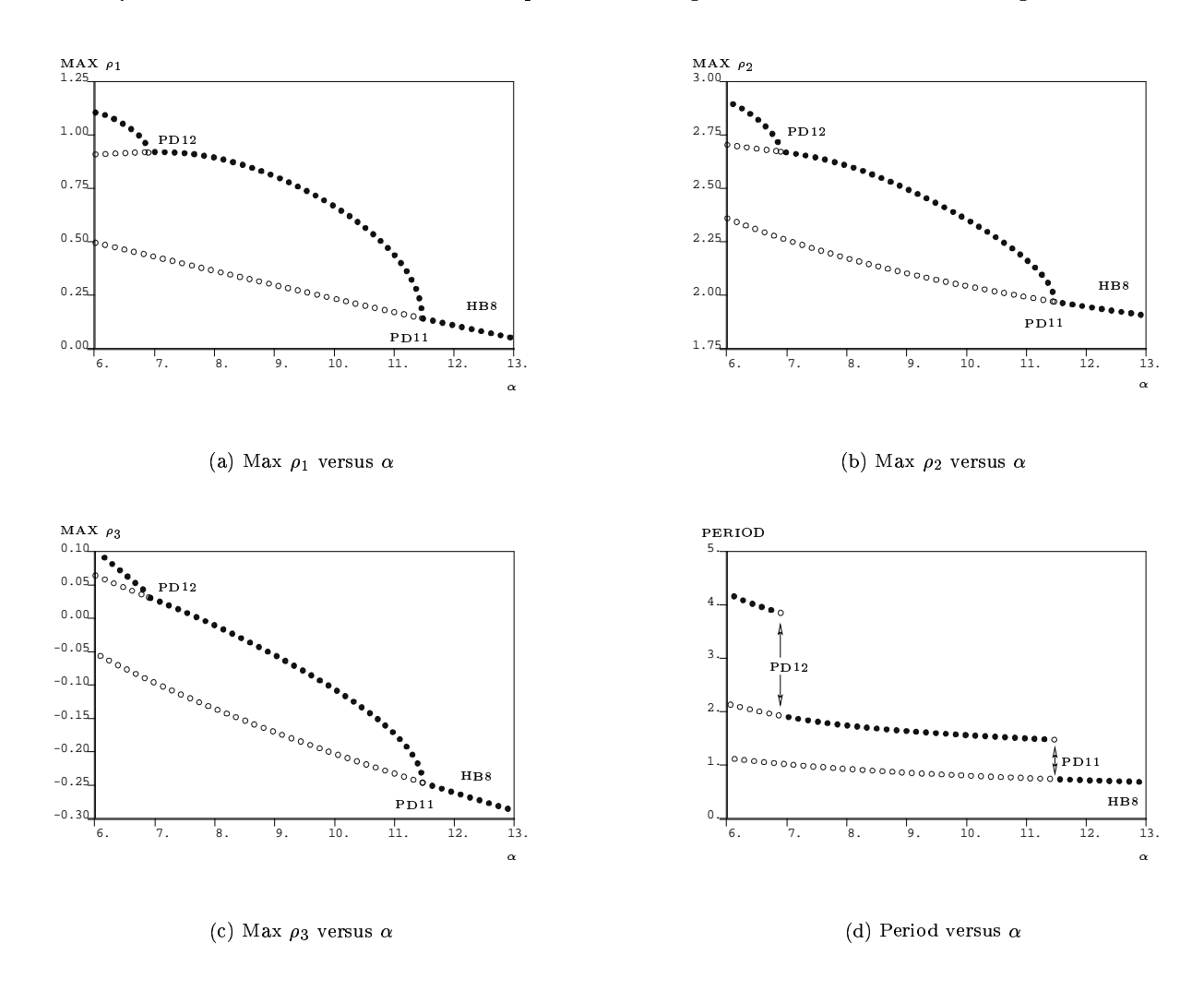


Figure 5: Continuation of limit cycle branches of Maas model from HB8, PD11 and PD12 with c=1

solution branches as α varies in [0,75]. One is a limit cycle branch (Fig. 6), the other one is associated with steady states (Fig. 7). In contrast to the globally stable situation in the preceding scenario the limit cycle branch becomes unstable as α grows and crosses a torus bifurcation (lab. TR1). The steady state branch is unstable until it runs through a saddle-node bifurcation point at $\alpha = 3.87$ (lab. SN4). Stability is further interrupted in an interval bounded by two Hopf bifurcation points located at $\alpha = 3.94$ (lab. HB5) and $\alpha = 206.53$ (lab. HB6).

The limit cycle branch starting from HB5 (Fig. 8) is stable as α increases until it encounters a period doubling point (lab. PD7), and transfers its stability to another limit cycle with approximately double period. The stability of this limit cycle branch is further interrupted on an interval bounded by two period doubling points (lab. PD8 and PD9). Another stable limit cycle with approximately double period emerges and connects these two period doubling points. The limit cycle branch generated at HB6 (Fig. 9) is stable as α decreases until it encounters a period doubling point (lab. PD10). Another stable limit cycle branch with approximately double period appears on the left hand side of the point. It is stable until α hits another period doubling point (lab. PD11), on the left side of which again a stable limit cycle branch with approximate double period appears. This pattern is repeated over and over.

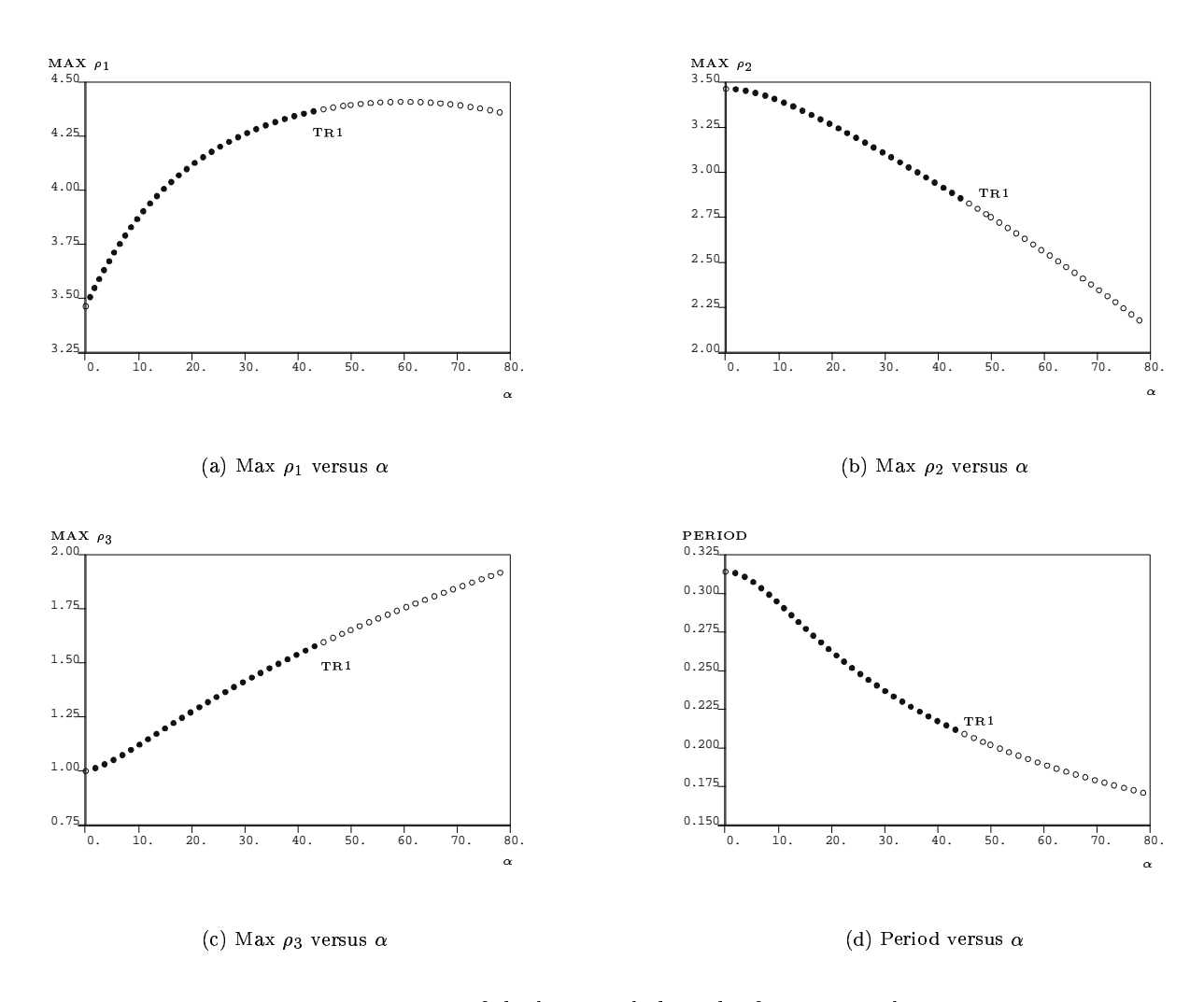


Figure 6: Continuation of the limit cycle branch of Maas model with c=5

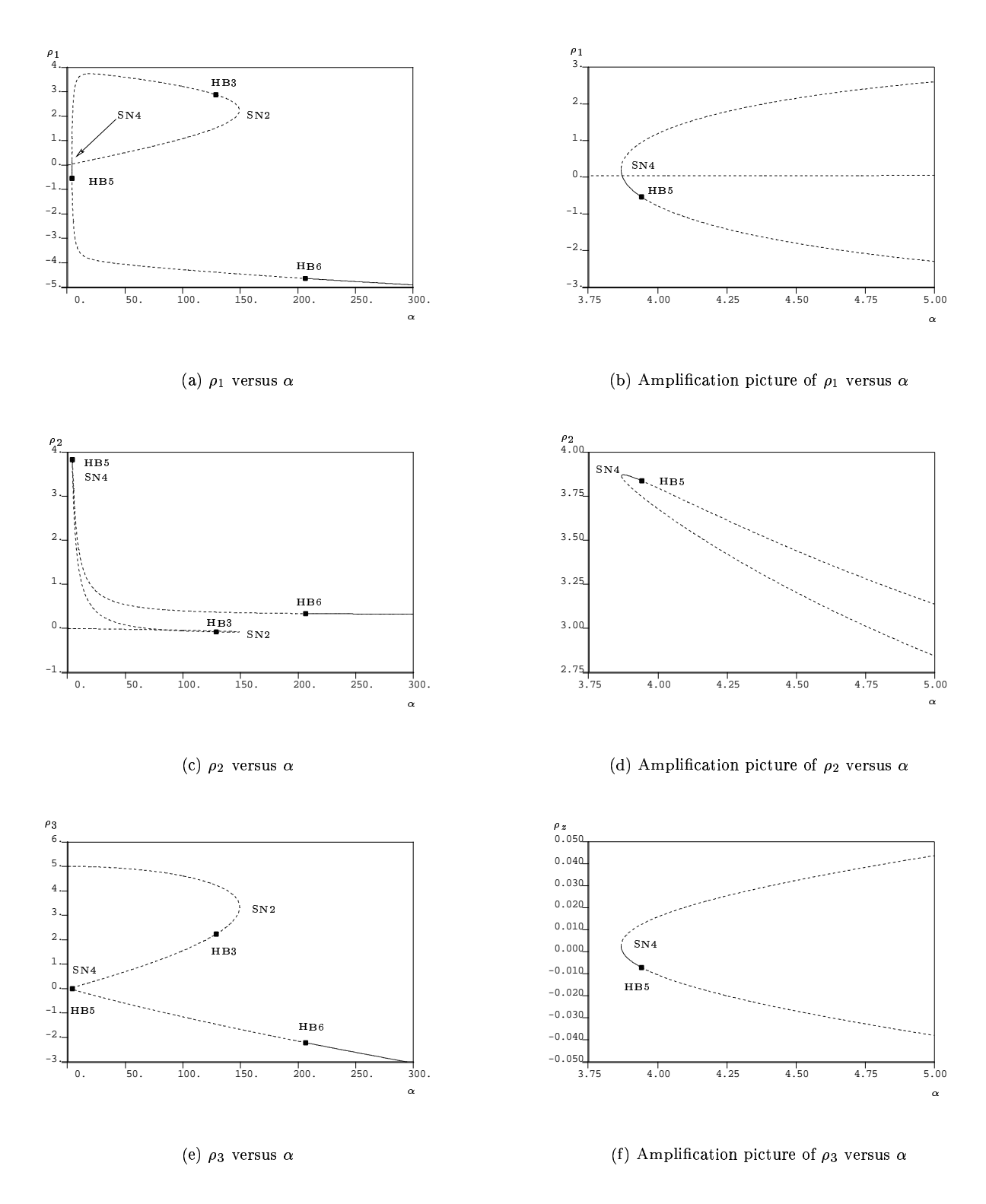


Figure 7: Steady states bifurcation diagram of Maas model with $c=5\,$

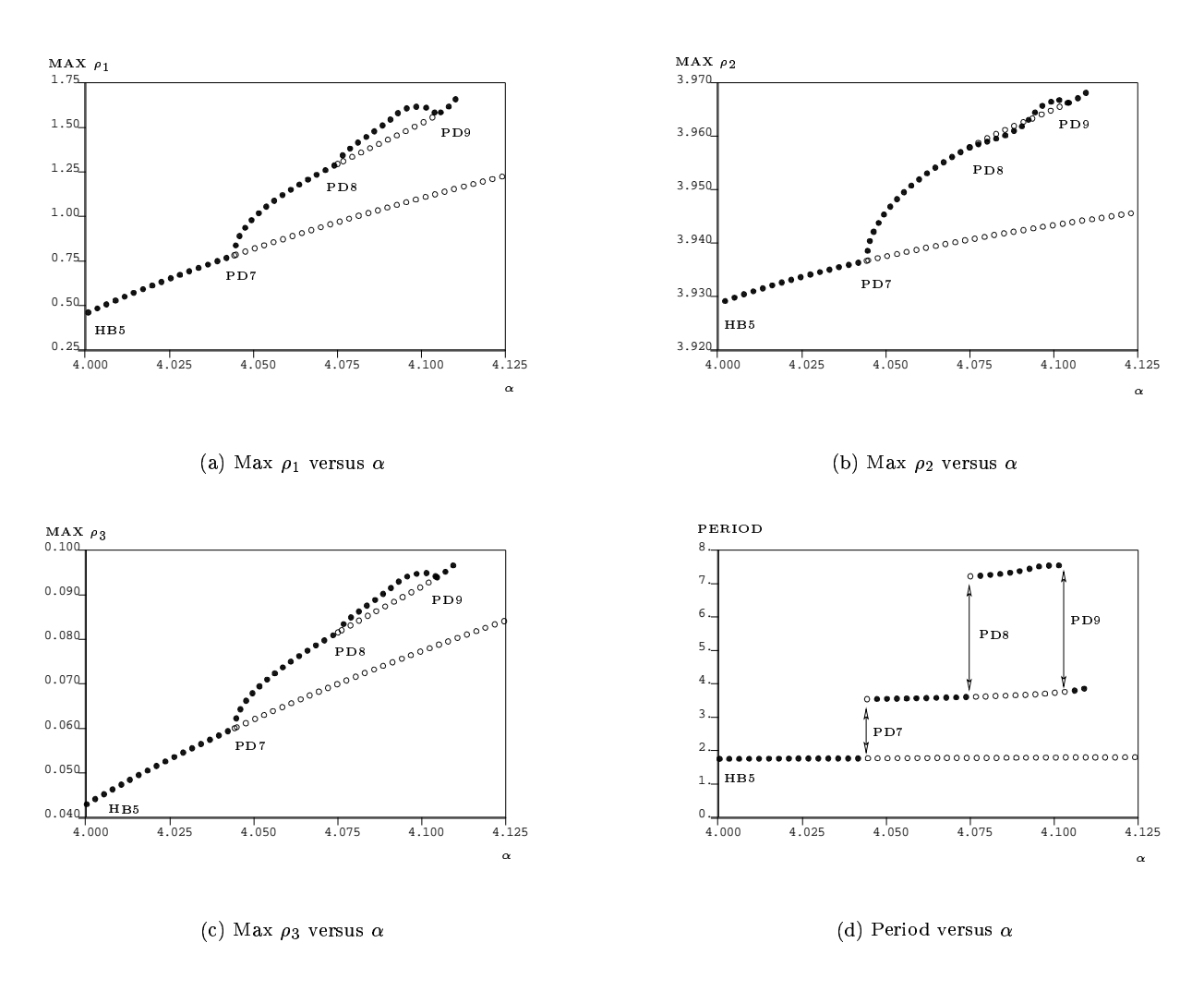


Figure 8: Continuation of limit cycle branch of Maas model from HB5 with c=5

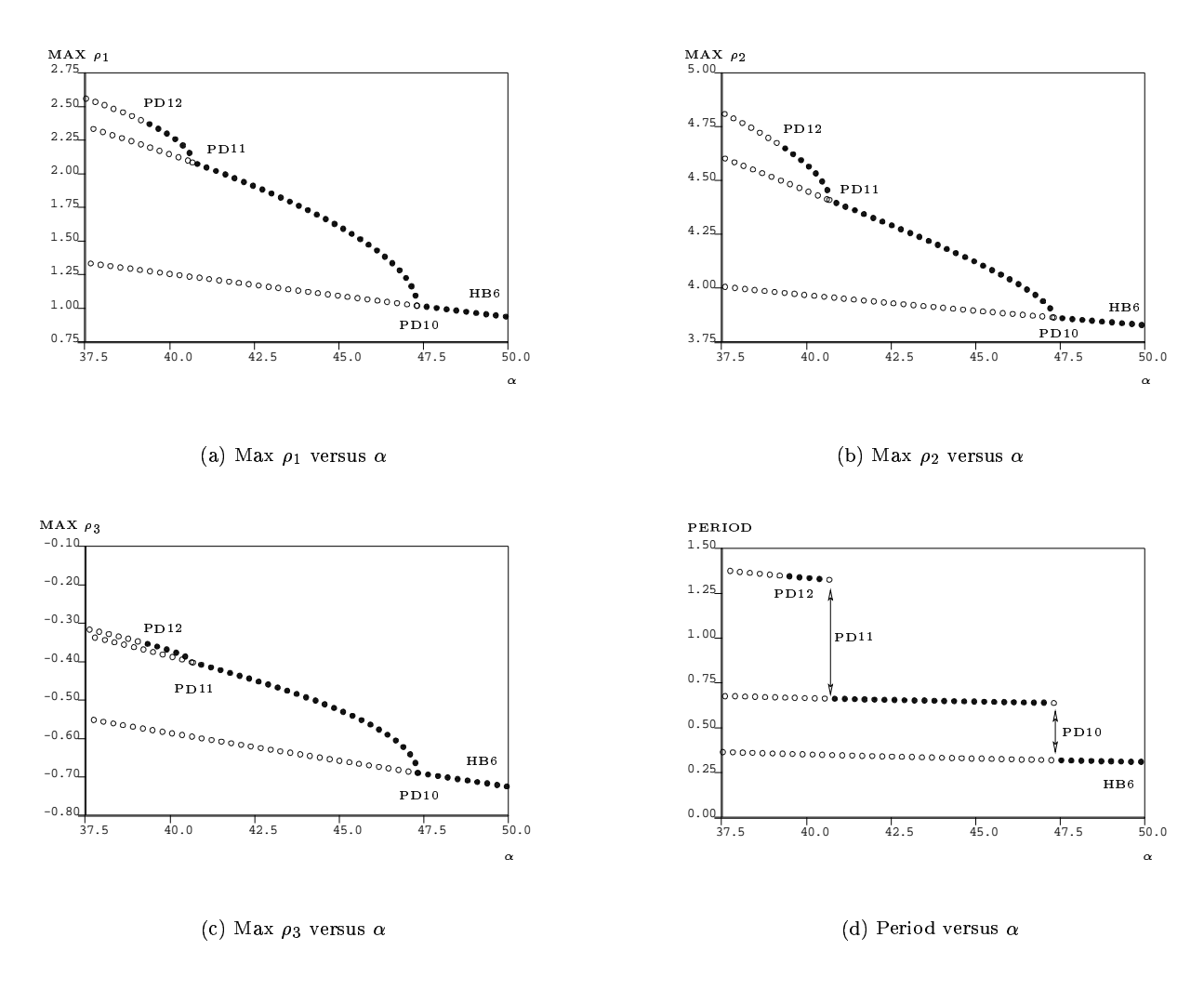


Figure 9: Continuation of limit cycle branch of Maas model from HB6 with c=5

4.3 Dynamics and bifurcation of the Lorenz-84 atmosphere model

We next consider the fast 3-dimensional atmosphere subsystem of our 6-dimensional coupled model described by the differential equation for (X, Y, Z), and freeze the interaction term coming from the slow climate component described by (ρ_1, ρ_2, ρ_3) . As before, the frozen variables appear in the form of a real-valued bifurcation parameter which will now be denoted by $\gamma := aF_0 + k_2\rho_2$. While in the previous subsection a *frozen* fast variable is intuitive only if imagined as an average over the fast motion, here, due to the slowness of the climate variables, freezing them has an intuitively obvious meaning.

We therefore have to consider the following family of differential equations for the atmospheric variables (X, Y, Z):

$$\dot{X} = -Y^2 - Z^2 - aX + \gamma,
\dot{Y} = XY - bXZ - Y + G,
\dot{Z} = bXY + XZ - Z,$$
(4.8)

parametrized by γ . The dynamics of (4.8) has already been studied since the introduction of this atmosphere model by Lorenz [32]. Numerical and analytical investigations can be found for instance in Masoller, Schifino and Romanelli [37] and Sicardi and Masoller [42]. A bifurcation analysis is presented in Shilnikov, Nicolis and Nicolis [41]. These studies were, however, performed in order to explore the rich dynamics of this model. But here, we are only concerned with the parameter γ describing the influence of the ocean and thereby connecting to the calculation of invariant measures (see Subsect. 5.1).

Again we do a detailed bifurcation analysis of the system using AUTO (see Doedel, Champneys, Fairgrieve, Kuznetsov, Sandstede and Wang [7]) to detect bifurcation points and branches in the diagrams while varying the parameter γ continuously in the interval [-20, 40] We choose the parameters in (4.8) in the following way: a = 0.25, b = 4 and G = 1. As in the previous section, in the following diagrams solid curves represent stable steady state branches, dashed curves unstable steady state branches. Full discs stand for stable limit cycle branches, empty discs for unstable ones.

Let us first comment on the steady state parts of the bifurcation diagrams (see Fig. 10). Two saddle-node bifurcations occur at $\gamma = 0.30$ and $\gamma = 1.08$, and the steady state branch splits into three branches according to Fig. 10(a). X being negative, the lower branch stands for stable easterly jets of baroclinic structure, i.e. with phase eventually depending on the atmospheric pressure. The middle branch, bounded by two saddle-node bifurcation points (lab. SN1 and SN2), represents an unstable weak westerly jet which is of baroclinic nature as well. The upper branch shows westerlies as well, is baroclinic in the first part and finally loses the pressure dependence of the phase, i.e. becomes barotropic. This branch is more closely related to the present large scale general atmospheric circulations. As γ increases, it is first stable and then loses stability when γ reaches the value 0.32 (lab. HB3), where the system undergoes a Hopf bifurcation with a stable limit cycle branch emerging on the right hand side. This limit cycle branch (see Fig. 11) represents a baroclinic traveling wave with a period of about 1.50. It is stable until it hits the first period doubling bifurcation point at $\gamma = 1.56$ (lab. PD4), and loses stability there. The emerging unstable branch ends at another period doubling point which is reached at $\gamma = 4.72$ (lab. PD5). Here the limit cycle becomes stable again until a torus bifurcation occurs at $\gamma = 7.34$ (lab. TR6). Beyond this point the limit cycle branch exhibits two saddle-node bifurcations (lab. SN7 and SN8) and finally becomes stable again as it crosses the last saddle-node bifurcation point. Let us now discuss the period doubling branch emerging at PD4 (Fig. 12). It is at first stable until it hits a torus bifurcation point for $\gamma = 1.97$ (lab. TR9), and a period doubling bifurcation point at $\gamma = 2.06$ (lab. PD10). The flow behaves chaotically near $\gamma = 2.00$. It becomes stable again for $\gamma \in (3.84, 4.00)$. The points on the branch corresponding to the boundaries of the interval represent a saddle-node bifurcation (lab. SN12) and a period doubling bifurcation (lab. PD13). The periods of the period doubling branches originating at lab. PD10 and PD13 are given in Fig. 13, respectively.

We next briefly describe the scenarios encountered on the period doubling branch emerging at PD5. Unlike the one previously discussed related to PD4 the instabilities along this branch are caused by further period doubling and saddle-node bifurcations, while no torus bifurcation occurs. More explicitly, its stable parts are interrupted

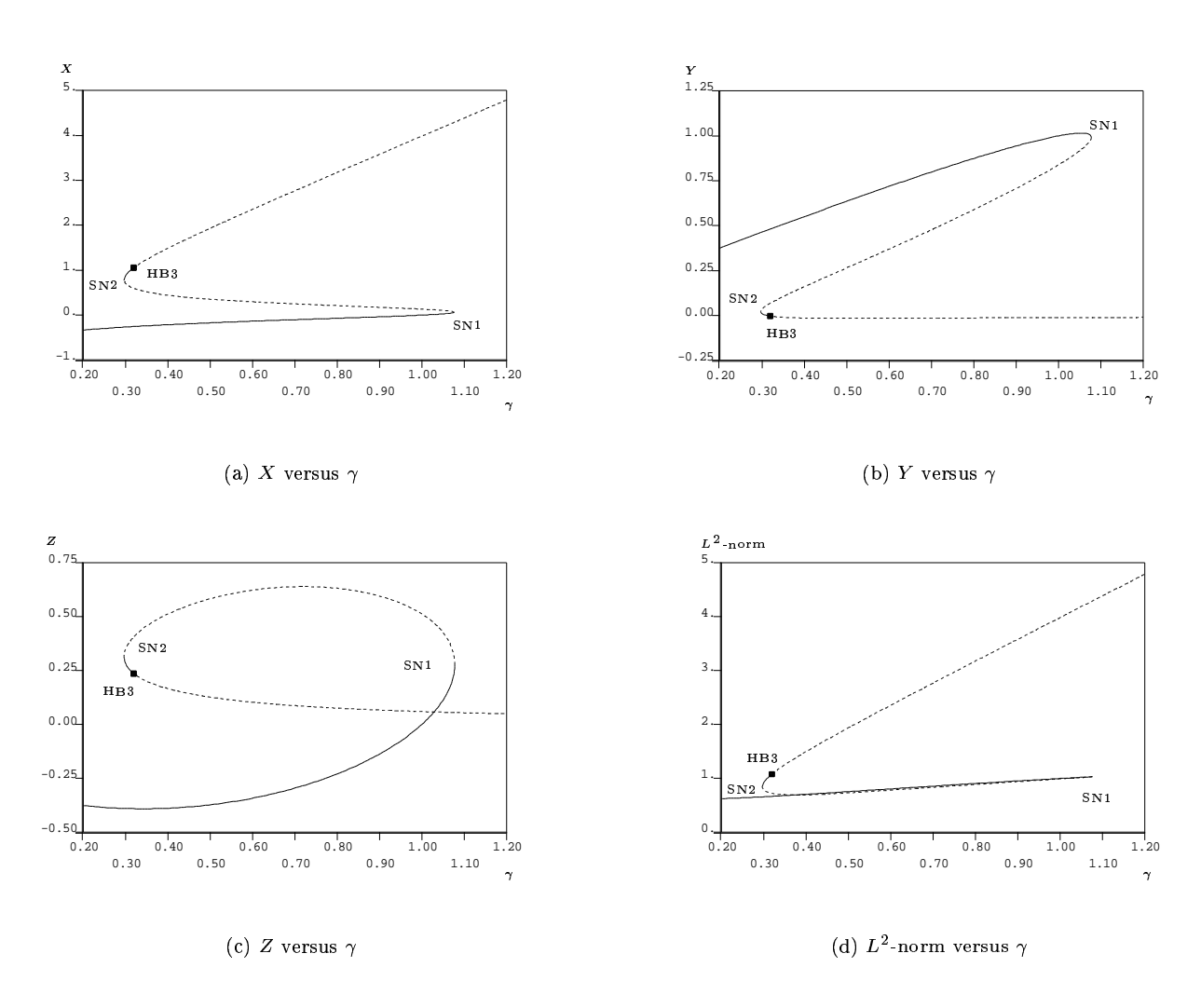


Figure 10: Steady state bifurcation diagram of Lorenz-84 model

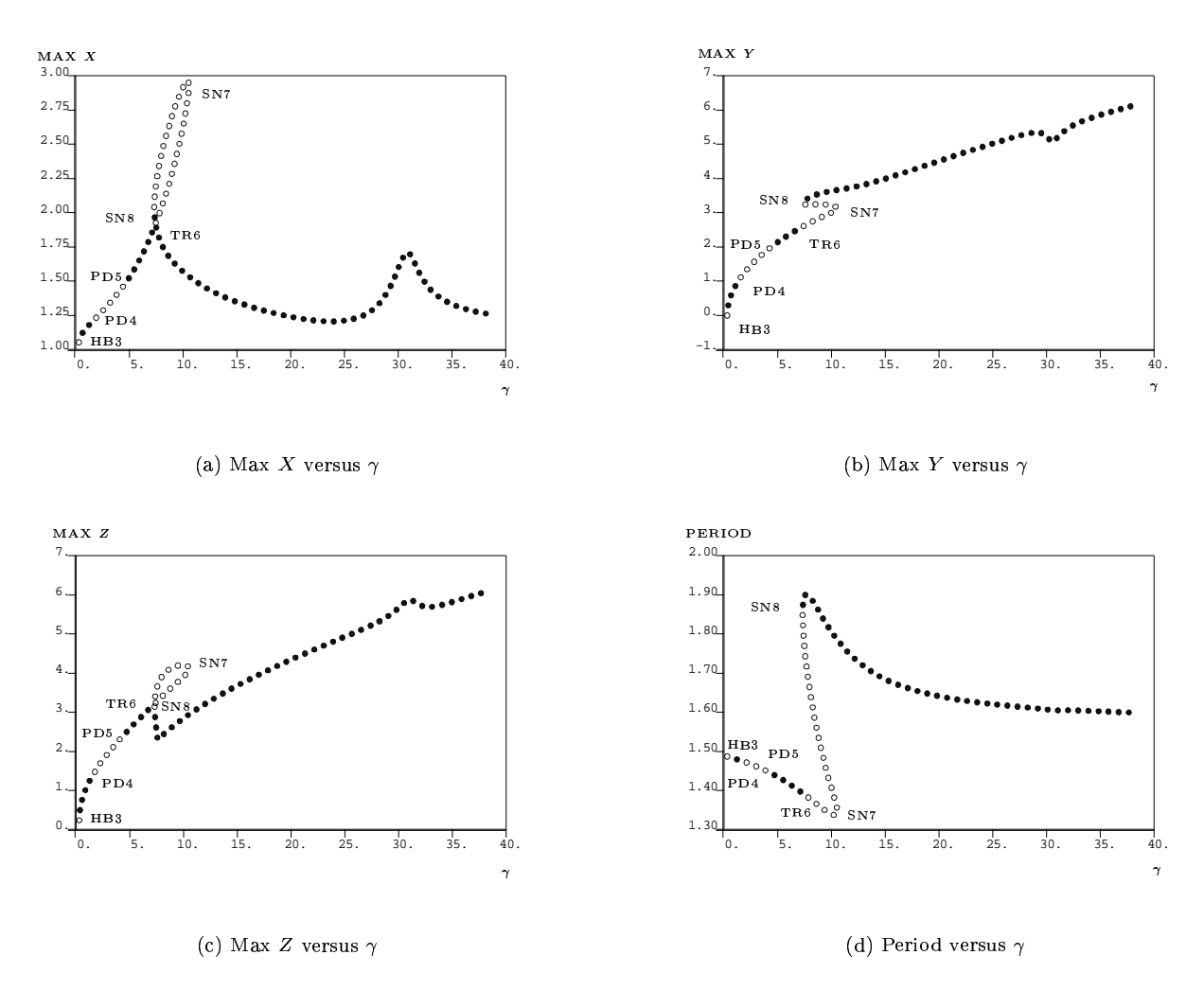


Figure 11: Continuation of limit cycle of Lorenz 84 model from HB3

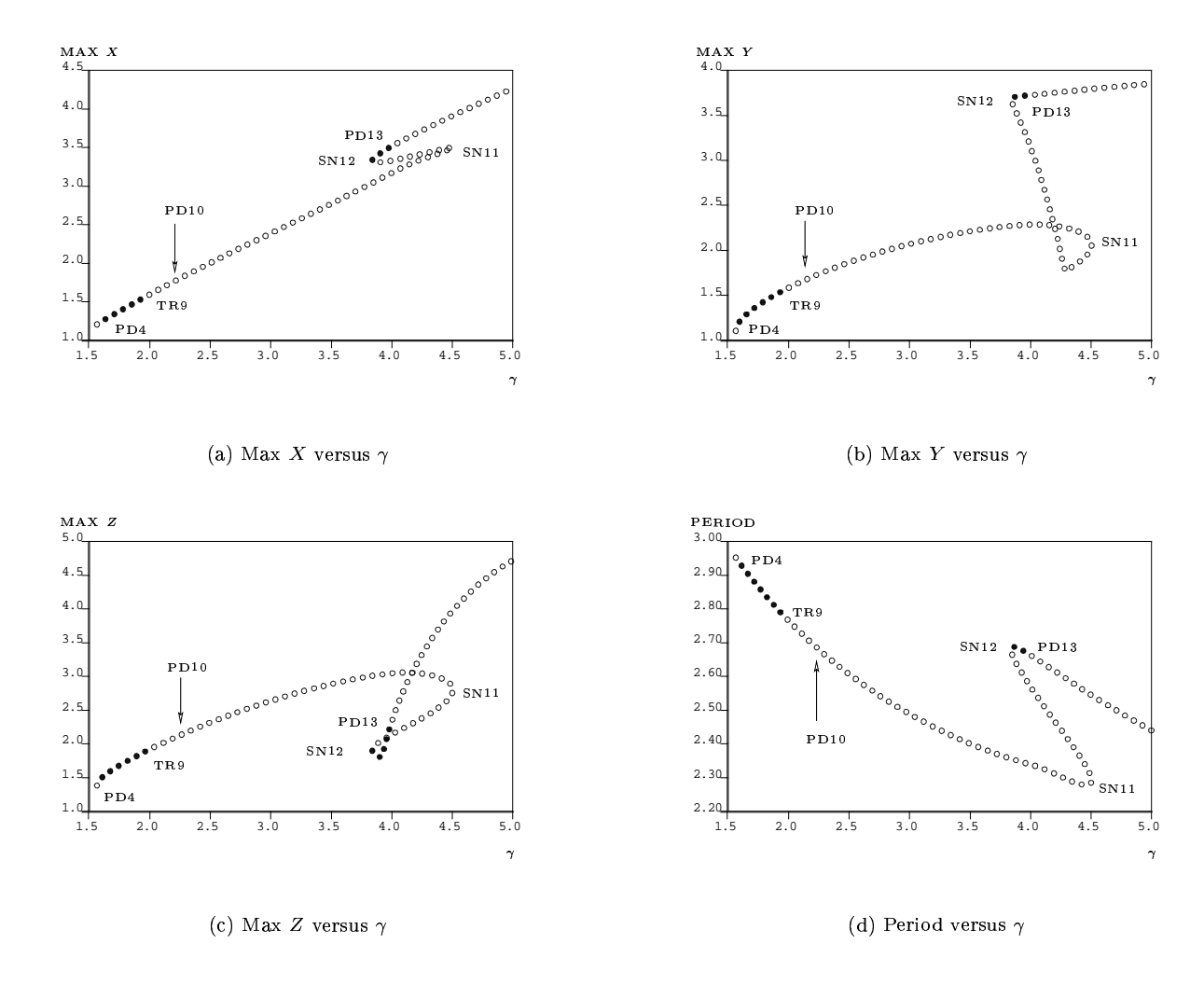


Figure 12: Continuation of limit cycle branch from PD4 of Lorenz-84 model

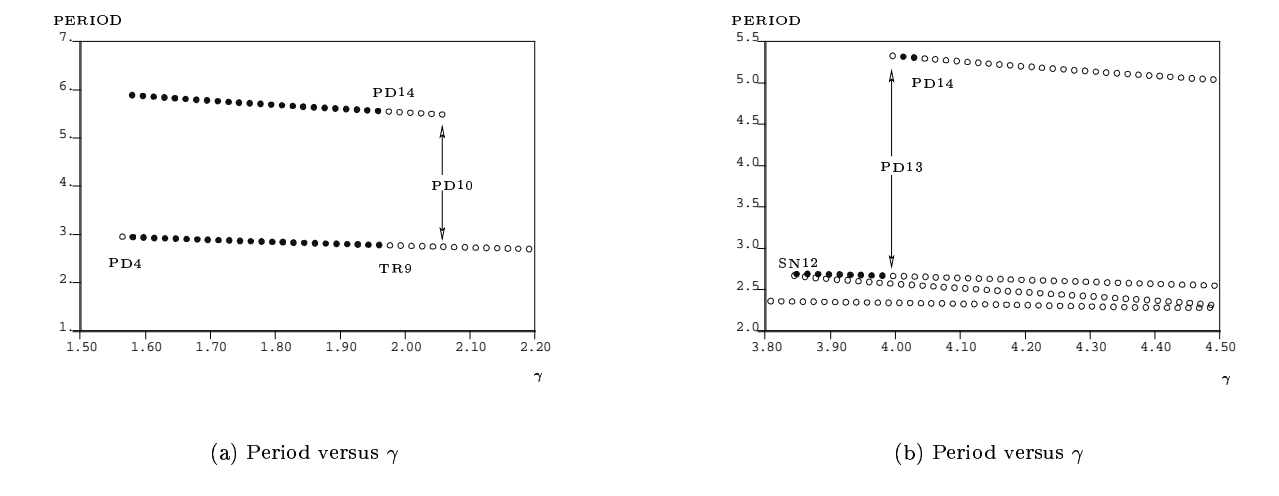


Figure 13: Continuation of limit cycle branch from PD4 and PD10 of Lorenz 84 model

by two period doubling bifurcation points corresponding to $\gamma=3.89$ (lab. PD16) and $\gamma=3.04$ (lab. PD17) and a saddle-node bifurcation point related to $\gamma=2.19$ (lab. SN18). The two period doubling points are connected by a further period doubling branch with a period of about 3.60. Its stability is further interrupted by two period doubling points corresponding to $\gamma=3.40$ (lab. PD19) and $\gamma=3.14$ (lab. PD20) connected by a stable limit cycle branch with a period of about 7.30.

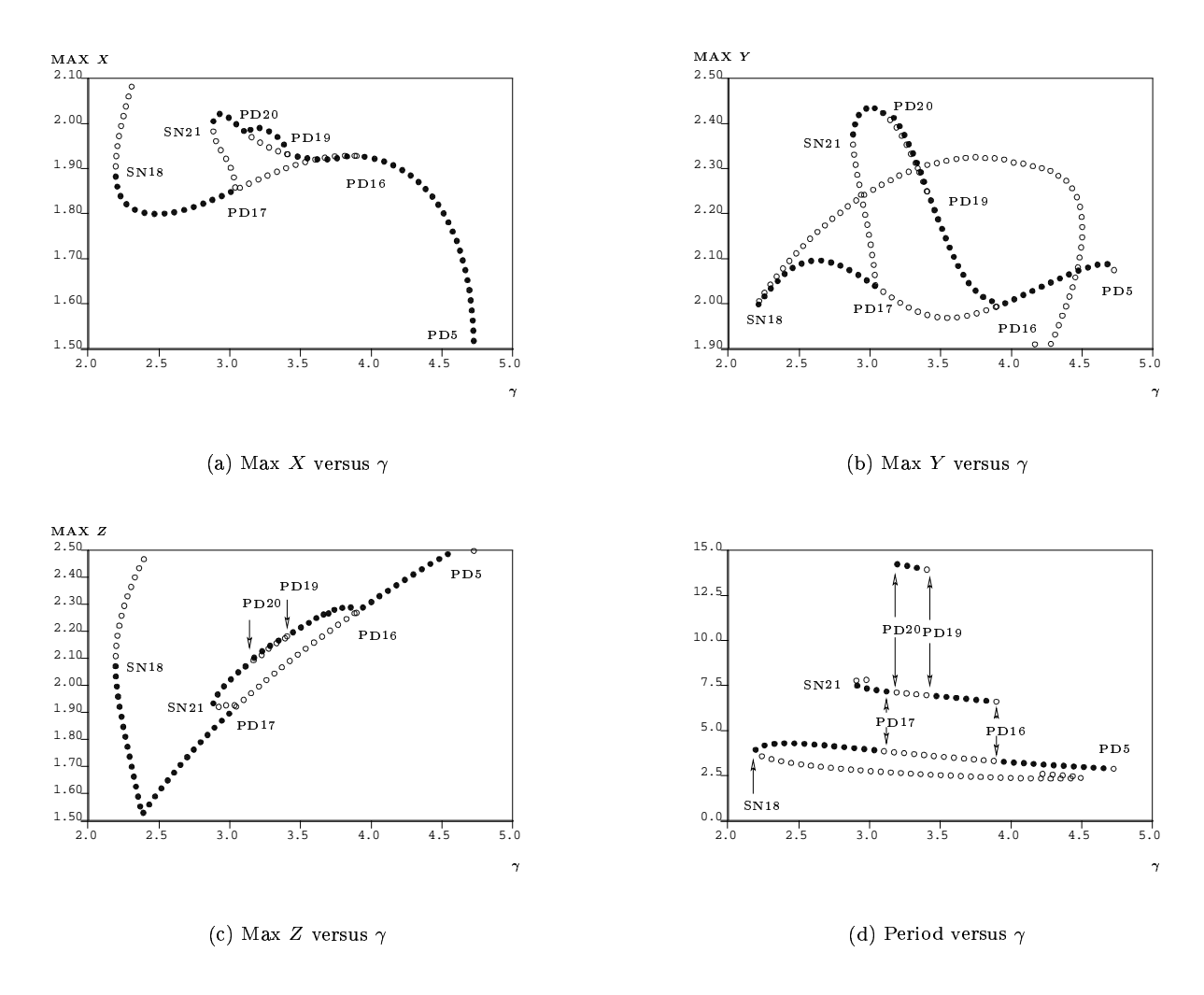


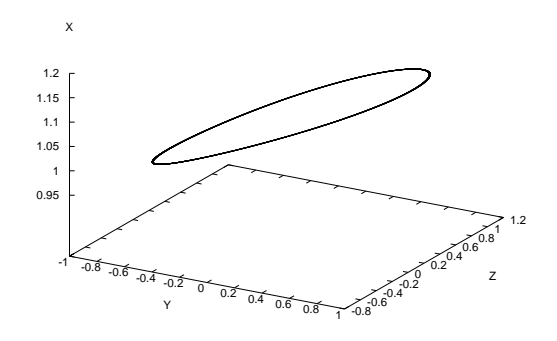
Figure 14: Continuation of limit cycle of Lorenz 84 model from PD5

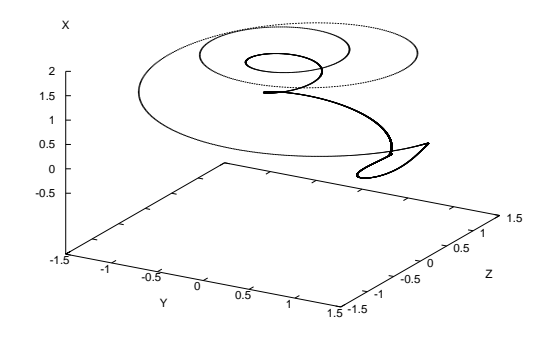
There is another limit cycle branch which coexists with the HB3 branch as γ varies in the interval (1.10, 1.16). This branch, however, is not detected by AUTO. It emerges when integrating the model step by step while increasing γ . Though the life interval for this limit cycle branch is short, the geometric structure of the corresponding trajectories is closer to the well known chaotic orbit for γ close to 2.00. Its characteristic orbit and the orbit of the limit cycle associated with HB3 for the same γ are shown in Fig. 15.

5 Statistical characteristics of the reduced models

We will now describe how and by which algorithms to determine the ingredients of the three reduced models corresponding to our coupled atmosphere-ocean Lorenz-Maas model given by (3.7,3.8) which we repeat for the reader's convenience:

$$\frac{d}{dt} \begin{pmatrix} \rho_1 \\ \rho_2 \\ \rho_3 \end{pmatrix} = f(\rho, X) = \begin{pmatrix} \rho_1 \rho_3 + f \rho_2 \rho_3 - \rho_1 \\ \rho_2 \rho_3 - f \rho_1 \rho_3 - k_3 \rho_2 + R + k_1 X \\ -k_4 (\rho_1^2 + \rho_2^2) - \mu \rho_3 + c \end{pmatrix},$$
(5.1)





- (a) The orbit of the limit cycle branch from HB3
- (b) The orbit of the limit cycle from another branch

Figure 15: Characteristic limit cycles of the Lorenz 84 model at $\gamma = 1.1$

$$\frac{d}{dt} \begin{pmatrix} X \\ Y \\ Z \end{pmatrix} = \frac{1}{\varepsilon} g(\rho_2, X, Y, Z) = \frac{1}{\varepsilon} \begin{pmatrix} -Y^2 - Z^2 - aX + aF_0 + k_2\rho_2 \\ XY - bXZ - Y + G \\ bXY + XZ - Z \end{pmatrix}.$$
(5.2)

5.1 Invariant measures of the Lorenz-84 atmosphere model

According to Subsection 2.2, the most basic operation preceding any reduction method is to determine the invariant measure(s) of the atmosphere subsystem with frozen ocean variables.

To connect with the notations of Subsection 2.2 we have $x=(x_1,x_2,x_3):=(\rho_1,\rho_2,\rho_3)\in\mathbb{R}^3$, $y=(y_1,y_2,y_3):=(X,Y,Z)\in\mathbb{R}^3$. We are looking for the invariant measures $d\mu_{\rho_2}(X,Y,Z)$ of

$$\frac{d}{dt}\begin{pmatrix} X\\ Y\\ Z \end{pmatrix} = g(\rho_2, X, Y, Z) = \begin{pmatrix} -Y^2 - Z^2 - aX + aF_0 + k_2\rho_2\\ XY - bXZ - Y + G\\ bXY + XZ - Z \end{pmatrix},$$
(5.3)

where ρ_2 is frozen.

Note that the invariant measure corresponding to a steady state of (5.3) is the Dirac measure charging this steady state, while for a limit cycle of (5.3) the invariant measure has density $c/\|g(\rho_2, X, Y, Z)\|$ with respect to the length element of the limit cycle, where c is some norming constant. Similarly for quasiperiodic orbits.

It is now of great help that we have already done a detailed bifurcation analysis of (5.3) in Subsection 4.3, using the bifurcation parameter $\gamma := aF_0 + k_2\rho_2$. The bifurcation diagrams tell us that there exist parameter intervals in which we have several coexisting stable structures (steady states, limit cycles, quasiperiodic orbits, chaotic attractors) which all carry invariant measures. We have applied the following two methods for the calculation of the invariant measures of (5.3)

Frobenius-Perron operator method

Let $F: \mathbb{R}^n \to \mathbb{R}^n$ be a diffeomorphism (e.g. the time T mapping of the solution flow of (5.3)). Assigning to each probability measure ν on the Borel sets of \mathbb{R}^n its image $\tilde{F}(\nu) := \nu(F^{-1}(\cdot))$ under F defines the Frobenius-Perron operator of F. Clearly ν is invariant under F if $\tilde{F}(\nu) = \nu$, i.e. if ν is an eigenvector of \tilde{F} with eigenvalue 1.

We can use the software package GAIO to obtain the invariant measure (denoted by IMGAIO) developed by Dellnitz and coauthors [5, 4]. An advantage of this method is that if there exists a global attractor then the influence of all initial values are taken into account. However, if the global attractor is large, we obtain the invariant measure at a low resolution only as the procedure is time-consuming (box counting, solving eigenvalue problem etc.).

We are in the favorite position that we know from Subsect. 4.1 (Theorem and its proof) that for any $\rho_2 \in \mathbb{R}$ (5.3) has a global attractor $A(\rho_2)$ which is contained in the absorbing ball $B := \{ ||(X,Y,Z)|| \le r \}$ not depending on ρ_2 whose radius is given by (4.6). It follows that for all ρ_2 all invariant measures μ_{ρ_2} are also supported by $A(\rho_2)$ and hence by this ball B which gives us an upper bound for the initial box independent of ρ_2 when applying GAIO.

Path following method (forward and backward)

This method is based on the fact that after some transient period the atmosphere subsystem will eventually tend to some specific flow pattern (equilibrium, limit cycle, quasiperiodic orbit, or chaotic flow), and the occupation measure in phase space,

 $\mu_{
ho_2}^T(A) := rac{1}{T} \int_{t=0}^T 1_A(arphi_t^{
ho_2}) \, dt \,,$

measuring the percentage of time of the trajectory $\varphi_t^{\rho_2}(X,Y,Z)$ of (5.3) spent in a set $A \subset \mathbb{R}^3$, will have approached some invariant measure μ_{ρ_2} if observation time T is long enough.

We now first integrate the model (5.3) for 1.0×10^6 time units in order to get rid of transient behavior, and then run it further to decide whether it tends to an equilibrium or a limit cycle. If yes, we are done, and the invariant measure can be easily obtained as explained above. If no, we integrate the model further long enough (for more than 8.0×10^6 units), then calculate the occupation measure and take this as the invariant measure (see Fig. 16 for explanation).

Now the bifurcation diagrams from Subsect. 4.3 are of great help. Since we have to obtain the invariant measures for various values of ρ_2 (resp. γ) we have two choices to start:

We either start from a globally stable steady state such that the corresponding γ value is far from the interesting region and small enough, or start from a periodic orbit such that the corresponding γ value is large enough. We take the occupation measure of the corresponding orbit as the invariant measure.

We now change the parameter γ by increasing or decreasing it and take the end point of the previous integration as the initial value of the new one. We call the method **forward/backward path following method** (and denote the resulting invariant measure by IMF and IMB, resp.) if γ is increased or decreased, resp. (see Fig. 16). The path

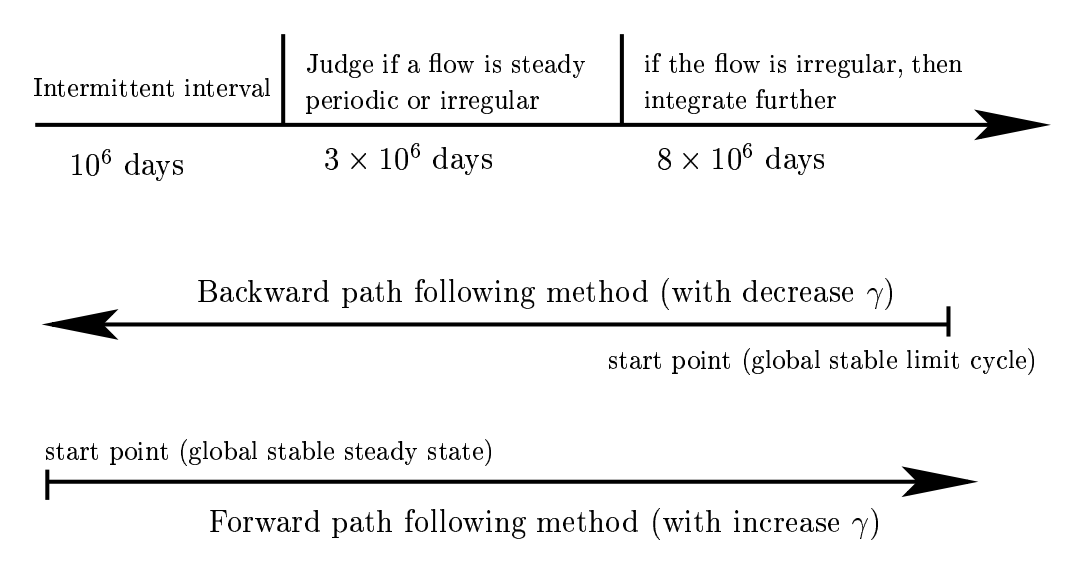


Figure 16: Illustrative diagram of the path following method

following method is rather efficient for dimensions less than 3 if the bifurcation behavior is not too complicated. If, however, several stable flow patterns coexist for certain ranges of γ , this method will single out a particular branch of invariant measures and will not be able to detect the other one's. [connect to the discussion in subsection 7.1]

With the invariant measures of the Lorenz-84 atmosphere model in principle at hand we can now determine the ingredients of the reduced models.

5.2 The drift coefficient of the reduced models

There is only the term X in the second equation of the system (5.1) to be averaged. Once we have chosen a branch μ_{ρ_2} of invariant measures of (5.3) for frozen ρ_2 , we apply (2.24) and obtain, denoting the first component of the solution of (5.3) by $X_f^{\rho_2}$,

$$\bar{X}(\rho_2) := \lim_{T \to \infty} \frac{1}{T} \int_0^T X_t^{\rho_2} dt = \int_{\mathbb{D}^3} X d\mu_{\rho_2}(X, Y, Z). \tag{5.4}$$

Hence the statistical ocean model (A) obtained by averaging on the basis of the branch μ_{ρ_2} of invariant measures is (with $\bar{\rho}$ the generic variable of (A), and with $\bar{f}(\bar{\rho}) := \bar{f}_{\mu_{\bar{\rho}_2}}(\bar{\rho})$)

$$\dot{\bar{\rho}} = \frac{d}{dt} \begin{pmatrix} \bar{\rho}_1 \\ \bar{\rho}_2 \\ \bar{\rho}_3 \end{pmatrix} = \bar{f}(\bar{\rho}) = \begin{pmatrix} \bar{\rho}_1 \bar{\rho}_3 + f \bar{\rho}_2 \bar{\rho}_3 - \bar{\rho}_1 \\ \bar{\rho}_2 \bar{\rho}_3 - f \bar{\rho}_1 \bar{\rho}_3 - k_3 \bar{\rho}_2 + R + k_1 \bar{X}(\bar{\rho}_2) \\ -k_4 (\bar{\rho}_1^2 + \bar{\rho}_2^2) - \mu \bar{\rho}_3 + c \end{pmatrix}.$$
(5.5)

The averaged function $\bar{X}(\bar{\rho}_2)$ is obtained numerically as a function of $\bar{\rho}_2$, in fact as a function of $\gamma := aF_0 + k_2\bar{\rho}_2$ for the interval $-39 \le \gamma \le 41$.

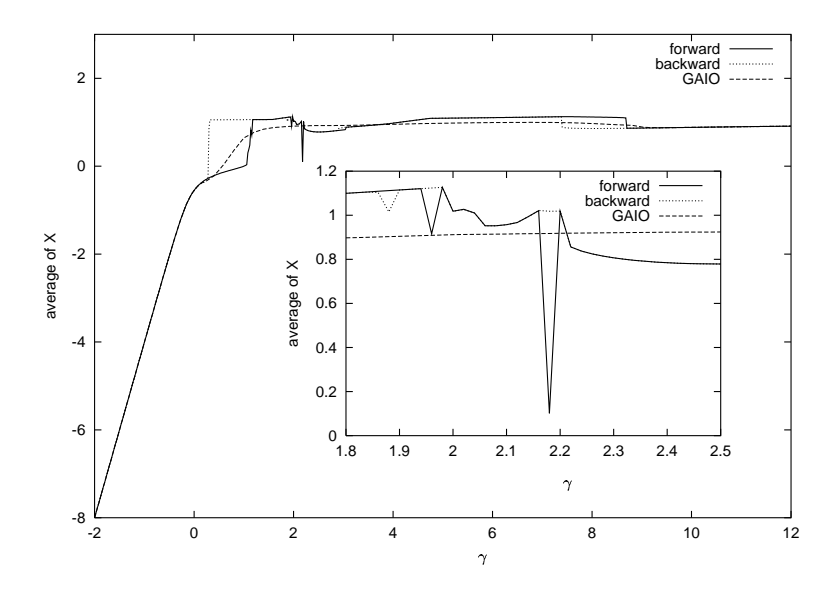


Figure 17: The averaged X versus $\gamma = aF_0 + k_2\rho_2$ of the Lorenz-84 model

Fig. 17 shows \bar{X} versus γ with respect to the invariant measures obtained by IMF, IMB and IMGAIO. The discrepancy of the results of IMF and IMB in parameter ranges where several stable states (equilibria and limit cycles) coexist (causing hysteresis) is clearly visible.

For example, the first splitting between IMF and IMB near $\gamma=0.30$ is due to the saddle-node bifurcation of the steady state. \bar{X} obtained by IMF (the lower branch) corresponds to the lower stable steady state branch (see Fig. 10(a)), while \bar{X} obtained by IMB is first connected with the upper stable steady state branch and then jumps to the stable limit cycle branch originating from the first Hopf bifurcation HB3. This can be seen more clearly in Fig. 18(a).

We present two more cases for which IMF and IMB differ in Fig. 18(b): These discrepancies are caused by the saddle-node bifurcations at $\gamma = 2.88$ (lab. SN21 of PD5) and at $\gamma = 7.33$ (lab. SN8 of HB3). In the left panel of Fig. 18(b) the forward branch is related to PD5 while the backward branch is related to the period-doubling branch of PD5. In the right panel of Fig. 18(b) the forward branch is related to the torus bifurcation branch (lab. TR6 of Fig. 11) while the backward branch is related to HB3 after the saddle-node bifurcation point (lab. SN8 of Fig. 11). This is related to the hysteresis phenomenon due to the coexistence of several stable equilibria (see Fig. 19).

We also observe that \bar{X} obtained by IMGAIO lies between the values obtained by IMF and IMB in case the latter are different. This suggests that in those cases IMGAIO yields a weighted average of IMF and IMB,

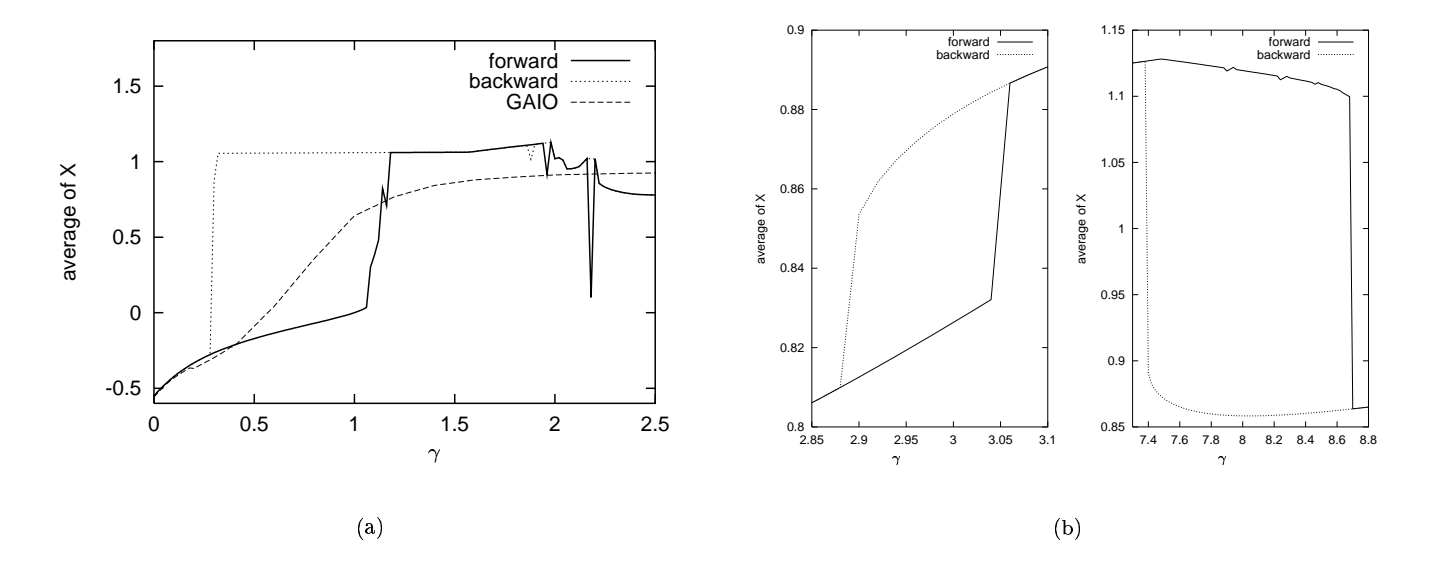


Figure 18: The amplified picture of the averaged X versus $\gamma = aF_0 + k_2\rho_2$ of the Lorenz-84 model

reflecting a more global picture of the dynamical system in phase space.

Note that the Jacobian of \bar{f} needed for the model (L) also depends on the branch of invariant measures used for the calculation of \bar{f} .

5.3 The diffusion coefficient of the reduced models

The general 3×3 nonnegative-definite diffusion matrix $\sigma(\rho)$ (see formula (2.13)) needed for the stochastic models (L) and (N) is given by

$$\sigma(\rho)^2 := \lim_{T \to \infty} \frac{1}{T} \int_0^T \int_0^T R_{\rho}(t-s)dtds, \tag{5.6}$$

where $R_{\rho}(t)$ is the covariance matrix

$$R_{\rho}(t) := \operatorname{cov}(f(\rho, \varphi_t^{\rho}), f(\rho, \varphi_0^{\rho})) = \mathbb{E}(f(\rho, \varphi_t^{\rho}) - \bar{f}(\rho))(f(\rho, \varphi_0^{\rho}) - \bar{f}(\rho))'$$
(5.7)

of $\eta_t^{\rho} := f(\rho, \varphi_t^{\rho})$ for frozen ρ . The expectation is with respect to the joint distribution of φ_t^{ρ} and $\varphi_0^{\rho} = (X_0, Y_0, Z_0)$, where (X_0, Y_0, Z_0) has distribution μ_{ρ} .

Due to the structure of f in (5.1), only the (2,2) entry of $R_{\rho}(t)$ and hence of $\sigma(\rho)$ is nontrivial (which we continue to denote by the same symbols). Moreover, due to the structure of (5.2), these quantities only depend on ρ_2 . Thus

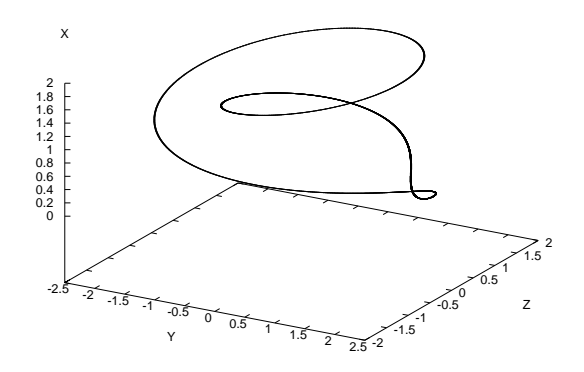
$$\sigma(\rho_2)^2 = k_1^2 C(\rho_2)^2, \quad C(\rho_2)^2 := \lim_{T \to \infty} \frac{1}{T} \int_0^T \int_0^T \text{cov}(X_t^{\rho_2}, X_s^{\rho_2}) dt ds.$$
 (5.8)

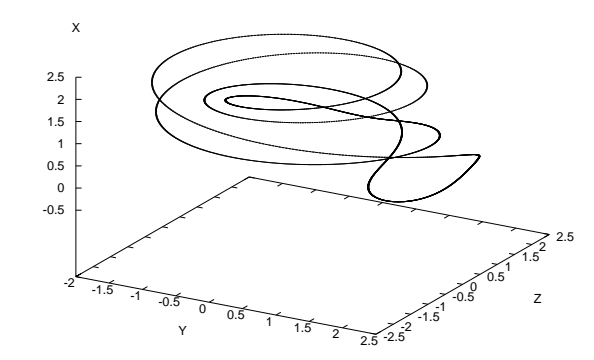
Here $X_t^{\rho_2}$ is the first component of the solution of (5.3) with frozen ρ_2 and random initial conditions with distribution $d\mu_{\rho_2}(X,Y,Z)$.

We can rewrite the limit in (5.8) for numerical convenience as

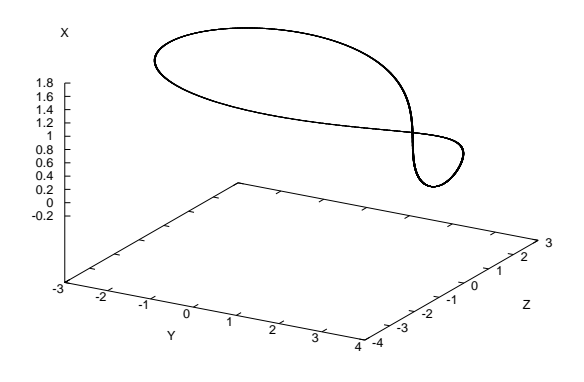
$$C(\rho_2)^2 = \lim_{T \to \infty} K(T), \quad K(T) = \frac{2}{T} \int_0^T (T - t) \operatorname{cov}(X_t^{\rho_2}, X_0^{\rho_2}) dt.$$
 (5.9)

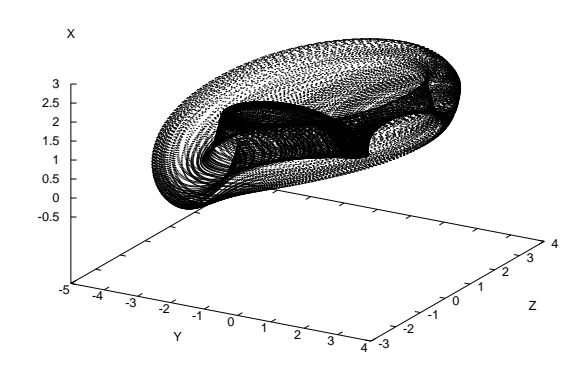
Having done the calculation (5.8) we are in a position of writing down the stochastic models (L) and (N) for the ocean component of the coupled Lorenz-Maas atmosphere-ocean model.





- (a) The orbit from the PD7 at $\gamma=3.00$
- (b) The orbit from the period doubling branch of PD7 at $\gamma=3.00\,$





- (c) The orbit from the HB3 at $\gamma=8.60$
- (d) The orbit from the torus bifurcation branch at $\gamma=8.60$

Figure 19: Some characteristic orbits of the Lorenz 84 Model

For the linear diffusion approximation (L) we first solve the averaged equation (A) given by (5.4) with initial value $\bar{\rho}_0 = \rho$ obtaining $\bar{\rho}(t)$. Then we plug this into the linear SDE

$$d\zeta_t^{\rho} = D\bar{f}(\bar{\rho}(t))dt + \begin{pmatrix} 0 \\ k_1 C(\bar{\rho}_2(t))dW_t \\ 0 \end{pmatrix}, \quad \zeta_0^{\rho} = 0,$$
 (5.10)

where $D\bar{f}$ is the Jacobian of \bar{f} given by (5.5) and W_t is a scalar standard Wiener process. We compose (L) as

$$\zeta^{\varepsilon,\rho}(t) := \bar{\rho}(t) + \sqrt{\varepsilon}\zeta_t^{\rho}. \tag{5.11}$$

The nonlinear diffusion approximation (Hasselmann's equation) (N) is given by the nonlinear SDE

$$dz^{\varepsilon}(t) = \bar{f}(z^{\varepsilon}(t))dt + \sqrt{\varepsilon} \begin{pmatrix} 0 \\ k_1 C(z_2^{\varepsilon}(t))dW_t \\ 0 \end{pmatrix}, \quad z^{\varepsilon}(0) = \rho.$$
 (5.12)

If the invariant reference measure μ_{ρ_2} is the Dirac measure at a steady state of (5.3) then $\operatorname{cov}(X_t^{\rho_2}, X_0^{\rho_2}) \equiv 0$ and hence $C(\rho_2) = 0$. We will now prove that $C(\rho_2) = 0$ also in the case where μ_{ρ_2} is the invariant measure on a limit cycle of (5.3).

Excursion: Vanishing of the diffusion coefficient in the periodic case

Let y(t) be a periodic solution of the ODE $\dot{y}=g(y)$ in \mathbb{R}^m with minimal period p>0 and initial condition $y(0)=y_0$. Then for any $\omega\in[0,p), z(t):=y(t+\omega)$ is a p-periodic solution of $\dot{y}=g(y)$ starting at $z(0)=y(\omega)$ and describing the same limit cycle $\mathfrak{C}\subset\mathbb{R}^m$ in phase space.

The dynamical system over which the p-periodic solution is a strict sense stationary stochastic process is as follows: The probability space is $\Omega := [0, p)$ with addition modulo p, \mathcal{B} the sigma-algebra of Borel sets on Ω , \mathbb{P} the uniform distribution (normalized Lebesgue measure) on \mathcal{B} . Define the family of measure-preserving transformations $\theta_t \omega := \omega + t$ modulo p. Then $(\Omega, \mathcal{B}, \mathbb{P}, (\theta_t)_{t \in \mathbb{R}})$ is a metric dynamical system which is uniquely ergodic (but not weak mixing).

Then $\xi_t(\omega) := y(t+\omega) = y(\theta_t\omega)$ is an ergodic stationary stochastic process taking values on the limit cycle \mathbb{C} . The measure μ on \mathbb{C} invariant under the flow generated by $\dot{y} = g(y)$ is the image of \mathbb{P} under the mapping $\omega \mapsto y(\omega)$. The measure μ has the density $c/\|g(y)\|$ with respect to λ , the Lebesgue measure on \mathbb{C} , but we do not make use of this information.

First note that

$$\mathbb{E}\,\xi_t = \frac{1}{p} \int_{\omega=0}^p \xi_t(\omega) d\omega = \frac{1}{p} \int_0^p y(u) du =: \bar{y} \in \mathbb{R}^m.$$

Since we can switch to $\xi_t - \bar{y}$ we can assume without loss of generality that $\mathbb{E}\xi_t \equiv 0$. We now calculate $X_T(\omega) := \int_0^T \xi_t(\omega) dt$. For given T > 0, $[T/p] \in \mathbb{Z}^+$ is that integer for which $T_p := [T/p]p \leq T < T_p + p$. Then $X_{T_p}(\omega) = 0$, hence

$$X_T(\omega) = \int_{T_p}^T y(t+\omega) dt = \int_{\omega}^{T-T_p+\omega} y(u) du.$$

In particular, $X_T(\omega)$ is p-periodic and

$$||X_T(\omega)|| \le p \max_{0 \le t \le p} ||y(t)|| = c$$
 for all T, ω .

The covariance of ξ_t is

$$R(t) = \mathbb{E}\xi_t \xi_0' = \frac{1}{p} \int_{\omega=0}^p y(t+\omega)y'(\omega)d\omega.$$

We easily see that $R(t+p)=R(t),\ R(t)=R(t-t_p),\ \text{where}\ t_p=[t/p]p,\ \text{and}\ \|R(t)\|\leq c^2.$ An elementary manipulation yields

$$Z_T := \mathbb{E} X_T X_T' = \int_0^T \int_0^T R(t-s) dt ds = \int_0^{T-T_p} \int_0^{T-T_p} R(t-s) dt ds,$$

from which we conclude that $||Z_T|| \leq p^2 c^2$, whence $\frac{1}{T} ||Z_T|| \leq \frac{1}{T} p^2 c^2 \to 0$ as $T \to \infty$. Finally

$$\sigma^2 := \lim_{T \to \infty} \frac{1}{T} \int_0^T \int_0^T R(t-s) dt ds = 0.$$

We apply this to the situation

$$\dot{x} = f(x, y), \quad \dot{y} = \frac{1}{\varepsilon}g(x, y)$$

and assume that $y^x(t)$ is a p(x)-periodic solution of $\dot{y} = g(x,y)$ for frozen x. Then

$$\sigma(x)^2 = V\left(\frac{1}{\sqrt{T}}\int_0^T f(x, y^x(t+\omega(x)))dt\right),$$

where $\omega(x)$ is uniformly distributed on $\Omega(x) = [0, p(x))$. Using $||f(x, y) - \bar{f}(x)|| \le c(x)$ on the limit cycle $\mathfrak{C}(x)$, we obtain

$$\|\sigma(x)^2\| \le \frac{1}{T}c(x)^2 \to 0 \text{ as } T \to \infty,$$

hence $\sigma(x) = 0$ for all x.

The result of this brief excursion is that in our case $\sigma(\rho_2) = 0$ whenever the underlying invariant measure $d\mu_{\rho_2}(X, Y, Z)$ of (5.3) used for averaging sits on a steady state or a limit cycle. The fact that $\sigma(\rho_2) = 0$ also holds for a quasiperiodic solution of (5.3) is supported by our simulations, although we cannot rigorously prove it (the main problem is that the integral over a quasiperiodic function even with mean 0 is not necessarily quasiperiodic – for this to hold one needs diophantine conditions on the frequency vector involved, see Moser and Siegel [43, page 261]).

As a result, only in case of chaotic behavior of (5.3) for some range of values of ρ_2 can we hope that stochasticity in (L) and (N) is "switched on" – if we only consider "simple" invariant measures, (L) and (N) are deterministic and are identical with (A).

In our model the interesting γ intervals for which we have chaotic behavior, hence the diffusion coefficient σ does not vanish are (1.98, 2.04) and (2.10, 2.20). For the representative case $\gamma = 2$, see Fig. ??.

6 Bifurcation analysis of the statistical ocean model

We have studied the bifurcation behavior of the Maas ocean model (4.7) in Subsect. 4.2 which we can now compare with that of the statistical ocean model(s) (A) given by (5.5) obtained by averaging. We calculate \bar{X} for $F_0 = 4$ and $k_2 = 1$ and, to be definite, restrict ourselves to the invariant measures obtained by IMGAIO.

We first put c = 1, $k_1 = 8$ and choose R as bifurcation parameter. Fig. 21 shows the bifurcation diagram of the steady states of (A). Comparing with that of the Maas ocean model (see Fig. 3) we observe that the left-hand part of the bifurcation diagram of (A) is different from that of the Maas model. This is caused by the breakdown of the symmetry property of the Maas model if the parameter is replaced by the function $\bar{X}(\rho_2)$.

However, the right-hand parts of the diagram of (A) (starting from lab. SN3) and of the Maas model (start from lab. SN4) closely resemble each other. The reason is that the function $\bar{X}(\rho_2)$ changes very little for $\rho_2 \geq 0.1$. Fig. 20(c) clearly shows that $\rho_2 \geq 0.1$ after R crosses lab. SN3.

There are, however, also differences between the two diagrams even on their right-hand part. In contrast to those of the Maas model, the steady states of (A) lying between the two saddle-node bifurcation points lab. SN3 and SN4 are no longer stable and are followed by a new Hopf bifurcation (lab. HB5). This reflects some more unstable features of (A).

Corresponding to lab. HB7 of the Maas model, we also do for (A) the continuation of the periodic solution from the Hopf bifurcation point HB7 (Fig. 21). In contrast to the continuation of limit cycles from lab. HB7 in the Maas model we observe for (A) a series of period-doubling bifurcations along this branch. The continuation of the period-doubling branch from lab. PD8 is decreasing with R and joined with lab. HB7. This means that there coexist two stable limit cycles between lab. HB7 and lab. PD8. This period-doubling branch of (A) is quite

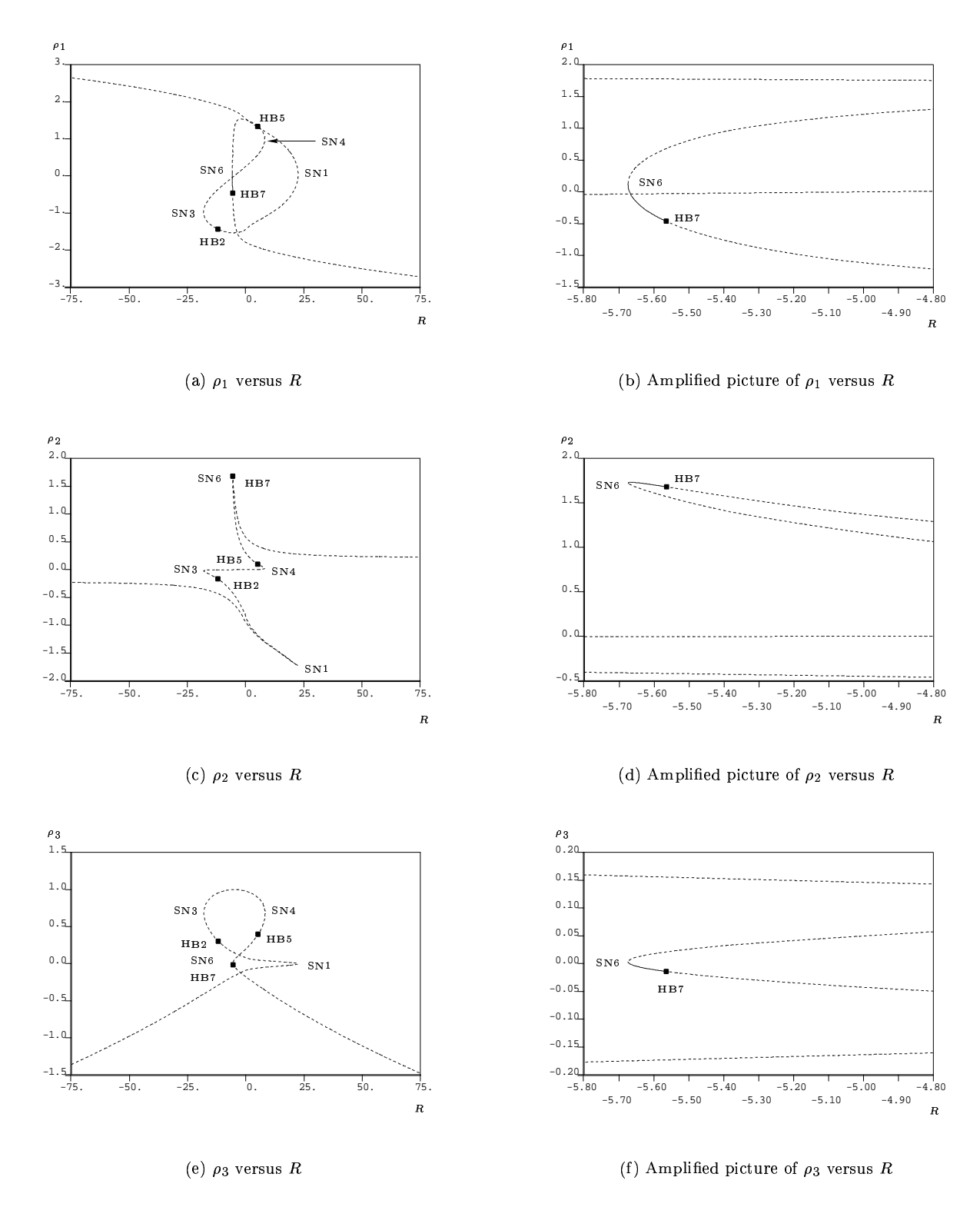


Figure 20: Bifurcation diagram of the steady states of (A) with $c=1,\,k_1=8$

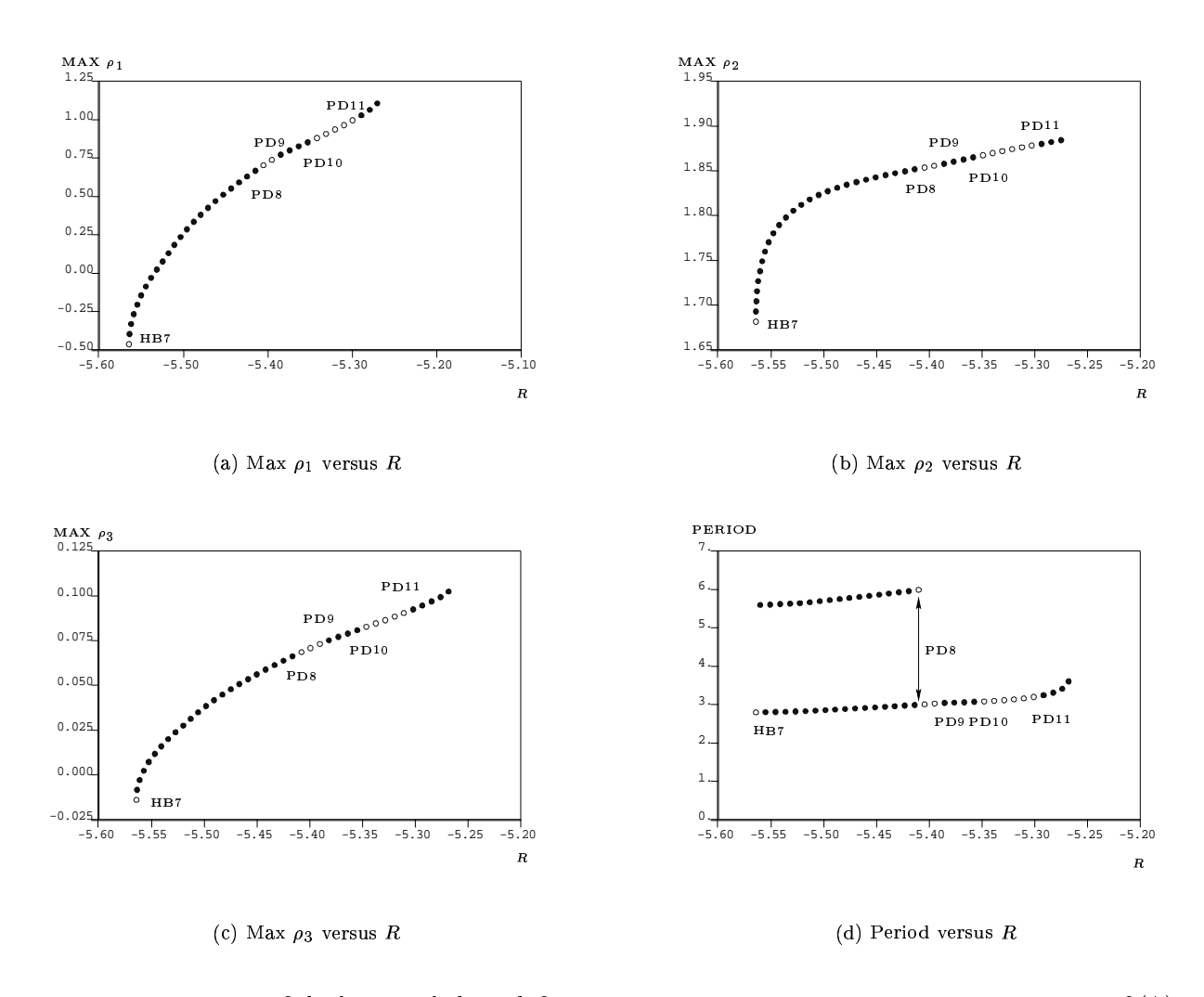


Figure 21: Continuation of the limit cycle branch from HB7 and the period doubling branch from PD8 of (A) with c=1 and k1=8

different from that of the Maas model from HB7 where the period-doubling branch joins the two period-doubling points PD9 and PD10.

We finally investigate the bifurcation behavior of (A) keeping R fixed and using k_1 as bifurcation parameter. This parameter indicates the strength of the influence of the atmosphere to the ocean.

The right-hand side of the bifurcation diagram of the steady states of (A) (Fig. 22) still resembles that of the Maas model. But in contrast to (A) and the Maas model with R as bifurcation parameter, there is now a Hopf bifurcation (lab. HB12). The continuation of the limit cycle branch shows that it is stable until it meets a torus bifurcation point (lab. TR17 of Fig. 23). The Hopf bifurcation point lab. HB16 of (A) is similar to that of lab. HB7 of the Maas model. The continuation of it first undergoes two period-doubling bifurcations which are followed by a torus bifurcation. The latter is not observed in the Maas model.

The presentation of these sample results should suffice, and we stop here. The total picture, also taking into account the various other choices of the invariant measure, is extremely complex.

7 Comparison of the unreduced model with the three reduced models

We now approach the main subject of this study, a numerical comparison of the performance of the three reduced models: the deterministic statistical climate model (A) originating in averaging, and the two stochastic ones, the linear diffusion approximation (L), and finally the nonlinear diffusion approximation (N). Their predictions will be compared to simulations of the unreduced model in different parameter regimes to be specified below.

7.1 The basics of our simulations

First, some comments are in order as to which *numerical schemes* we use for the different models, which numerical methods will produce the *invariant measures* needed for both averaging and calculating the diffusion coefficient in the stochastic models, and finally how we measure numerically the *closeness of trajectories* of the different models.

The following numerical schemes will be used. For the simulations of the unreduced Lorenz-Maas model and for (A), the modified 4th order Runge-Kutta scheme is employed. The time grid is chosen to be $dt = 5.0 \times 10^{-4}$ for the Lorenz-Maas model and $dt = 5.0 \times 10^{-6}$ for (A). In the simulation of the stochastic climate models, we use the further modified 4th order Runge-Kutta scheme with time grid varying between $dt = 5.0 \times 10^{-6}$ and $dt = 5.0 \times 10^{-8}$. The meaning of the time grid for the Lorenz-Maas model is quite different from that of (A), (L) and (N). While for the former it determines time steps in the scale of the atmosphere, for (A), (L) and (N) it gives time units in ocean scales. In the following simulations we call the time unit for the integration of the Lorenz-Maas model "weather day" (abbreviated in figure captions as WD).

Finally, a word of care is in order. Stability and convergence of the modified 4th order Runge-Kutta scheme are not proved for the setting of our stochastic climate models. It should generally be used with care for stochastic differential equations (Kloeden and Platen [29], Kloeden, Platen and Schurz [30]).

To rule out doubts about the validity of this scheme in our setting, we also employ mixed schemes of the following type to check our results: in case the diffusion coefficient $\sigma(\rho_2) = 0$, we use the modified 4th order Runge-Kutta scheme, while we employ either the Euler, the modified Euler or the strong Platen schemes of order one if $\sigma(\rho_2) \neq 0$. The results obtained by these modified schemes correspond well to those the modified 4th order Runge-Kutta scheme yields. This is exemplified by Fig. 25 in the case of the fully coupled atmosphere and ocean. In the sequel we will use the modified 4th-order Runge-Kutta scheme for both (L) and (N) if not specified otherwise.

In the simulations for both the statistical climate models and the stochastic climate models, invariant measures will be computed using the software package GAIO as well as a combination of the forward (IMF) and backward (IMB) path following methods which we will denote by IMF&B. When both IMF and IMB are the same we will call it IMPF. To explain this combination, recall the results of our bifurcation studies for the atmosphere subsystem parametrized by a slowly varying ocean component γ representing essentially ρ_2 . As long as γ is kept outside of bifurcation intervals, the invariant measure obtained by IMF is the same as that obtained by IMB.

There are, however, intervals on the γ -line which we shall call hysteresis intervals in which the invariant measures provided by IMF when entering the interval at its lower boundary disagree with the invariant measures obtained by

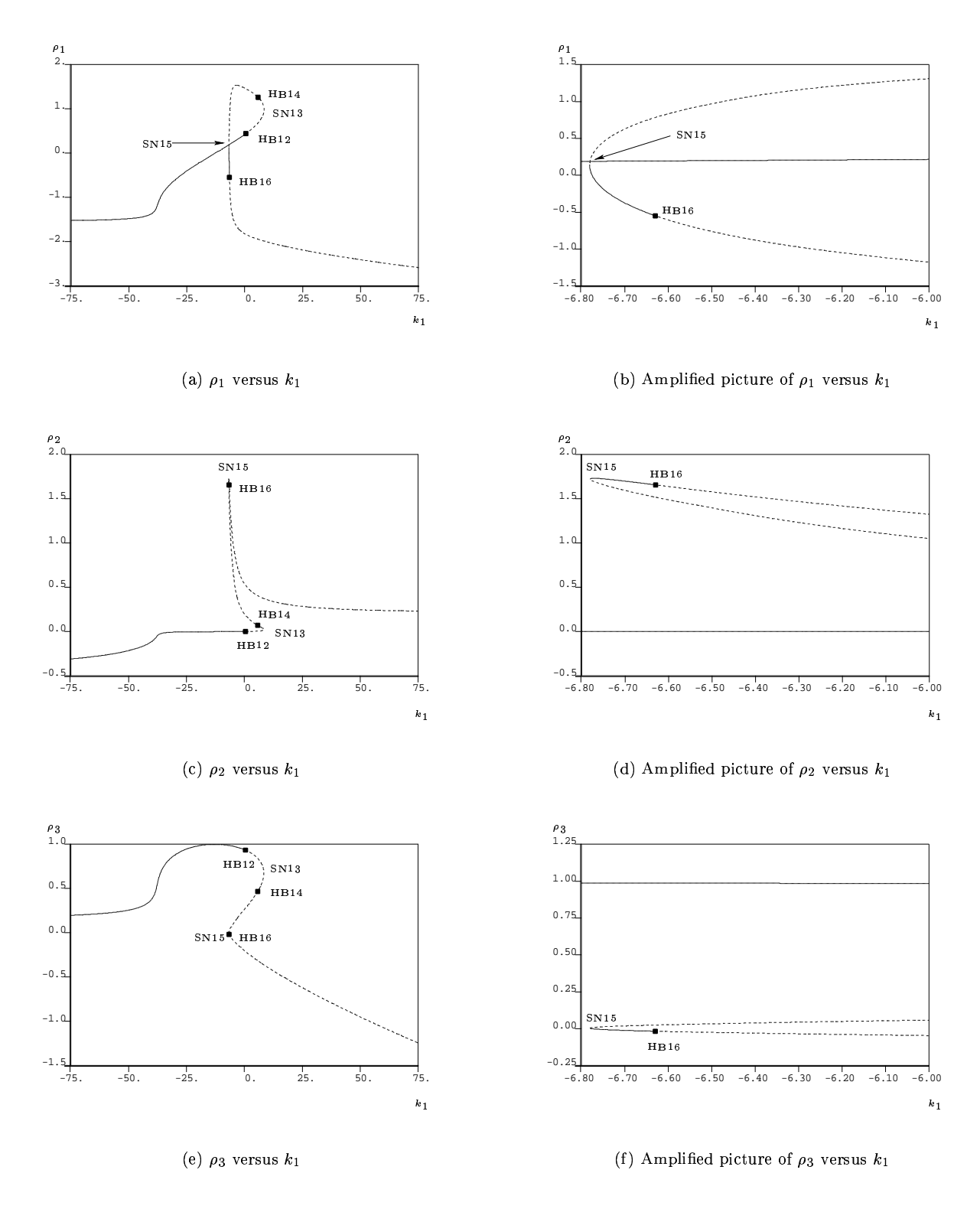


Figure 22: Bifurcation diagram of the steady states of (A) with $c=1,\,R=8$

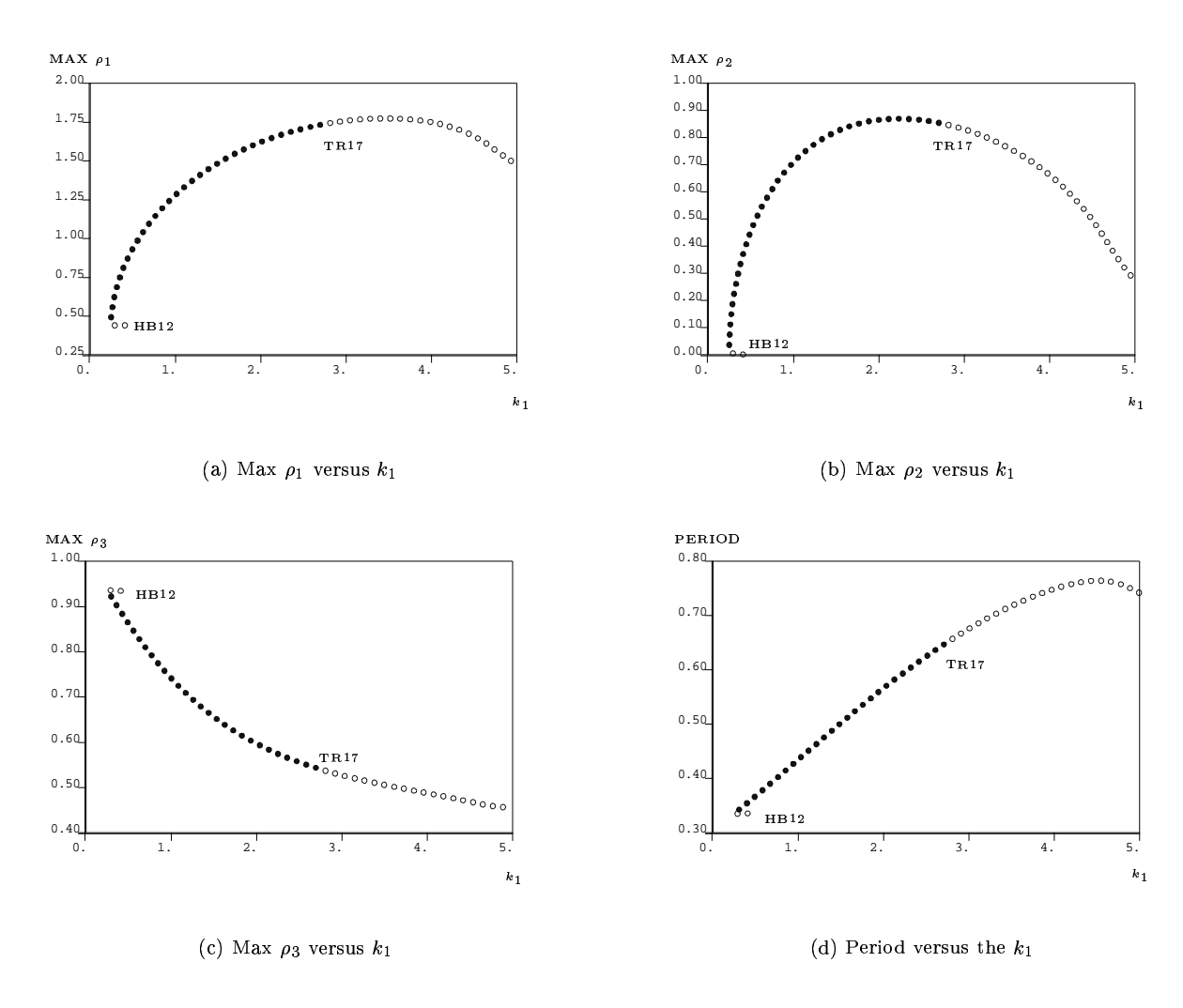


Figure 23: Continuation of the limit cycle branch of (A) from the first Hopf bifurcation point HB12 with c=1, R=8

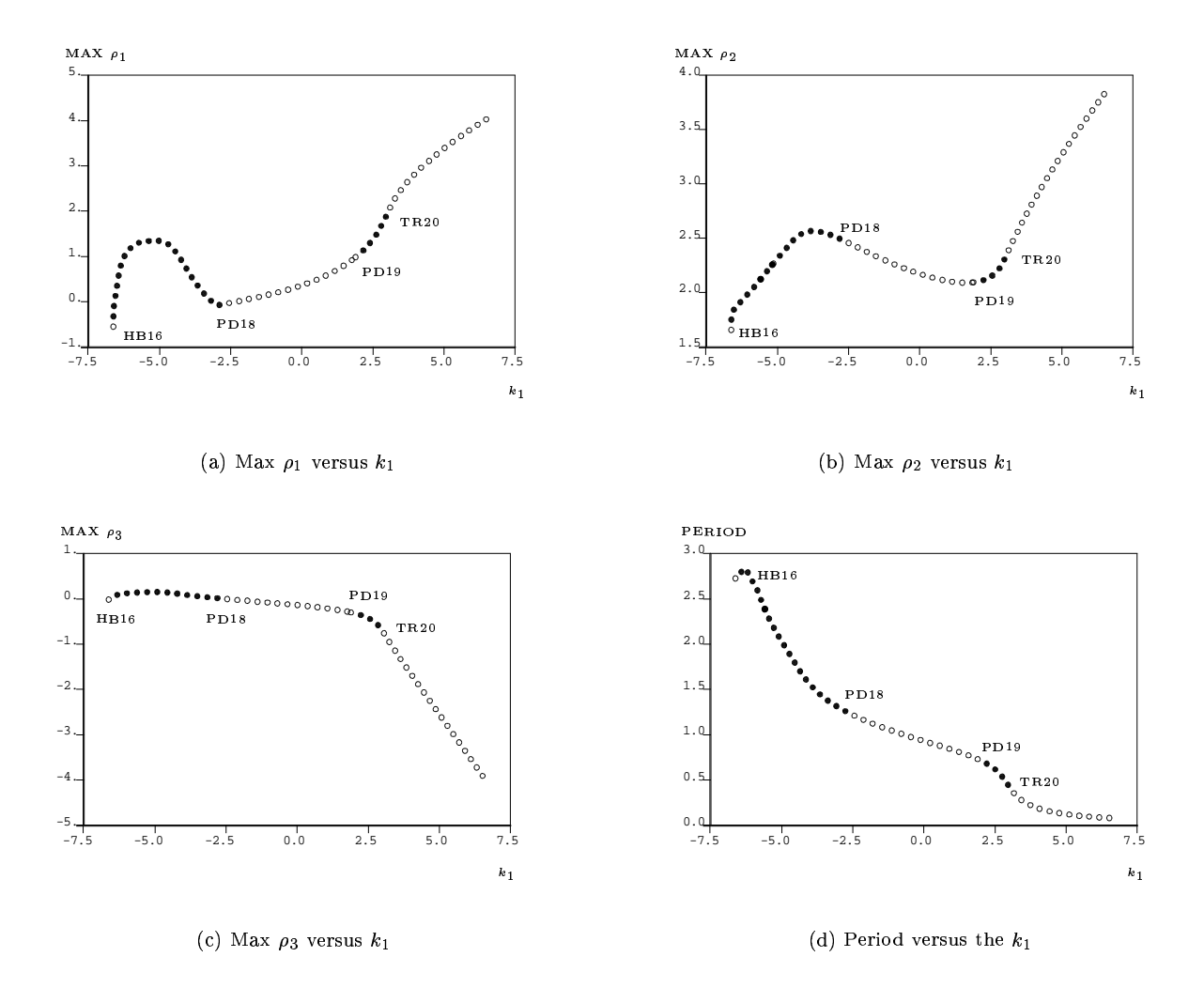


Figure 24: Continuation of the limit cycle branch of (A) from the third Hopf bifurcation point HB16 with c=1, R=8

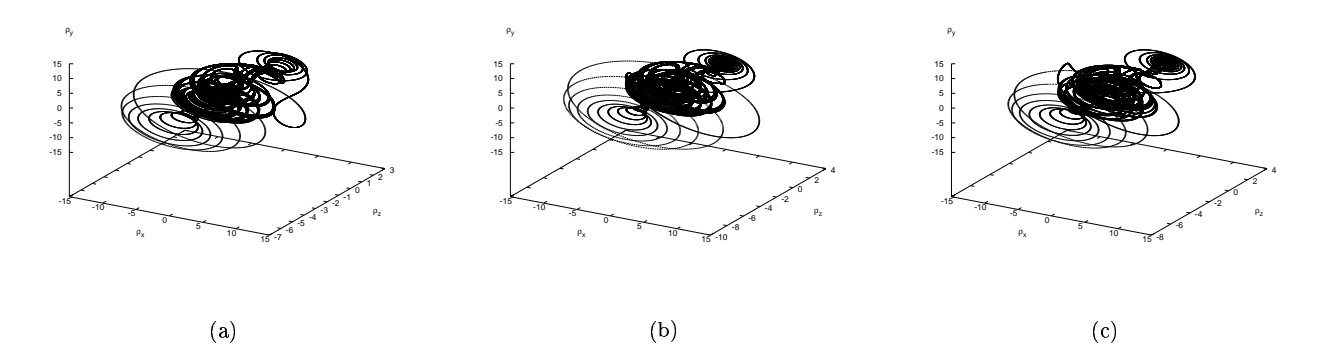


Figure 25: Orbits of the climate components for (a) the unreduced model, (b) (N) with modified Runge-Kutta scheme, (c) (N) with mixed scheme (strong Platen algorithm of order one if $\sigma(\rho_2) \neq 0$)

IMB when entering from above. The reason is that the measures tend to live on different bifurcation branches as the bifurcation parameter enters from different boundaries. IMF&B just keeps the branch chosen by the unreduced system when approaching a hysteresis interval. Since the dynamics of the unreduced model is taken into account in a very natural manner this way, it turns out that (A), (L) and (N) calculated on the basis of IMF&B perform much better than those computed with the other quoted methods to obtain invariant measures. Without further specification we always use IMF&B in the following simulations for (L) and (N).

To measure the closeness of trajectories of the solutions (η_1, η_2, η_3) of the reduced models to trajectories of the ocean variables (ρ_1, ρ_2, ρ_3) of the unreduced model, we introduce the divergence ratio

$$D(t) = \frac{\sqrt{[(\eta_1 - \rho_1)^2 + (\eta_2 - \rho_2)^2 + (\eta_3 - \rho_3)^2](t)}}{1 + \sqrt{[\rho_1^2 + \rho_2^2 + \rho_3^2](t)}}$$

and define the *closeness period* as the first time t for which D(t) exceeds the value of 0.1. We perform our comparison studies in the following two different situations:

- 1. Ocean forced by the atmosphere: First we assume that the coupling of ocean and atmosphere is just one way by putting $k_2 = 0$. This means that the ocean is just forced by the atmosphere, but gives no feedback (see Subsection 7.2)
- 2. Ocean coupled to the atmosphere: In the second more realistic case we assume $k_2 \neq 0$ so that both subsystems influence each other (see Subsection 7.3).

7.2 The unreduced ocean model forced by the atmosphere

7.2.1 Simulation of the unreduced ocean model

If $k_2 = 0$ and the ocean is just forced by the atmosphere, we shall concentrate on two different dynamical regimes. The first regime (**case** (a)) is periodic or quasi-periodic. The corresponding specification of the model parameters is given by R = 10, $\mu = 1$, $k_1 = 15$, $k_3 = 1$, $k_4 = 0.8$, c = 5, and $F_0 = 10$ (**case** (a1)). For this particular choice the atmosphere subsystem shows quasi-periodic behavior. The corresponding dynamics is exhibited in Fig. 26.

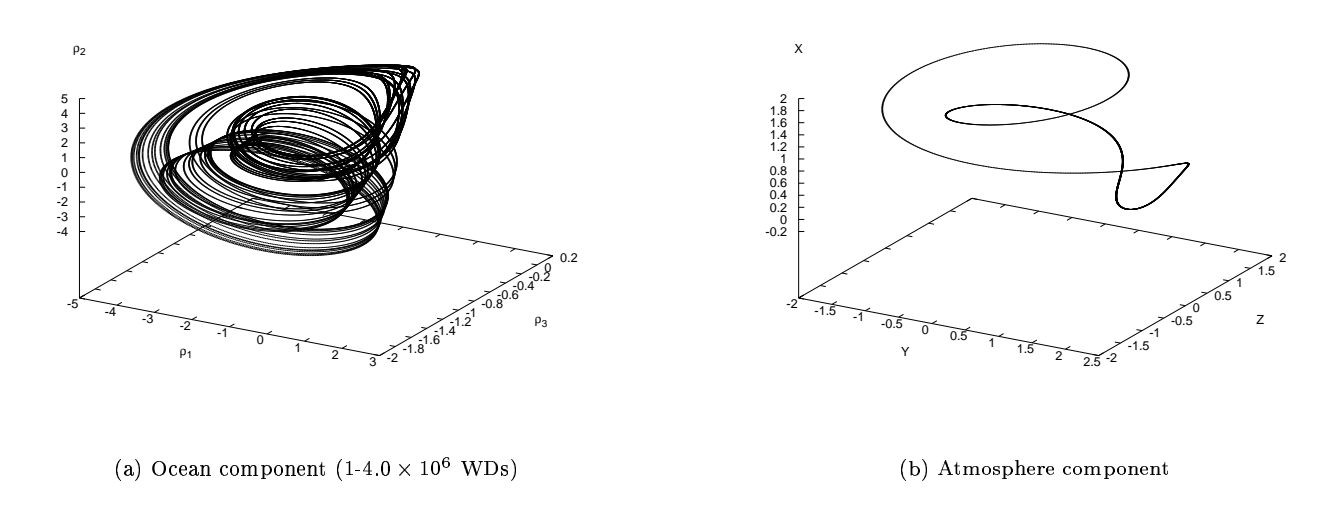


Figure 26: Orbits of the unreduced model in case (a1)

If we take R = 10, $\mu = 1$, $k_1 = 15$, $k_3 = 1.8$, $k_4 = 1/3$, c = 4.5, and $F_0 = 6$ (case (a2)), we obtain trajectories of the unreduced model as seen in Fig. 27, for which the atmosphere subsystem exhibits periodic behavior.

The second regime (case (b)) is characterized by chaotic behavior of the atmosphere component. This is guaranteed for instance for the choice R = 10, $\mu = 1$, $k_1 = 15$, $k_3 = 1$, $k_4 = 1/3$, c = 9 and $F_0 = 8$. Fig. 28 shows the characteristic ocean orbit of the unreduced model which wanders between two regimes irregularly, and the corresponding chaotic orbit of the atmosphere.

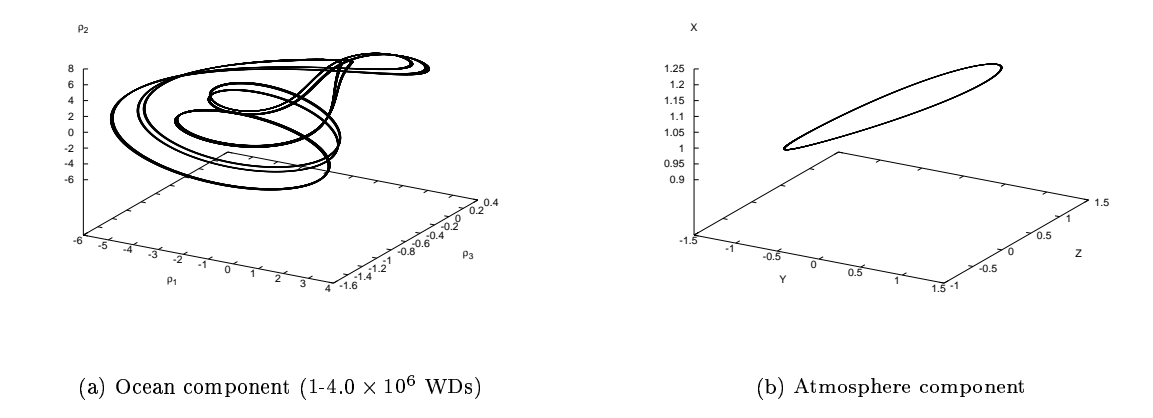


Figure 27: Orbits of the unreduced model in case (a2)

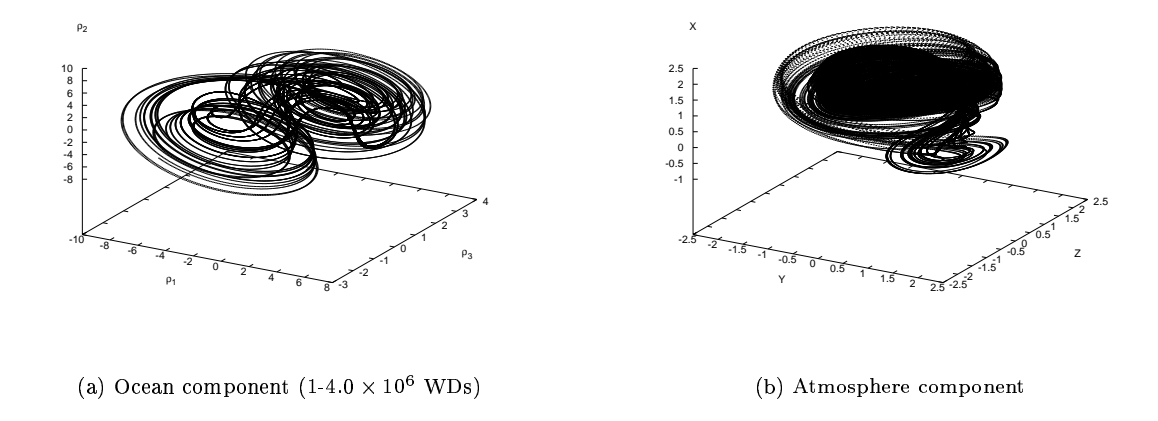


Figure 28: Orbits of the unreduced model in case (a2)

7.2.2 Comparison of the reduced ocean models with the unreduced model forced by the atmosphere

Let us now discuss the different reduced climate models with respect to their quality of approximation of the unreduced model whose behavior in the various regimes was illustrated in Subsect. 7.2.1.

In the first regime (a) the diffusion coefficients vanish, so that no source of stochasticity is present. Therefore in this regime the only relevant reduced model is (A).

For case (a1) IMF and IMB yield the same invariant measure. The characteristic orbits of (A) with various invariant measures are plotted in Fig. 29. It is show that the closeness period is more than 200,000 weather days for (A) with IMPF, while it is about 8,800 weather days for (A) with IMGAIO. During the closeness period (A) simulates the behavior of the ocean component of the unreduced model well. After this period the difference to the solution of (A) with IMGAIO becomes larger and larger, while the trajectory of (A) with IMPF diverges slightly from the orbit of the ocean subsystem of the unreduced model. Moreover, the flow pattern of the ocean variables of the unreduced model is reproduced well by (A) with IMPF while the solution of (A) with IMGAIO tends to a different limit cycle (see Fig. 29(c)). This indicates the dependence of the atmosphere subsystem with frozen ocean components on particular choices among non-unique invariant measures.

This is further exemplified in case (a2): For the parameter choice leading to the trajectories presented in Fig. 30 we see that the closeness periods of both the solution of (A) with IMPF and the solution of (A) with IMGAIO are approximately the same: about 18,000 weather days. However, the flow pattern of (A) with IMGAIO compares better to the one of the unreduced model than that of (A) with IMPF.

Here is an interesting side remark concerning the quality of approximation of climate variability in coupled atmosphere-ocean dynamical systems with two well separated time scales. Can one do better than (A) with a deterministic model? The answer seems to be "yes". For example, a simple seemingly artificial manipulation in (A) extends the closeness period by much: We replace the averaged \overline{X} and set it equal to the constant 0.7. The resulting behavior of the solution of the modified (A) model has a closeness period with respect to the corresponding trajectories of the unreduced model of more than 3.2×10^6 weather days (see Fig. 30(d))! It would be interesting to know if there are other ways than averaging to simulate climate variability in reduced deterministic models better.

In the chaotic regime represented by the parameter choice underlying ocean trajectories as in case (b), the diffusion coefficients no longer vanish. Here we are in the true realm of (L) and (N). 50 sample paths each are calculated for (L) and (N). In Fig. 31 we compare the performance of the three reduced models. In the first 38,400 weather days, the individual solution trajectories of (A), (L) and (N) with various invariant measures simulate well the behavior of the ocean subsystem of the unreduced model. After this period the trajectories of (A) with IMGAIO and of (L) diverge from that of the unreduced one. The solution of (A) with IMGAIO tends to a different quasi-periodic orbit (see Fig. 31(e)), while the solution of (L) oscillates dramatically and then diverges to infinity (not shown). Only the trajectories of (A) with IMPF and all the sample paths of Hasselmann's equation (N) continue describing the flow pattern of the unreduced model well.

Our results raise the following interesting question: Can we improve the output of our simulations by replacing individual trajectories with the ensemble mean over the 50 computed sample paths? For (L), ensemble averages extend the closeness period by a few hundred days (see Fig. 32). However, they do not seem to provide more information on the evolution of the ocean variables due to the wide scattering of the sample paths in phase space as time goes on. In addition, taking ensemble averages changes the structure of the flow pattern of the ocean orbit of the unreduced model considerably. This is also observed for (N). In fact, the following pattern seems to be supported by our simulations. The ensemble mean performs better than individual sample paths in short-range climate prediction, while in the long run individual trajectories provide more information on the transition of the flow among the flow regimes and on the structure of the flow patterns due to wide scattering of spontaneous transitions between meta-stable equilibria changing their local structure a lot.

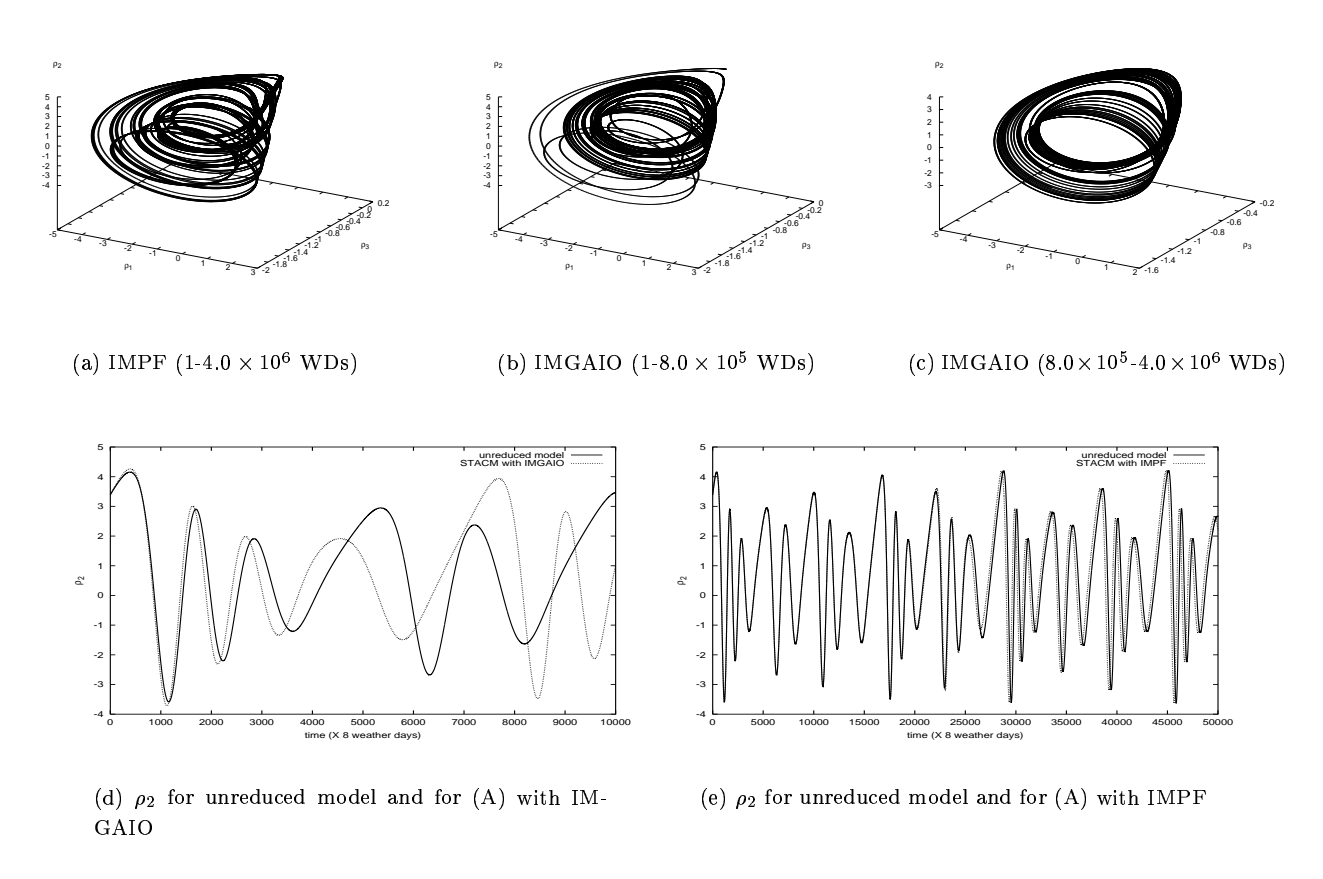


Figure 29: Orbits of reduced models in case (a1)

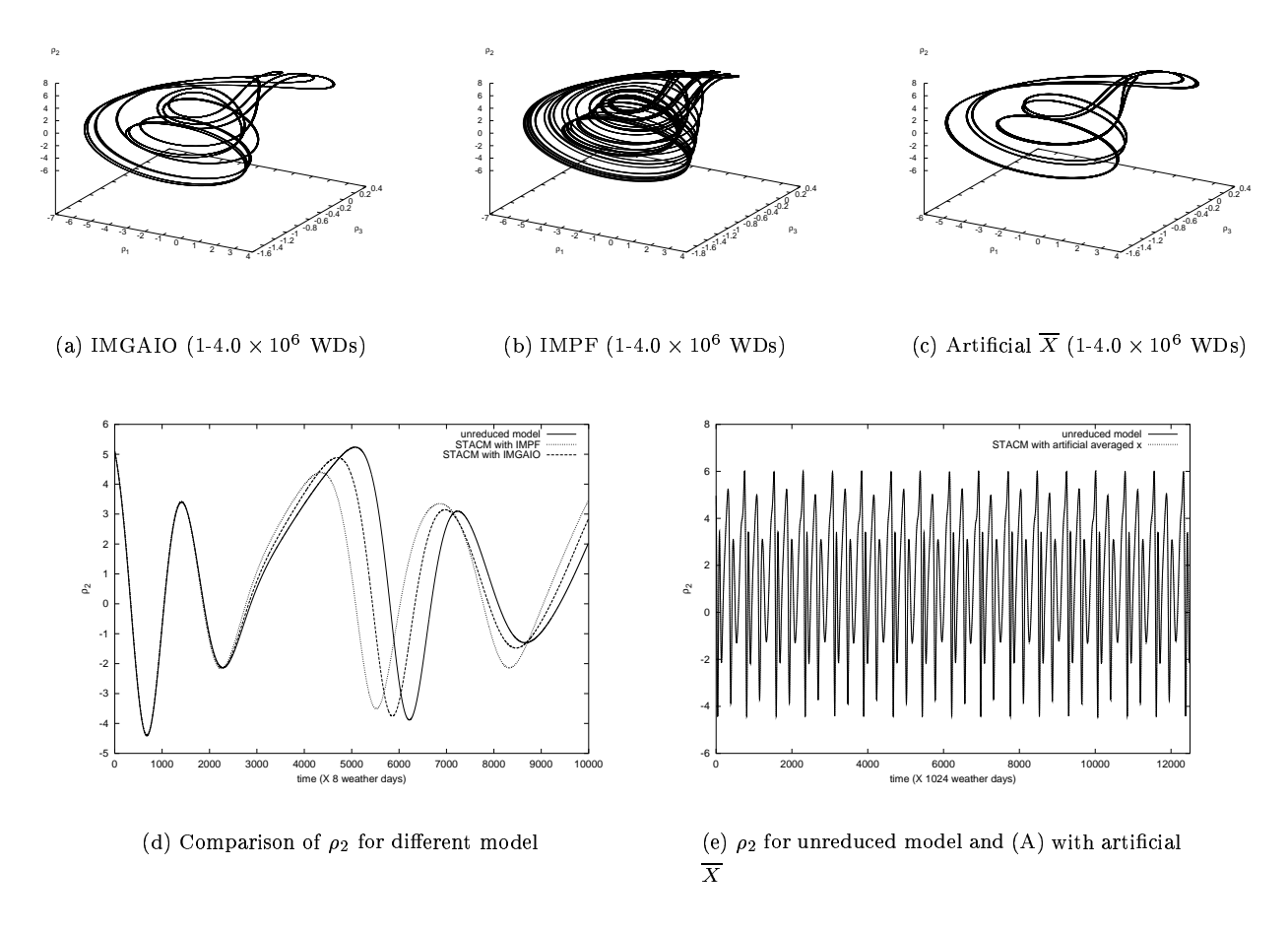


Figure 30: Orbits of reduced models in case (a2)

7.3 The unreduced ocean model coupled to the atmosphere

7.3.1 Simulation of the unreduced ocean model

We now come to the case $k_2 \neq 0$ in which atmosphere and ocean are influencing each other, and the dynamics becomes much richer. Here again we consider two different dynamical regimes which this time are determined by different types of asymptotic behavior of the ocean component of the unreduced model.

The first regime is characterized by quasi-periodic behavior of the ocean variables. The corresponding choice of the model parameters is given by R=5, $\mu=1$, $k_1=10$, $k_3=0.2$, $k_4=1$, c=1, $F_0=8$ and $k_2=1$ (case (c)). Fig. 33(a) shows a trajectory of the corresponding unreduced model. It is quasiperiodic with an approximate cycle length of about 3.85×10^5 weather days. Each period is subdivided into three stages. The first stage takes more than 62% of the time, during which the ocean orbit is on its way to reach a limit cycle traveling along the inner solid part of Fig. 33(a) which resembles a straight line. The density field varies slowly with very small amplitude. The second stage takes about 26% of the time, while the ocean orbit wanders near the limit cycle (the upper part of Fig. 33(a)). Dramatic changes occur in the third stage which occupies about 12% of the time. During this period the orbit turns off the limit cycle rapidly with large oscillations of both ρ_1 and ρ_2 , and a sharp decrease of ρ_3 from -0.80 to -13.00 before returning to the first stage and restarting the cycle.

The second regime is characterized by irregular wanderings of the ocean subsystem of the unreduced model between quasi-periodic parts of the orbits which are terminated by abrupt transitions. This can be observed for instance for the choice of parameters R=10, $\mu=1$, $k_1=10$, $k_3=1$, $k_4=1/3$, c=5, $F_0=8$ and $k_2=0.6$ case (d). Fig. 34 exhibits this behavior: the ocean orbit wanders for most of the time of about 1.28×10^5 weather days between transitions near a quasi-periodic orbit in a counter-clockwise sense (see Fig. 34(b)). It sometimes

changes the sense of rotation, winds up to the upper part of the trajectory, and then spirals downward in the counter-clockwise sense to the lower part (see Fig. 34(c)) with ρ_3 decreases rapidly from 2.50 to -6.90. Then the system returns to the part where most of the time is spent. In the integration time period of 1.20×10^7 weather days we find five transition events.

7.3.2 Comparison of the reduced ocean models with the unreduced model coupled to the atmosphere

We now turn to a discussion of the quality of approximation of the unreduced model by the different reduced models starting in the quasi-periodic regime. In Fig. 35 we show trajectories of (A), (L) and (N) in case (c). It is seen that the behavior of the ocean orbit is well recovered by (A) with different invariant measures and by both stochastic models (L) and (N). However, the closeness period of ocean orbits and the orbits produced by (A) with IMGAIO ends at about 8,000 weather days while it lasts for about 40,000 weather days for (A) with IMGAIO. Looking more closely (see Fig. 36), we further find that both (L) and (N) simulate the behavior of the ocean subsystem better than (A) with various invariant measures: The periods of the sample paths obtained from (A) with IMF&B and IMB are slightly different from that of the unreduced model, while those obtained by IMGAIO and IMF differ a lot.

Fig. 37 and 38 show some characteristic flow patterns of (A) and (N) with various invariant measures in case (d). In the first 8,000 weather days the behavior of the ocean subsystem of the unreduced model can be simulated well by (A) with various invariant measures, and by both (L) and (N). Then the differences among the various reduced models become obvious. Eventually (A) with various invariant measures fails to follow the ocean subsystem of the original model (see Fig. 37). The trajectories corresponding to (A) with IMF&B and IMF tend to a quasi-periodic orbit which can be thought of as the prototype of a quasi-periodic orbit of the unreduced model (see Fig. 37(a) and (b)), while the solutions of (A) with both IMB and IMGAIO (see Fig. 37(c) and (d)) enter into a quasi-periodic regime similar to Fig. 34(b).

The most interesting observation we obtain is the absence of any transition between various parts of the trajectories as discussed in the previous section for (A) with various invariant measures. In contrast to this, all the 50 sample paths obtained from (N) reproduce well this important feature of the ocean subsystem with a closeness period of about 80,000 weather days, though after the closeness period the transitions in the 50 individual sample paths and the ocean orbit of the original model are not entirely synchronous.

Fig. 38 gives three characteristic flow patterns obtained from a sample path of (N). A comparison to Fig. 34 reveals how well the trajectory of (N) interprets the three characteristic flow patterns of the original model, including spontaneous transitions together with their intensities. Only the variation of ρ_3 appears a little large in the lower part of the second pattern. Moreover, the power spectral densities derived from ρ_2 of the sample paths of (N) and of the unreduced model agree well (see Fig. 39). The difference lies in the tail of the power spectral density: The one for the sample path of (N) is a little wider or a little narrower than the one of the unreduced model. Therefore statistically the model (N) produces transition frequencies reflecting well the reality described by the ocean part of the unreduced model.

The instability of the trajectories of (A) with IMF&B has dramatic effects on (L): After an initial period they exhibit strong fluctuations and then diverge quickly. In Fig. 40 we show the evolution of the exponential growth rate of the trajectories of (L). We hence refrain from showing their diagrams.

8 Conclusions and discussion

Synopsis. To be skipped if only trivial repetitions

References

[1] L. Arnold. Hasselmann's program revisited: the analysis of stochasticity in deterministic climate models. In

- P. Imkeller and J.-S. von Storch, editors, *Stochastic Climate Models*, volume 49 of *Progress in Probability*, pages 141–157. Birkhäuser, Boston Basel Stuttgart, 2001.
- [2] L. Arnold. Linear and nonlinear diffusion approximation of the slow motion in systems with two time scales. In N. Sri Namachchivaya, editor, *IUTAM Symposium on Nonlinear Stochastic Dynamics, University of Illinois at Urbana-Champaign*. Kluwer, Dordrecht, 2002.
- [3] N. Bogolyubov and Y. Mitropolskii. Asymptotic methods in the theory of nonlinear oscillations. Gordon and Breach, New York, 1961.
- [4] M. Dellnitz, G. Froyland, and O. Junge. The algorithm behind GAIO set oriented numerical methods for dynamical systems. In B. Fiedler, editor, *Ergodic theory*, analysis, and efficient simulation of dynamical systems, pages 145–174. Springer, Berlin Heidelberg New York, 2001.
- [5] M. Dellnitz, A. Hohmann, O. Junge, and M. Rumpf. Exploring invariant sets and invariant measures. *CHAOS:* An Interdisciplinary Journal of Nonlinear Science, 7:221–228, 1997.
- [6] M. Denker. The central limit theorem for dynamical systems. In *Dynamical Systems and Ergodic Theory*, volume 23 of *Banach Center Publications*, pages 33–62. PWN Polish Scientific Publishers, Warszawa, 1989.
- [7] E. Doedel, A. Champneys, T. Fairgrieve, Y. Kuznetsov, B. Sandstede, and X. J. Wang. AUTO 97: continuation and bifurcation software for ordinary differential equations. California Institute of Technology, Pasadena, California, 1998.
- [8] M. Freidlin. The averaging principle and theorems on large deviations. Russian Math. Surveys, 33:117–176, 1978.
- [9] M. Freidlin and A. Wentzell. *Random perturbations of dynamical systems*. Springer-Verlag, Berlin Heidelberg New York, 1998. Second edition.
- [10] K. Gelfert. Asymptotic behavior of multi time-scale systems via Young measure limits. Preprint, MPI-PKS Dresden, 2002.
- [11] K. Gelfert. Bidirektional gekoppeltes lineares System. Preprint, MPI-PKS Dresden, 2002.
- [12] K. Hasselmann. Stochastic climate models: Part I. Theory. Tellus, 28:473–485, 1976.
- [13] K. Hasselmann. Climate change: linear and nonlinear signature. NATURE, 398:755-756, 1999.
- [14] I. A. Ibragimov and Y. V. Linnik. Independent and stationary sequences of random variables. Wolters-Noordhoff, Groningen, 1971.
- [15] P. Imkeller. Stochastic dynamics of climate states. Research Project for an SFB Proposal, Berlin, 2001.
- [16] P. Imkeller and A. Monahan, editors. Stochastic Climate Models, volume 2 of Stochastics and Dynamics. World Scientific, Singapore, 2002. Special Issue.
- [17] P. Imkeller and J.-S. von Storch, editors. *Stochastic Climate Models*, volume 49 of *Progress in Probability*. Birkhäuser, Boston Basel Stuttgart, 2001.
- [18] W. Just, K. Gelfert, N. Baba, A. Riegert, and H. Kantz. Elimination of fast chaotic degrees of freedom: on the accuracy of the Born approximation. Preprint, MPI-PKS Dresden, 2002.
- [19] W. Just, H. Kantz, C. Rödenbeck, and M. Helm. Stochastic modelling: replacing fast degrees of freedom by noise. *J. Phys. A: Math. Gen.*, 34:3199–3213, 2001.
- [20] H. Kantz, W. Just, and N. Baba. Replacing fast chaotic degrees of freedom by noise: a formally exact result. Preprint, MPI-PKS Dresden, 2002.

- [21] A. Katok and B. Hasselblatt. *Introduction to the modern theory of dynamical systems*. Cambridge University Press, 1995.
- [22] R. Z. Khasminskii. A limit theorem for solutions of differential equations with random right-hand side. *Theory of Probability and its Applications*, 11:390–406, 1966.
- [23] R. Z. Khasminskii. On stochastic processes defined by differential equations with a small parameter. *Theory of Probability and its Applications*, 11:211–228, 1966.
- [24] Y. Kifer. Averaging in dynamical systems and large deviations. Invent. math., 110:337–370, 1992.
- [25] Y. Kifer. Limit theorems in averaging for dynamical systems. *Ergodic Theory and Dynamical Systems*, 15:1143–1172, 1995.
- [26] Y. Kifer. Averaging and climate models. In P. Imkeller and J.-S. von Storch, editors, *Stochastic Climate Models*, volume 49 of *Progress in Probability*, pages 171–188. Birkhäuser, Boston Basel Stuttgart, 2001.
- [27] Y. Kifer. Stochastic versions of Anosov's and Neistadt's theorems on averaging. *Stochastics and Dynamics*, 1:1–21, 2001.
- [28] Y. Kifer. L^2 diffusion approximation for slow motion in averaging. Preprint, Institute of Mathematics, Hebrew University, 2002.
- [29] P. E. Kloeden and E. Platen. Numerical solution of stochastic differential equations. Springer-Verlag, Berlin Heidelberg New York, 1992.
- [30] P. E. Kloeden, E. Platen, and H. Schurz. *Numerical solutions of SDE through computer experiments*. Springer-Verlag, Berlin Heidelberg New York, 1994.
- [31] P. Lochak and C. Meunier. *Multiple averaging for classical systems*. Springer-Verlag, Berlin Heidelberg New York, 1988.
- [32] E. Lorenz. Irregularity: a fundamental property of the atmosphere. Tellus, 36A:98-110, 1984.
- [33] L. Maas. A simple model for the three-dimensional, thermally and wind-driven ocean circulation. *Tellus*, 46A:671–680, 1994.
- [34] L. Maas. Basin scale dynamics of a stratified rotating fluid, Preprint, Netherlands Institute for Sea Research, 2001.
- [35] A. Majda, I. Timofeyev, and E. Vanden-Eijnden. A mathematical framework for stochastic climate models. Communications on Pure and Applied Mathematics, 54:891–974, 2001.
- [36] A. Majda, I. Timofeyev, and E. Vanden-Eijnden. A priori tests of a stochastic mode reduction strategy. Preprint, Courant Institute of Mathematical Sciences, New York University, 2002.
- [37] C. Masoller, A. Schifino, and L. Romanelli. Characterisation of strange attractors of Lorenz model of general circulation of the atmosphere. *Chaos, Solitons & Fractals*, 6:357–366, 1995.
- [38] M. Ollers Towards a validation of a low-order ocean model for the thermohaline circulation with two Ocean General Circulation models, *Master Thesis*, *Utrecht University*, 1999.
- [39] Y. A. Rozanov. Stationary random processes. Holden-Day, San Francisco, 1967.
- [40] J. A. Sanders and F. Verhulst. Averaging methods in nonlinear dynamical systems. Springer-Verlag, Berlin Heidelberg New York, 1985.
- [41] A. Shilnikov, G. Nicolis, and C. Nicolis. Bifurcation and predictability analysis of a low-order atmospheric circulation model. *Journal of Bifurcation and Chaos*, 5:1701–1711, 1995.

- [42] A. Sicardi and C. Masoller. Analytical study of the codimension two bifurcation of the new Lorenz system. Instabilities and Non-equilibrium Structures, 5:345–348, 1996.
- [43] C. L. Siegel and J. Moser. *Lectures on celestial mechanics*. Springer-Verlag, Berlin Heidelberg New York, 1971.
- [44] R. Temam. Infinite-dimensional dynamical systems in mechanics and physics. Springer-Verlag, Berlin Heidelberg New York, 1988.
- [45] L. van Veen. Time scale interaction in low-order climate models. PhD thesis, Department of Mathematics, Universiteit Utrecht, 2002.
- [46] L. van Veen, T. Opsteegh, and F. Verhulst. Active and passive ocean regimes in a low-order climate model. Tellus, 53A:616–628, 2001.
- [47] M. Viana. Stochastic dynamics of deterministic systems. IMPA, Rio de Janeiro, 1997.
- [48] A. J. Weaver, S. M. Aura, and P. G. Myers. Interdecadal variability in an idealized model of the North Atlantic. *J. Geophys. Res.*, 99:12423–12441, 1994.
- [49] A. J. Weaver and E. S. Sarachik. Evidence for decadal variability in an ocean general circulation model. Atm.-Ocean, 29:197–231, 1991.

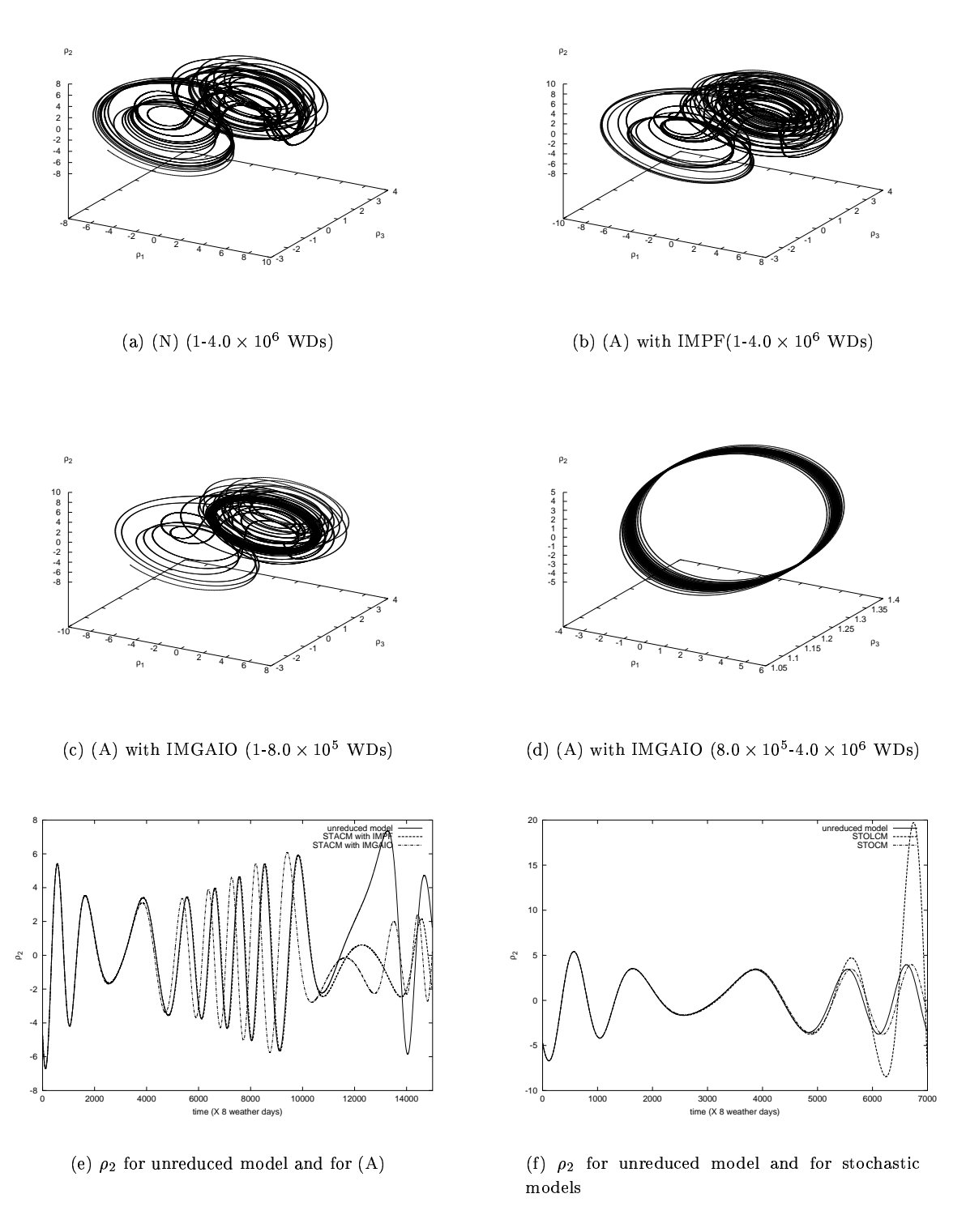


Figure 31: Orbits of reduced models in case (b)

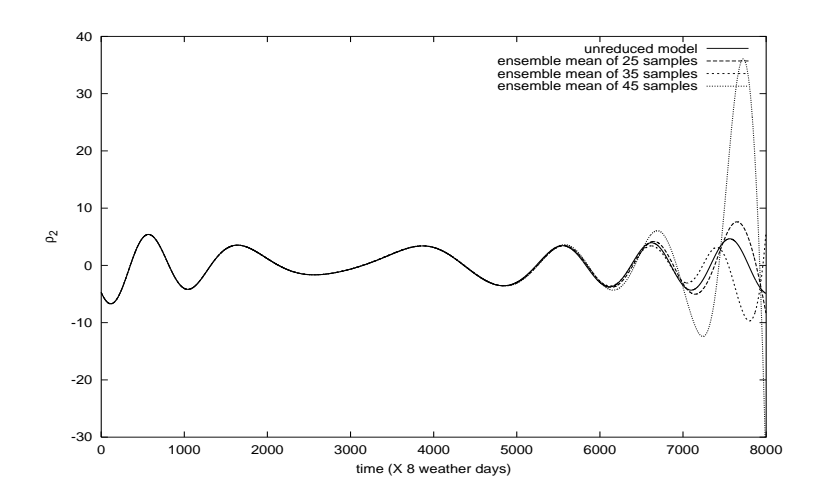


Figure 32: ρ_2 for unreduced model and for (L)

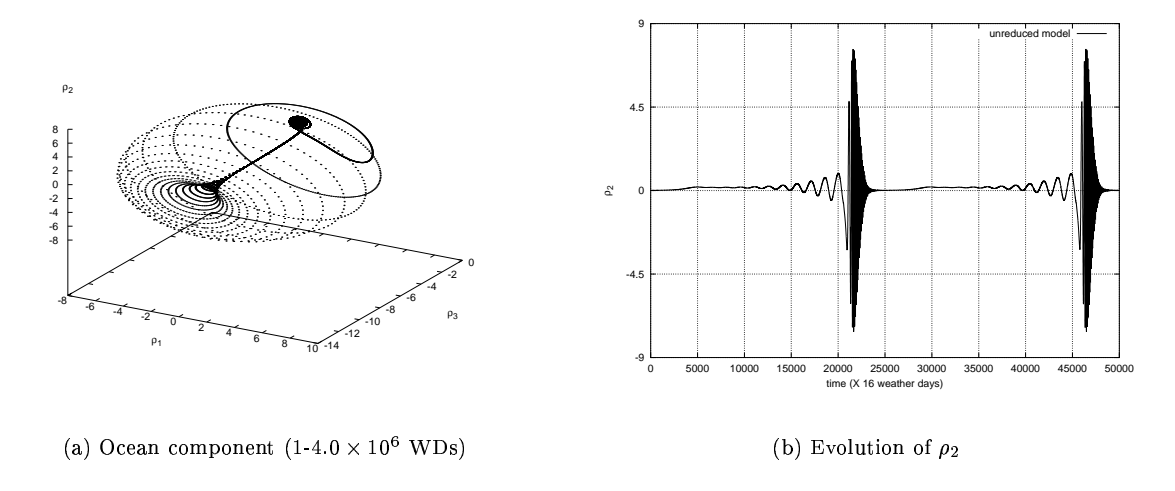


Figure 33: Orbit of climate component of unreduced model in case (c)

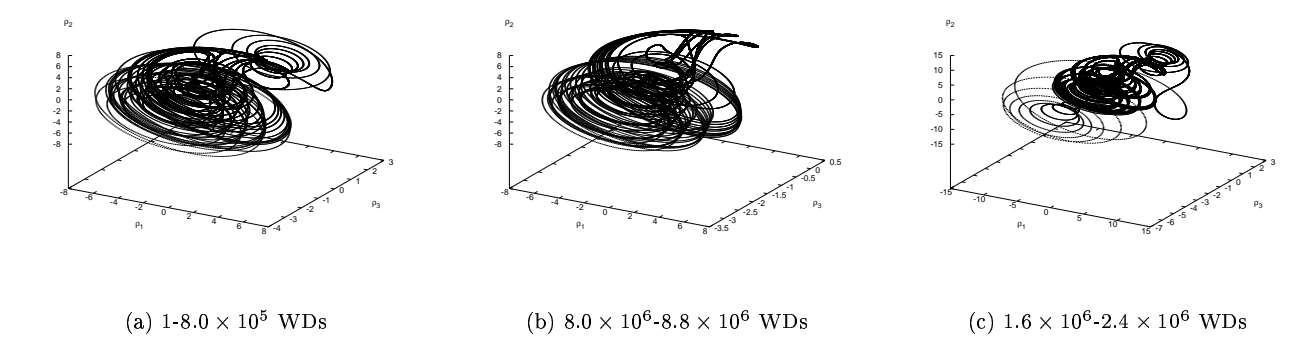


Figure 34: Orbits of climate component of unreduced model in case (d)

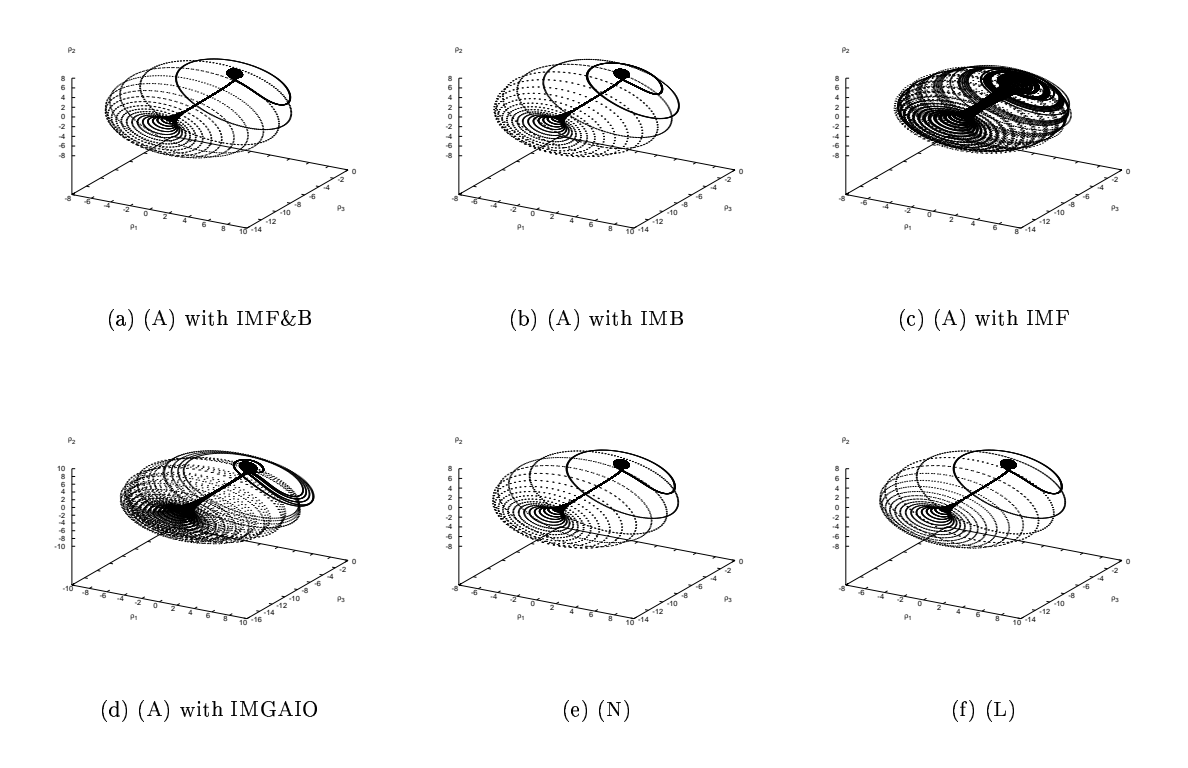


Figure 35: Orbits of reduced models in case (d) $(1-4.0 \times 10^6 \text{ WDs})$

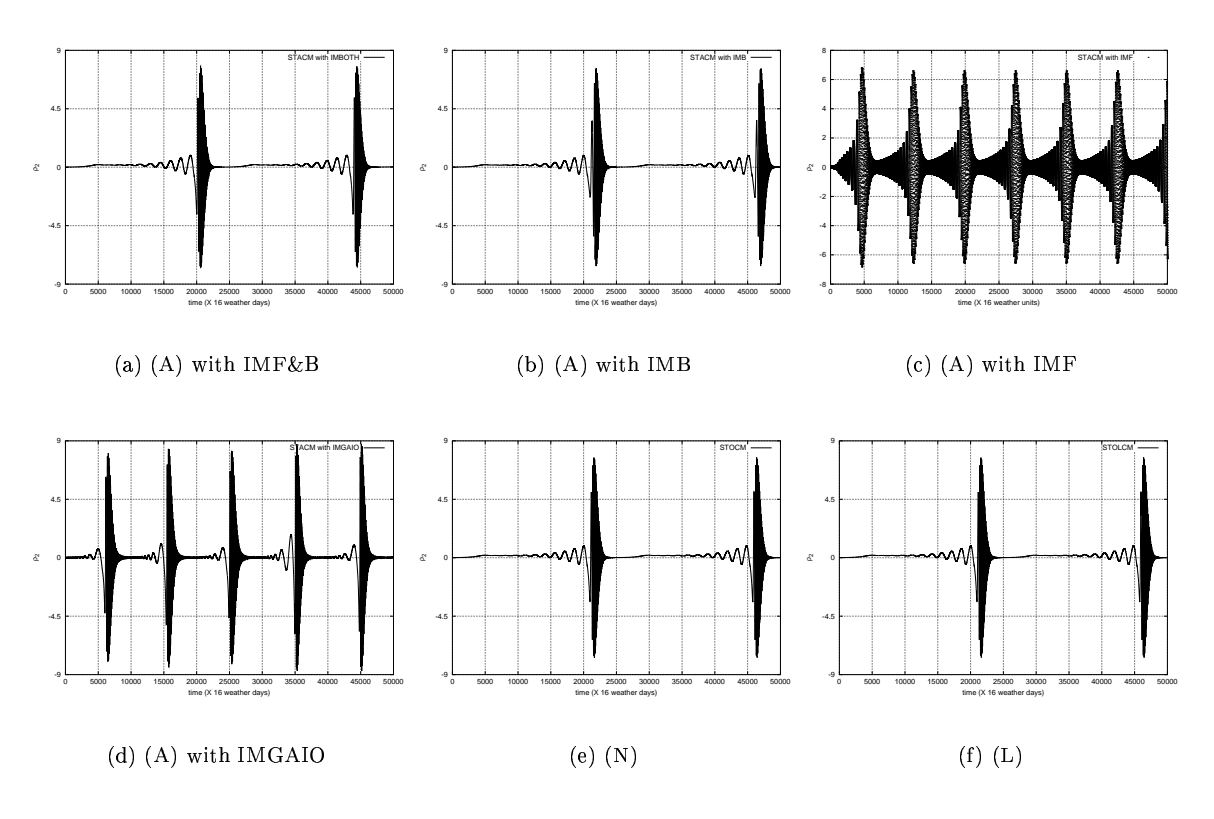


Figure 36: ρ_2 for various models in case (d)

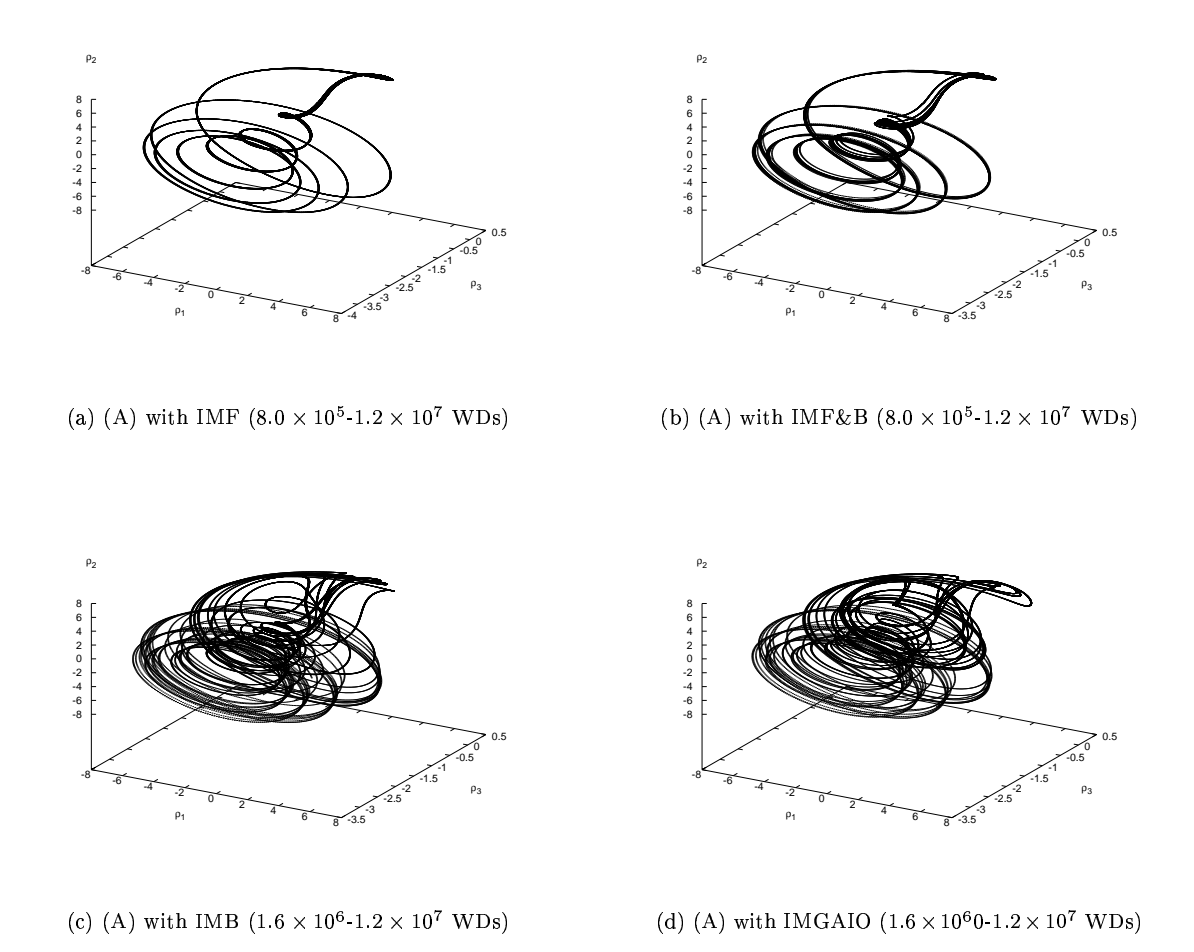


Figure 37: (A) with various invariant measures in case (d)

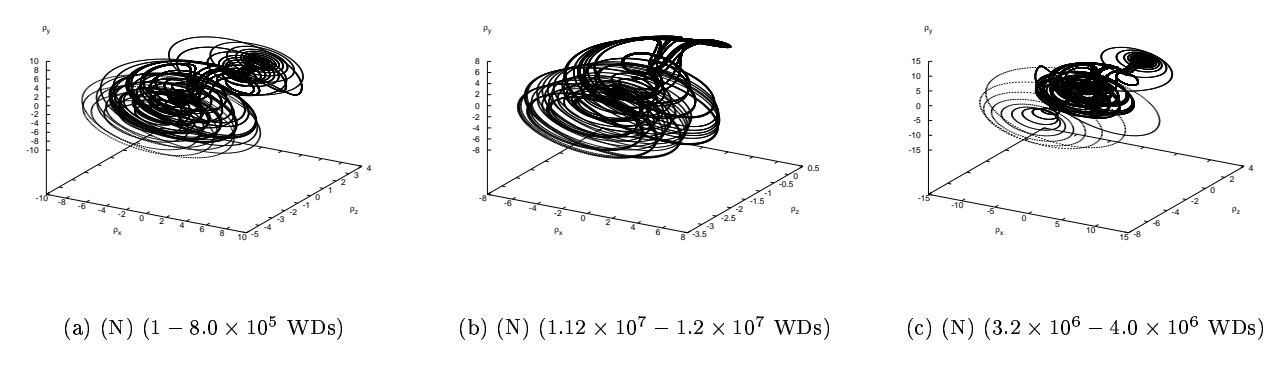


Figure 38: (N) in case (d)

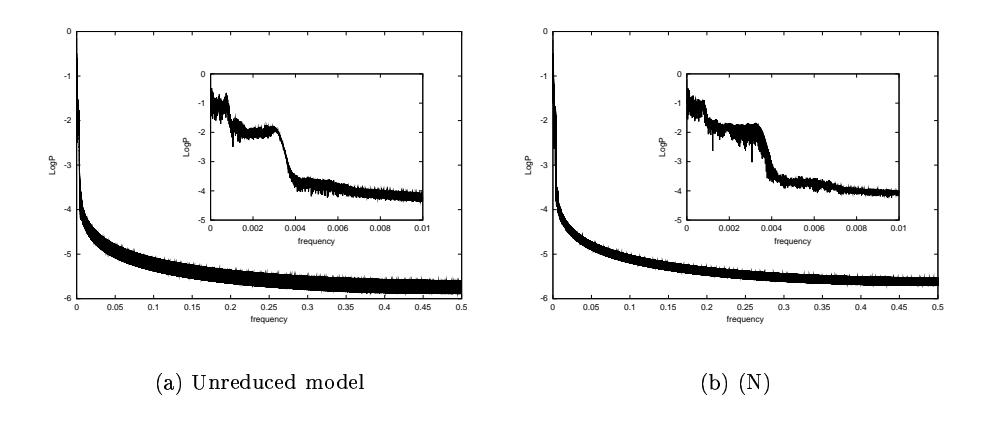


Figure 39: Power spectral densities of ρ_2 in case (d)

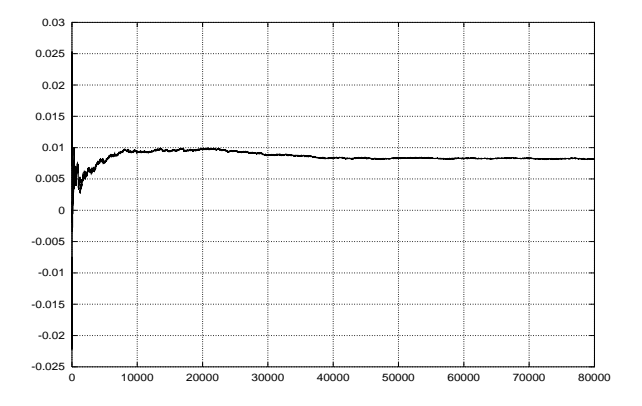


Figure 40: Evolution of $\frac{1}{t}\ln|\rho(t)|$ in case (d)